Università degli Studi di Ferrara

DOTTORATO DI RICERCA IN

FISICA

CICLO XXVIII

COORDINATORE Prof. Vincenzo Guidi

SPIN DYNAMICS IN TWO-DIMENSIONAL MAGNONIC CRYSTALS

Settore Scientifico Disciplinare FIS/03

Dottoranda

Dr. Perla Malagò

Tutori

Prof. Loris Giovannini

Dr. Roberto Zivieri

Anni 2013/2015

Contents

Introduction

Magnetic nanostructures have received a lot of attention in latest years, both from a fundamental point of view and for the several potential technological applications. In the last few years, these structures become one of the most important and exciting areas of the present solid state research[1]. This is due to both the interest towards the comprehension of magnetism and the prospect of important applications in the technology of solid state electronic devices and magnetic recording media. Nanostructured magnetic materials are known to possess further functionalities that cannot be achieved in their bulk constituents. As an example are effects like Giant Magnoresistance[2,3] and Perpendicular Magnetic Anisotropy[4,5], and they have a great impact on the development of new technological equipment and products. Moreover, the research in this field has been stimulated by the availability of sophisticated growth and characterization techniques. As a consequence, nowadays magnetic nanostructures can be fabricated with high precision and their properties are intensively investigated by means of high sensitivity experimental technique and of high accuracy theoretical models. A very interesting field of magnetism consists in the study of the spin dynamics. Spin wave is the collective excitation of the microscopic magnetization[6]. The first direct observation of spin waves was made using ferromagnetic resonance by Griffiths for the case of uniform precession[7]. Later, Brillouin light scattering experiments performed by Fleury *et al* confirmed the existence of spin waves with non-zero wave vectors[8] . In the last years the collective excitations have been widely investigated both from the theoretical and experimental point of view with the aim of probing the intrinsic dynamic properties of the nanoparticles. Thanks to the high precision of the fabrication technique, now it is possible to create one, two or three dimensional magnetic nanostructures of different shapes and composed of different ferromagnetic materials. Indeed, the spin dynamics have been studied in thin films, in isolated elements and in periodic magnetic systems. Recently, it has been found that the periodic systems can support the propagation of collective spin waves. As a consequence, among the possible geometries, periodic

ferromagnetic systems are the most investigate because they give the possibility of tailoring the dynamic properties in the nanoscale. Periodic ferromagnetic systems are magnetic materials with periodic geometric modulation and are called magnonic crystals[9,10,11]. Therefore, magnonic crystal represents the magnetic analogue of photonic crystals. The spin wave spectrum is modified by patterning[12] and may show a tailored band structure in periodic magnetic materials[13]. The band spectrum consists of bands of allowed magnonic states and forbidden-frequency gaps ('band gaps'), in which there are no allowed magnonic states. One of the first attempts to study the propagation of spin waves in periodic magnetic structures was made by Elachi[14]. Presently, thanks to the multitude of studies in this field, it is possible to understand magnetization dynamics and (a) to design metamaterial devices[15,16], (b) to transduce and transmit signals[17,18,19], (c) to realize magnonic transistors[20], and (d) to make logic operations [21,22,23]. The large variety of shapes and of their arrangements together with magnetic configurations which can be realized in magnonic crystals[24,25,26,27], makes magnonics an inexhaustible and intriguing topic of research.

The main goal of this Thesis is to investigate from a fundamental point of view the magnetic properties of periodic magnetic nanostructures by means of micromagnetic methods. The analysis collected here give an advancement in the field of nanomagnetism providing detailed descriptions of new phenomena. In order to understand the effects due to different shapes geometries or materials on the spin dynamic, different periodic ferromagnetic systems are studied. Investigations are performed both in propagative and stationary regime evaluating the band structures of spin waves modes and their dependence on the geometric and magnetic parameters. This lead to the appearance of new physical effect previously unrevealed in magnonic crystals. New physical mechanisms are explained from a theoretical point of view and most of them are totally confirmed by experimental measurements provided by others research group. Hence, the results shown here are not only theoretical prediction but also confirmed experimentally in order to propose these systems as prototypes of new technologies and to increase the basic physics knowledge in the field of the nanomagnetism and magnonics. It is also important to underline that the magnonic systems considered can be easily created by means of fabrication technique or in some case have been already constructed.

Theoretical basis of the nanomagnetism are introduced in Chapter 1. Here, the macroscopic, microscopic and micromagnetic theories are presented and compared to each others. Moreover, basic concepts of spin wave, magnonic crystals, magnonic devices and metamaterial are given. A brief description of the Brillouin light scattering technique is also provided.

In Chapter 2, the method used to study the magnetic properties of magnetic nanostructures illustrated in this Thesis is presented. The calculations has been performed through a micromagnetic approach, in particular is used the Dynamical Matrix Method[28]. This is a finite-difference method developed in the past years in our research group able to calculate the dynamic properties of the magnetization.

The main results obtained during the Ph.D are collected in Chapters 3, 4 and 5. Chapter 3 is focused on the analysis of the magnetic properties of mono-material two-dimensional magnonic crystals[29,30]. In the first Section, the presence of soft modes is demonstrated in two-dimensional periodic magnetic systems composed of holes embedded into a ferromagnetic matrix. Moreover, the softening mechanism is also

investigated from a theoretical point of view in order to understand the physical phenomena at the basis of the frequency softening. The second Section is devoted to the study of the effect of ground-state magnetization on the band structures of a two-dimensional magnetic system. Dispersion curves of the spin waves modes and their feature are calculated and compared for the case of in-plane magnetized system and for the case of out-of-plane magnetized system.

In Chapter 4 the magnetic properties of multi-material two dimensional magnonic crystals are analyzed[31,32]. The systems investigated here are called bicomponent magnonic crystals because they are composed of two different ferromagnetic materials. In the first Section four different periodic systems made up of Permalloy and Cobalt are analyzed in order to understand how the position and volume of the Cobalt dot influence the band structures of the spin waves modes. The second Section is focused on the study of the influence of a non-magnetic spacer between two ferromagnetic materials on the band structure of spin waves modes in five different magnonic crystals is investigated[33]. In order to do this, the spin waves modes are examined in the first Brillouin zone and the internal total field for each system has been calculated.

Finally, the static and dynamic properties of the magnetization in isolated elliptical Permalloy and Cobalt dots as a function of the external magnetic field. Here, the magnonic modes are investigated over the major and minor hysteresis curve, encompassing both the parallel and anti-parallel ground state. In order to turn magnonic crystals as a new class of metamaterials, the metamaterial properties of these systems have been studied form a theoretical point of view in Chapter 5. By means of the introduction of new effective quantities, the effective properties of both mono[34] and multi-material[35] magnonic crystals are investigated.

List of publications

The work presented in this thesis is based on the following **articles and conference proceedings**:

1) **P. Malagò**, L. Giovannini and R. Zivieri, "Perpendicularly Magnetized Antidot Lattice as a Two-Dimensional Magnonic Metamaterial", in Proceedings of the 9th International Congress on Advanced Electromagnetic Materials in Microwaves and Optics pp. 535-537 – Metamaterials 2015, Oxford, United Kingdom, 7-12 September 2015.

2) **P. Malagò,** L. Giovannini, R. Zivieri, P. Gruszecki and M. Krawczyk "Spin-wave dynamics in permalloy/cobalt magnonic crystals in the presence of a nonmagnetic spacer ", Phys. Rev. B **92**, 064416 (2015).

3) G. Gubbiotti, **P. Malagò**, S. Fin, S. Tacchi, L. Giovannini, D. Bisero, M. Madami, G. Carlotti, J. Ding, A. O. Adeyeye, and R. Zivieri "Magnetic normal modes of bi-component permalloy/cobalt structures in the ferromagnetic and antiferromagnetic state", Phys. Rev. B **90**, 024419 (2014).

4) **P. Malagò**, L. Giovannini and R. Zivieri, "Effective properties of a binary magnonic crystal" , in Proceedings of the 8th International Congress on Advanced Electromagnetic Materials in Microwaves and Optics pp. 316-318– Metamaterials 2014, Copenaghen, Denmark, 25-30 August (2014).

5) R. Zivieri, **P. Malagò**, and L. Giovannini, "Band structure of collective modes and effective properties of binary magnonic crystals", Photon. Nanostruct.: Fundam. Appl. **12**, 398 (2014).

6) R. Zivieri, **P. Malagò**, L. Giovannini, S. Tacchi, G. Gubbiotti, A. O. Adeyeye "Soft magnonic modes in two-dimensional permalloy antidot lattices" J. Phys.: Condens. Matter **25** 336002 (2013).

7) R. Zivieri and **P. Malagò**, "Metamaterial properties of a three-dimensional permalloy/cobalt binary system", in Proceedings of the 7th International Congress on Advanced Electromagnetic Materials in Microwaves and Optics p.439-441– Metamaterials 2013, Bordeaux, France, 16-21 September (2013).

Contributions (oral/poster) to conferences:

1) Oral presentation: **P. Malagò**, L. Giovannini and R. Zivieri, "Dynamical properties of 2D ferromagnetic antidot lattices", FISMAT 2015 – Italian National Conference on Condensed Matter Physics, Palermo, Italy, 28-2 October 2015.

2) Oral presentation: **P. Malagò**, P. Gruszecki, L. Giovannini, M. Krawczyk, "The influence of non-magnetic spacers in two-dimensional binary magnonic crystals on spin wave spectra", 20th International Conference on Magnetism ICM 2015, Barcelona, Spain, 5-10 July 2015.

3) Poster presentation: E. Bonfiglioli, **P. Malagò**, F. Spizzo, M. Tamisari, L. Giovannini, L. Del Bianco, "Modeling the exchange bias interaction in nanostructures", 20th International Conference on Magnetism ICM 2015, Barcelona, Spain, 5-10 July 2015.

4) Poster presentation**:** **P. Malagò**, L. Giovannini and R. Zivieri, "Metamaterial description of perpendicularly magnetized 2D antidot lattices", Magnet 2015 - IV Conference of the Italian Magnetism Association, National conference, Bologna, Italy, 17-19 February 2015, AIMagn (Associazione Italiana di Magnetismo).

5) Poster presentation: **P. Malagò**, L. Giovannini and R. Zivieri, "Effective properties of a binary magnonic crystal", in Proceedings of the 8th International Congress on Advanced Electromagnetic Materials in Microwaves and Optics – Metamaterials 2014, Copenaghen, Denmark, 25-30 August 2014.

6) Poster presentation: **P. Malagò**, G. Gubbiotti, S. Tacchi, R. Zivieri, L. Giovannini, M. Madami, and G. Carlotti "Magnetic normal modes in ferromagnetic and antiferromagentic state bi-component periodic system", Physics of Magnetism PM'14, Poznan, Poland 23-27 June 2014.

7) Oral presentation: **P. Malagò**, R. Zivieri, L. Giovannini "Magnonic modes in three-dimensional permalloy/cobalt binary systems", 58th Annual Conference on Magnetism and Magnetic Materials, International conference, Denver USA, 4-8 November 2013, AIP Publishing & IEEE Magnetics Denver, USA.

8) Poster presentation: R. Zivieri, **P. Malagò**, L. Giovannini "Metamaterial properties of three-dimensional permalloy/cobalt magnonic crystals", 7th International Congress on Advanced Electromagnetic Materials in Microwaves and Optics III-101-1-3 (2013)– Metamaterials 2013,

Bordeaux, France, 16-21 September 2013, International conference. University of Bordeaux, IdEx and LabEx Amadeus Bordeaux, France.

9) Poster presentation: R. Zivieri, **P. Malagò** "Metamaterial description of magnonic modes along ΓM direction in a 2D antidot lattice" 7th International Congress on Advanced Electromagnetic Materials in Microwaves and Optics III-101-1-3 (2013)– Metamaterials 2013, Bordeaux, France, 16-21 September 2013, International conference. University of Bordeaux, IdEx and LabEx Amadeus Bordeaux, France.

10) Poster presentation: R. Zivieri, **P. Malagò**, L. Giovannini "Size effects on spin dynamics in 2D ferromagnetic antidot lattices", 9th International Symposium on Hysteresis Modelling and Micromagnetics, International conference, Taormina, Italy, 13-15 May 2013, IEEE Magnetics Italian Chapter & Magnetism Research Group, University of Messina, Italy Taormina, Italy.

11) Oral presentation: **P. Malagò**, R. Zivieri, L. Giovannini "Size Effects on Spin-wave Modes in Ferromagnetic Antidot Lattices", Magnet 2013 - III Convegno Nazionale di Magnetismo, National conference, Napoli, Italy, 20-22 February 2013, AIMagn (Associazione Italiana di Magnetismo).

Chapter 1
Magnetic nanostructures

Nanoscience involves the study of phenomena occurring in objects of dimensions in the range 1 to 1000 nm. This is the range of sizes of many molecules and viruses, and is also the characteristic length scale of many physical processes[36]. Moreover, the lateral dimensions of integrated circuit components, as well as the dimensions of grains in magnetic-recording film media, belong to the nanometer range. Nanomagnetism is the area of physics research concerning the magnetic properties of systems having at least one dimension in the submicron range. Even if the magnetism is an old scientific discipline, physics of the magnetic nanostructures has become one of the most interesting research fields in the last decades, driven by the scientific and technologic trend towards miniaturization of physical systems. Particular interest has been received from the analysis of magnetic nanostructures because they show magnetic properties typical of both magnetic systems and nanostructures. The research in this field has been stimulated by the availability of sophisticated growth and characterization techniques and by the discovery of new and stimulating phenomena, such as giant magnetoresistance (GMR)[3,37], anti-ferromagnetic interlayer exchange coupling (AFC)[38] and perpendicular magnetic anisotropy (PMA)[39,40]. Nowadays, thanks to the progress in the fabrication methods it is possible to fabricate magnetic nanostructures having high quality and well-defined shapes. For example it is possible to create nanoelements of different shapes, periodic nanostructures, and magnetic nanostructures composed of different ferromagnetic materials. As a consequence, also the methods able to characterize from a theoretical and experimental point of views this ferromagnetic systems have been developed.

Measurements of the magnetic properties of nanostructures are highly demanding in view of the small amount of magnetic material involved[41]. The superconducting quantum interference devices (SQUID) are designed for measurements of the magnetic moment of thin film and can achieve sensitivities and accuracies

that rival any other magnetometric techniques, as exemplified by the pioneering work of Gradmann and co-workers using a UHV compatible SQUID [42]. It is only relatively recently that the extraordinary sensitivity of the magneto-optic Kerr effect (MOKE) in probing magnetic properties has been fully appreciated and now its use is widespread in the study of nanostructures[43,44]. Ferromagnetic resonance (FMR)[45,46] and Brillouin light scattering (BLS)[47,48] techniques have provided an important role in the study of the dynamical properties of magnetic nanostructures. FMR technique consists in measuring spectra of the absorption of microwaves in a cavity containing a magnetic sample. Differently, BLS technique is based on the phenomenon of Brillouin-Mandelstam inelastic scattering pumped magnon. Moreover, several powerful high-sensitivity imaging techniques have been developed recently: for example, atomic force microscopy, magnetic force microscopy, scanning Kerr microscopy and spin-polarized microscopy. As a theoretical counterpart, also micromagnetic and analytical methods have been developed in order to understand the properties of the nanostructures. As an example: Object Oriented MicroMagnetic Framework (OOMMF)[49], MicroMagus[50], Plane Wave Method (PMW)[10] and Dynamical Matrix Method (DMM)[28].

1.1 Magnonic crystals

Magnonic crystal (MC) consists of a periodic magnetic system. They are magnetic systems in which the spectrum of magnons has a band structure and contains band gaps. The artificially introduced periodicity modifies the energy spectrum of magnons. The dipolar or exchange interactions dominate spin waves (SWs) spectra depending on the absolute value of the periodicity of the MC. A frequency gap might open such that magnon propagation through the MCs is forbidden for a specific frequency range. In periodically nanopatterned magnetic media minibands are formed: they consist of allowed SW frequencies and forbidden frequency gaps and this depends on the structure created[51]. Due to the complicated geometry, it can be difficult to take into account analytically the long range magneto-dipole interaction within samples. Hence, numerical methods must be used. From the point of view of fabrication and practical applications, MCs and devices with a planar geometry and, ideally, fabricated from a single magnetic material are preferred. MCs can be arranged in one dimensional (1D), two dimensional (2D) and three dimensional (3D) array of magnetic nanostructure and can be composed of one or more than one magnetic material.

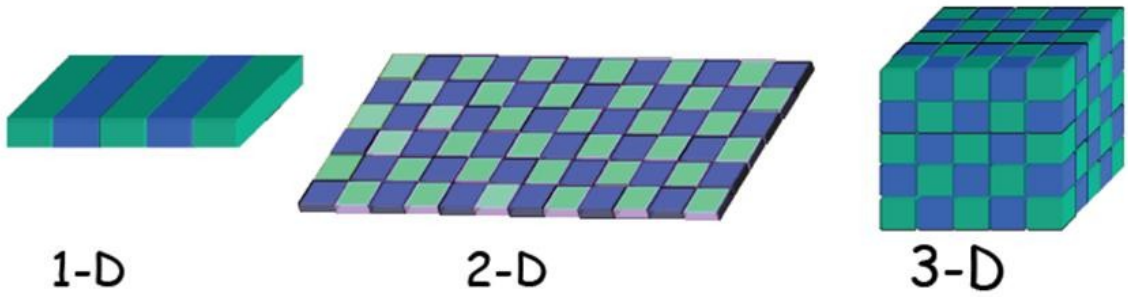

Fig. 1.1. Schematic representation of 1D, 2D and 3D MCs.

Planar 1D MCs are formed for example by stripes[52] or by chain of interacting dots of various shapes[53,54].The spectrum of magnons in closely packed 1D arrays of magnetic nanoelements was shown to have a band structure with Brillouin zone (BZ) boundaries determined by the artificial periodicity of the arrays. The 2D MCs consist for example of periodically arranged magnetic dots interacting along the two in plane directions. The position and the width of band gaps in spectrum were investigated as a function of the period of the structure and the depth of modulation of the magnetic parameters. It was found that the depth of the modulation of the exchange coupling constant has a drastic effect upon the position and width of the band gaps. An example of 2D MCs are antidots (ADs): ADs consist of a mesh of nonmagnetic holes embedded into a continuous magnetic film, and they have been proposed as candidates for ultrahigh density storage media. In recent years the static properties of ADs have been widely investigated. Now it is important to have a control also of dynamic properties since reading and writing speeds in magnetic storage devices are getting closer to the time scale of spin dynamics. In AD nanostructures, collective magnetic excitations in the form of Bloch waves can have a dispersive behaviour. The 3D MCs are ferromagnetic systems periodic along the *x*, *y* and *z* directions. Also for these kind of MCs, the dispersion curves calculated with respect to the different directions of the wave vector can have a dispersive behavior. 1D, 2D and 3D MCs can be composed both of a single ferromagnetic material or of different materials. In the second case the MCs are usually called multi-component MCs and their properties are different from the case of a single component MCs.

The eigenfrequencies of SWs are determined by the spin stiffness, the absolute value of the saturation magnetization, the Bloch wave vector, and the relative orientation between the magnetization vector and the wave vector. Depending on the hole size ranging from Angstroms to micrometers, SWs are dominated by short-range dynamic exchange interactions or long-range dipolar interactions. Both these interactions regulate the characteristic slope of the SW dispersion relation.

1.2 Magnonic metamaterials

Metamaterials are smart materials engineered to have properties that have not yet been found in nature. They are made from assemblies of multiple elements fashioned from composite materials such as metals or plastics. The materials are usually arranged in periodic patterns, at scales that are smaller than the wavelengths of the phenomena they influence. Metamaterials usually gain their properties from structure rather than composition, using small inhomogeneities to create effective macroscopic behavior. Their precise shape, geometry, size, orientation and arrangement give them their smart properties capable to manipulate electromagnetic waves: by blocking, absorbing, enhancing, bending waves, to achieve benefits that go beyond what is possible with conventional materials.

Exploiting non-volatility, multifunctional metamaterials might be formed. The primary research in metamaterials investigates materials with negative refractive index. Negative refractive index materials appear to permit the creation of super lenses which can have a spatial resolution below that of the wavelength.

On the other hand, great attention has been devoted to the investigation of MCs characterized by periodically modulated properties and where collective spin-wave modes can propagate. MCs are a new class of metamaterials. First of all it can be useful to clarify what means magnonic metamaterial and what makes a metamaterial different from a standard material. To give an explanation in the most general sense, it should be clarified first as to what makes standard (i.e., nature-made) materials. A standard material is composed of atoms and ions joined together to collectively create a novel quality with properties that are not observed in the constituent atoms in isolation. An example is the presence of discrete electronic energy levels and associated discrete electromagnetic spectra in isolated atoms. In the case of atoms inside a material, each discrete electronic level is split into a continuous “electronic band.” This is due to the fact that when atoms are part of a material, they collectively have new properties that are different with respect to those of isolated atoms. The properties of a material are mainly connected to their composition. The attempt of going beyond this concept led to the idea of a metamaterial. Unlike standard materials, metamaterials are artificial materials and their properties are mainly due to their structure. Historically, the first hint of materials with properties similar to those of metamaterials was attributed to Kock and applied to artificial dielectrics[55,56]. The first theoretical prediction of unconventional phenomena that cannot occur in usual materials and that are instead a feature of artificial materials was given by Veselago, who predicted the existence of electromagnetic materials with negative refractive index[57]. This phenomenon was confirmed experimentally about 30 years later by Smith et al. in split-ring resonators[58]. Generally speaking, most of the dynamical properties of metamaterials can be considered relative to excitations with wavelengths either comparable to or much greater than the characteristic size of the building blocks. The characteristic size in most cases is given by the periodicity of the system. The former case is associated with studies of artificial band gap crystals in, for example, photonic[59], plasmonic[60], phononic[61], and MCs[62]. In the latter case, the metamaterials

are treated in terms of effectively continuous media. However, the physical object under study is the same in both cases. For example, metamaterials with artificial periodic modulation of the refractive index with periodicity comparable to the wavelength of electromagnetic waves in the visible range are known as photonic BG structures. These structures are very important, because it is possible to manipulate the direction of propagation of light along given directions. Moreover, light propagation can be confined in chosen channels or zones or even prohibited. In the microwave frequency range, the same structures would behave as effectively continuous materials. In a particular frequency region of interest, the same metamaterials can behave differently with respect to excitations of different kinds, for example, electromagnetic, sound, or SWs. Attractive opportunities arise from the use of one of the previously cited excitations to design a resonance feature for another excitation with respect to which the structure behaves as a quasi-continuous metamaterial. For example, plasmonic resonances can be used to alter effective electromagnetic properties from THz to visible frequency range. Magnonic resonances can be used for the same purpose in GHz–THz frequency range. Periodically modulated magnetic materials have been shown to form MCs, that is, a magnetic analogue of photonic crystals.

1.3 Experimental technique: Brillouin Light Scattering

Among the many experimental techniques able to study the SWs in magnetic nanostructures, for the purposes of this Thesis it is useful to briefly describe the Brillouin Light Scattering (BLS) technique. The results presented in the Chapters 3 and 4 (Sect. 3.1 and 4.3) are critically compared with the BLS measurements performed at the Department of Physics and Geology of the University of Perugia. BLS technique is a powerful tool able to investigate SWs and acoustic phonons in nanometric and micrometric systems. The physical mechanism involved is the inelastic scattering between the light and the collective excitations. In a typical BLS experiment one measures SWs with frequencies in the range from 1 to 100 GHz. In order to detect the weak inelastic component of light from the elastically scattered contribution a high resolution spectrometer is required. In order to achieve this aim, a tandem Fabrì-Perot interferometer is the main component of the BLS apparatus. BLS spectra are recorded in the backscattering configuration by using a Sandercock-type high-contrast and high resolution (3+3) tandem Fabry-Pérot interferometer. The light source is a laser polarized in the incident plane (polarization p) with wavelength λ_i = 532 nm. By focusing the laser beam on the ferromagnetic sample it is possible to collected and directed towards the interferometer the scattered light. The Fabry-Pérot interferometer analyzes the presence of light with wavelength different from λ_i and the scattered light with wavelength $\lambda_i \neq \lambda_s$ is detected by the photomultiplier. A system made up of diaphragms and filters is used to select only a particular frequency range of light. A computer collects the photon number and shows the data. The BLS apparatus is shown in Fig. 1.2[63].

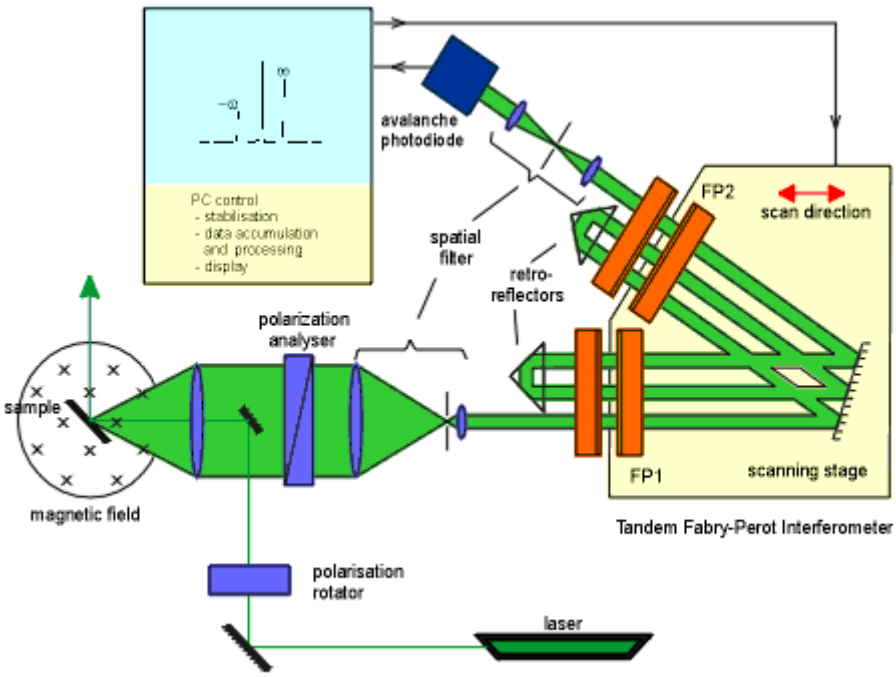

Fig. 1.2. BLS apparatus diagram.

When the light wave scatters on the magnetic system an inelastic process takes place. In particular, the incident light wave, with wavelength λ_i and wave vector $\boldsymbol{k}_i$, is scattered by a SW, with wavelength λ and wave vector $\boldsymbol{k}$. The wave characterized by λ and $\boldsymbol{k}$ is the SW created or destroyed by the incident light wave. The scattered light wave is characterized by frequency ω_s and wave vector $\boldsymbol{k}_s$. Wave vectors and frequencies of the components of this process must satisfy the following conservation rules:

$$\begin{aligned} \omega_S &= \omega_i \pm \omega \\ \boldsymbol{k}_S &= \boldsymbol{k}_i \pm \boldsymbol{k} \end{aligned} \tag{1.1}$$

These conservation rules are valid for infinite magnetic systems and are not fulfilled in laterally confined systems due to quantization effects. The sign + indicates the destruction of SW (Stokes process) and the sign – is referred to the creation of SW (anti-Stokes process). In a BLS experiment it is also important to detect SWs with different values of wave vector. In order to change the magnitude of the wave vector it is possible to vary the incidence angle θ of light on the sample. The wave vector of the SW and the incident angle are related by means of the following equation: $k = \frac{4\pi}{\lambda}\sin\theta$.

1.4 Theoretical background

The ferromagnetic nanostructures can be investigated from a theoretical point of view following three different approaches: the microscopic model, the macroscopic or analytical model and the micromagnetic approach. These models differ each other by their length scales. The first is based on the quantum

mechanical description of the phenomena and the length scale is minor than 1 nm. The macroscopic or analytical model describes the magnetic body from a macroscopic point of view giving an analytical description of the body and its length scale is higher than 1 micron. Between these two approaches it is placed the micromagnetic theory with a length scale that ranges from 1 nm to 1 micron and gives a continuous description of the magnetization. Recently, thanks to progress in the field of the micromagnetism, this approach allows to study magnetic properties in systems having dimension of 10 μm.

Model	Description	Length Scale
Microscopic theory	Quantum mechanical ab initio calculations	<1nm
Micromagnetic theory	Discretized description of the magnetization	1−1000nm
Macroscopic theory	Analytical description of the magnetization of the body	>1μm

Tab. 1.1. Three different theoretical approaches to the magnetism together with their lengths scale.

In the following subsections the microscopic and macroscopic models will be shortly presented while the micromagnetic approach will be described in detail since most of the results of this Thesis have been obtained by means of a micromagnetic method.

Before starting with the description of the previously introduced models, it can be useful to recall that the phenomena involved in the ferromagnetic materials arise from different spatial scales, going from few nanometers to few microns. In Fig. 1.3 it is shown a sketch of a short range interacting magnetic elements (left) and of a long range coupling magnetic element (right). The two different types of interactions depend on the distance between the two magnetic elements.

Fig. 1.3. Magnetic elements interacting by means of short range interaction and long range interaction.

In general, the fundamental interactions present in a ferromagnetic material are: Zeeman interaction, dipolar coupling, exchange interaction and the anisotropy term. Taking into account the different length scale of each interaction involved, it is possible to classify the exchange and the anisotropy interactions as short-range terms and the dipolar interactions as long-range interactions.

1.4.1 Microscopic approach

Historically, the first method developed is the microscopic theory of ferromagnetism which explain the origin of magnetism. This approach is based on an atomistic model where the spin of each atom **S** is individually considered in the Hamiltonian of the system. It is assumed that into ferromagnetic materials, at low temperature, the magnetic moments are parallel one to each other. The microscopic approach is used to study magnetic systems as the quantum dots, molecular magnetism and other magnetic systems where the quantum effects play a dominant role. It is also important to note that this model is not suitable to analyze ferromagnetic systems having macroscopic dimension (higher than 1 μm) because of the high number of atoms.

The Hamiltonian that describes the spin system responsible for the ferromagnetism in the microscopic approach is:

$$H = -J_{ij}\sum_{ij}\mathbf{S}_i\cdot\mathbf{S}_j - g\beta H_0\sum_i \mathrm{S}_i^z + \frac{1}{2}\sum_{ij}(g\beta)^2\left(\frac{\mathbf{S}_i\cdot\mathbf{S}_j}{\mathrm{r}_{ij}^3} - \frac{3(\mathbf{r}_{ij}\cdot\mathbf{S}_i)(\mathbf{r}_{ij}\cdot\mathbf{S}_j)}{\mathrm{r}_{ij}^5}\right) + D\sum_i\left(\mathrm{S}_i^z\right)^2 \qquad (1.2)$$

where β is the Bohr magneton, g is the Landè factor, $\mathbf{S}_i$ indicates the spin in the i lattice point, J_{ij} is the exchange constant between the two spin $\mathbf{S}_i$ and $\mathbf{S}_j$ and $\mathbf{r_{ij}}$ is the distance between the two spins. The first term of the Hamiltonian is the exchange energy term. It has an electrostatic origin but it is explained by means of the quantum mechanics; indeed, it can be described by means of the Heisenberg isotropic Hamiltonian and its energy levels do not depends on the direction in the space in which the ferromagnetic material is magnetized. The exchange coupling is characteristic of ferromagnetic systems where the interaction between two spins is considered and is not present in the theory of diamagnetic and paramagnetic materials. It is a short range interaction and it is calculated over all the atomic sites by taking into account the directions of two spin located at the sites i and j. J_{ij} is the exchange integral and it is related to the overlap of spatial terms of the wave functions of the electrons of the ferromagnetic material. The value of J_{ij} rapidly decreases when the distance between the two spin increases. By evaluating the value of J_{ij} it is possible to understand the configuration of the ground-state of the system: if $J_{ij} > 0$ the system is in the ferromagnetic state, if $J_{ij} < 0$ the system is in the anti-ferromagnetic state. This means that in the ferromagnetic (antiferromagnetic) state the energy associated to the exchange interaction is minimum (maximum) when $\mathbf{S}_i$ and $\mathbf{S}_j$ are parallel while it has the maximum (minimum) value for antiparallel alignment of $\mathbf{S}_i$ and $\mathbf{S}_j$. The second term of the Hamiltonian is the Zeeman energy and describes the interaction between the spin of each lattice site and the external magnetic field. The Zeeman term in Eq. (1.2) refers to the case of an external magnetic field applied along the z-axis and the sum is over each lattice point. The third term is the dipolar interaction and it corresponds to the first order term of the demagnetizing energy. This a long range interaction and the energy associated is minimum when $\mathbf{S}_i$ and $\mathbf{S}_j$ are in antiparallel configuration and is maximum if $\mathbf{S}_i$ and $\mathbf{S}_j$ are parallel to each

other. The last term is the energy contribution due to the anisotropy term that arises from the spin-orbit coupling. D is the anisotropy constant and for $D < 0$ there is an easy plane anisotropy while for $D > 0$ an easy axis anisotropy. The anisotropy term is not related to the direction of the external field and the associated energy is usually smaller that the exchange energy.

1.4.2 Macroscopic approach

The macroscopic model is based on the hypothesis that the magnetization of a ferromagnetic body is treated as a field $\mathbf{M}(\mathbf{r})$ instead of a single individual atomic spin $\mathbf{S}_i$ as occurs in the microscopic theory. The macroscopic model is usually called also continuum model for the ferromagnetism because the ferromagnetic material is considered as a continuum medium with a magnetization $\mathbf{M}(\mathbf{r})$ that is a slowly varying function of the spatial coordinates $\mathbf{r} = (x,y,z)$. If a ferromagnetic body having a volume V is considered, a small region of the body $dV_\mathbf{r}$ contains a number N of elementary magnetic moments $\mu_i = 1,\ldots, N$ and the average of the magnetic moments in the volume $dV_\mathbf{r}$ varies smoothly. In this respect the magnetization vector field $\mathbf{M}(\mathbf{r})$, such that the product between $\mathbf{M}(\mathbf{r})$ and $dV_\mathbf{r}$ is equal to net magnetic moment of the elementary $dV_\mathbf{r}$ is:

$$\mathbf{M(r)} = \frac{\sum_i \boldsymbol{\mu}_i}{dV_r} \tag{1.3}$$

The main advantage of the macroscopic approach with respect to the microscopic one is that the phenomenological parameters due to the anisotropy and the magnetostatic energies can be easily included in the macroscopic Hamiltonian. Moreover, the calculation of continuous quantities by means of integrals is quicker than the calculation of microscopic quantities by means of sums. Starting from the microscopic Hamiltonian it is possible to write the corresponding energy terms of the macroscopic approach. For all the energy contributions the summation over all the lattice sites is replaced with the integral calculated over the whole volume of the ferromagnetic object considered. The exchange energy among spins can be written in terms of the angles ϕ_{ij} between spin i and spin j. The angles between neighbours are expected to be small, because the exchange interaction is very strong over a short range and will not allow any large angle to develop. For small angles, $|\phi_{ij}| \approx |\boldsymbol{m}_i - \boldsymbol{m}_j|$ where $\boldsymbol{m}$ is the unit vector parallel to the local spin direction and also to the local direction of the magnetization vector since it is defined as $\boldsymbol{m} = \mathbf{M}(\mathbf{r}) / M_s$ where M_s is the saturation magnetization, a parameter characteristic of each material.

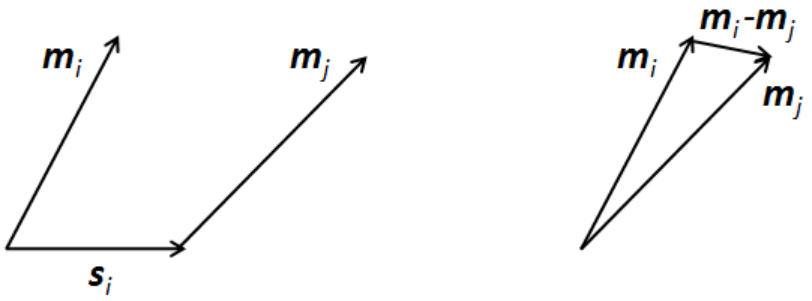

Fig. 1.4. Schematic representation of the change in the angle between spin *i* and *j* and the position vector $\mathbf{s}_i$ between them.

For such a variable, the first-order expansion in a Taylor series is $|\boldsymbol{m}_i - \boldsymbol{m}_j| = |(\mathbf{S}_i \cdot \nabla)\boldsymbol{m}|$ where $\mathbf{S}_i$ is the position vector pointing from the lattice point *i* to *j*. Moreover, in the macroscopic approach a new exchange constant *A* is introduced (more properly called exchange stiffness constant) and is linked to the exchange integral *J*, namely $A = 2JS^2/a$ where *a* is the edge of the unit cell. This definition of exchange stiffness is valid for a simple cubic lattice, similar relations can be obtained for different kind of lattices. From the macroscopic point of view, the Zeeman interaction can be easily obtained by replacing in Eq. (1.2) the summation over the lattice sites with the integral over all the volume of the element and by substituting $\mathbf{M}(\mathbf{r}) = \beta g \mathbf{S}_i$. In the macroscopic model the dipolar interaction, that corresponds to the first order of the demagnetizing field, can be obtained by inserting $\mathbf{M}(\mathbf{r_i}) = (2\mu_0/v_0) \langle \mathbf{S_i} \rangle$, where v_0 is the volume of the unit cell and $\langle \mathbf{S_i} \rangle$ indicates a statistical average, in the expression of the dipolar energy in the microscopic model. Following a macroscopic approach it is simple to introduce different types of anisotropies with respect to the microscopic model. There are several sources of magnetic anisotropy that is the directional dependence of a material's magnetic properties. The magnetocrystalline anisotropy is due to the atomic structure of a crystal that introduces preferential directions for the magnetization. The shape anisotropy term is taken into account when a particle is not perfectly spherical and the demagnetizing field is not equal for all directions, creating one or more easy axes. Moreover the magnetoelastic anisotropy is due to the tension that may alter magnetic behaviour, leading to magnetic anisotropy.

The most common anisotropy is the magnetocrystalline anisotropy that is an intrinsic property of the material, independent of size and shape of the magnetic element. It can be observed by measuring magnetization curves along different lattice directions. Magnetocrystalline anisotropy can be also regarded as the energy necessary to deflect $\mathbf{M}(\mathbf{r})$ from the easy to the hard direction. The second type of anisotropy is the shape anisotropy due to the finite shape of the body and corresponding to the demagnetizing magnetostatic energy. In this respect, in Fig. 1.5, left panel, it is shown a magnetized body that produces magnetic charges or poles at the surface. This surface charge distribution, acting in isolation, is itself another source of a magnetic field, called the demagnetizing field (see Fig. 1.5, right panel). It is called the demagnetizing field because it acts in opposition to the magnetization that produces it.

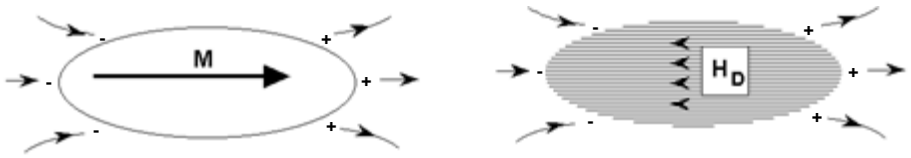

Fig. 1.5. Distribution of apparent surface pole produced by the magnetization. Demagnetizing field due to the apparent surface pole distribution.

In addition, in the macroscopic model there is another anisotropy term related to spin-orbit coupling called magnetostriction. Magnetostriction arises from the strain dependence of the anisotropy constants. After magnetization, a previously demagnetized crystal experiences a strain that can be measured as a function of applied field along the principal crystallographic axes. A magnetic material will therefore change its dimension when magnetized.

1.4.3 Micromagnetic approach

Micromagnetics is based on one hand on a continuum approximation of exchange interactions, including boundary conditions, on the other hand on Maxwell equations in the non-propagative limit for the evaluation of the demagnetizing field. The micromagnetic energy is most often restricted to the sum of the exchange, (self-)magnetostatic, Zeeman and anisotropy energies. The most important feature that characterize every micromagentic method is the discretization of the magnetic element in micromagnetic cells. When supplemented with a time evolution equation, including field induced magnetization precession, damping and possibly additional torque sources, micromagnetics allows for a precise description of magnetization distributions within finite bodies both in space and time. Analytical solutions are, however, rarely available. Numerical micromagnetics enables the exploration of complexity in small size magnetic bodies. The validity of the micromagnetic approach for the study of ferromagnetic nanostructures depends on the fundamental assumptions according to which, within a small region, a magnetization vector can be representative of the local average magnetic spins. This vector carries the sum of the atomic spins in a limited region or cell, and is ideally concentrated at the center of the cell itself, whose the magnetization is assumed uniform: this region has usually a nanometric extension. Among the micromagnetic methods it is possible to distinguish two main classes: micromagnetism based either on the finite-difference (FD) methods or on the finite-element (FE) methods.

The FD methods are widely used numerical method for finding approximate values of solutions of problems involving partial differential equations[64]. The basic idea consists of approximating the partial derivatives of a function by finite difference quotients. The process of replacing partial derivatives by FD quotients is known as a discretization process and the associated error is the discretization error. A partial differential equation can be changed to a system of algebraic equations by replacing the partial derivatives in the differential equation with their FD approximations. The system of algebraic equations can be solved numerically by an iterative process in order to obtain an approximate solution.

The FE methods are numerical techniques for finding approximate solutions to boundary value problems for partial differential equations. They use subdivision of a whole problem domain into simpler parts, called finite elements, and variational methods from the calculus of variations to solve the problem by minimizing an associated error function. Analogous to the idea that connecting many tiny straight lines can approximate a larger circle, FE methods encompass methods for connecting many simple element equations over many small sub domains to approximate a more complex equation over a larger domain. By comparing the two discretization methods it is possible to note that the most attractive feature of the FE methods is their ability to handle complicated geometries (and boundaries) with relative ease. While the FD methods in their basic form are restricted to handle rectangular shapes and simple alterations thereof due to the use of a rectangular lattice, the handling of geometries in the FE methods is theoretically straightforward. The most attractive feature of FD methods is that they can be very easy to implement.

Most of the results of this Thesis have been obtained by means of a micromagnetic approach, called DMM and OOMMF, that are a FD methods. In this respect, the energy contributions of each interaction involved in the ferromagnetic systems studied in this Thesis are now presented following the micromagnetic approach. The magnetic system is divided in prismatic cells where the thickness of the sample in the *z*-direction is indicated with L and l_c is the side of the square micromagnetic cell. In the case when the system is a 2D magnetic system, the thickness L of the sample is equal also to the height of the micromagnetic cell.

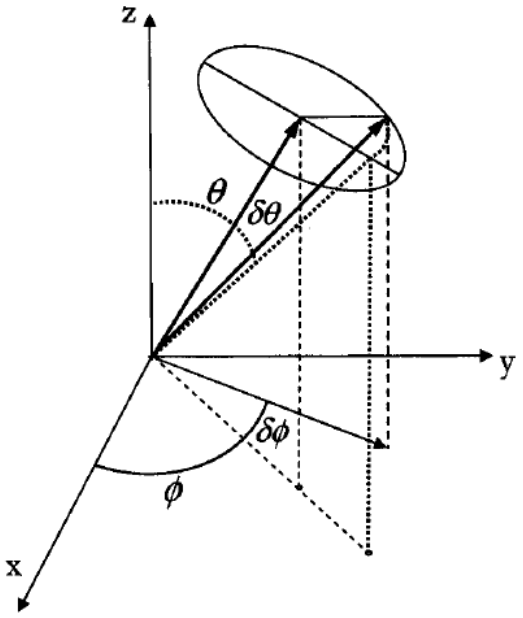

Fig. 1.6. Polar reference frame used in the micromagnetic method.

The reference frame is shown in Fig. 1.6. The *z*-axis is along the normal to the magnetic elements and the *x*-*y* plane lies on the particle plane. The studied sample is subdivided into rectangular micromagnetic cells. Each micromagnetic cell is identified by a single index that varies from 1 to N. Hence, M_k is the magnetization

in the k-th cell and $\boldsymbol{r}_{kj} = \boldsymbol{r}_k - \boldsymbol{r}_j$ is the distance between k-th cell and j-th cell. The index has been assigned so that the first line of the rectangular matrix *(X×Y)* corresponds to $k = 1,...,Y$ and the second line to $k = Y+1,...,2Y$ ecc. *X (Y)* is the number of cells along *x* (*y*), while *Z* is the number of cells along *z* for a sample of thickness equal to L.

The magnetization $\boldsymbol{m}_k = \boldsymbol{M}_k / M_S$ is expressed in a polar reference frame:

$$\boldsymbol{m}_k = (\sin\theta_k \cos\phi_k, \sin\theta_k \sin\phi_k, \cos\theta_k) \tag{1.4}$$

where ϕ_k is the azimuthal angle and θ_k is the polar angle of the magnetization. The total energy density of the system is a function of ϕ_k and θ_k: $E = E(\theta_k, \phi_k)$ where k varies from 1 to N. In particular, it has been evaluated the energy density that can be obtained by dividing the energy per volume cell.

In the following explicit expressions are given for the different interactions entering into the total micromagnetic energy density *E* of a given confined magnetic system: Zeeman, exchange, demagnetizing and anisotropy.

In the presence of an external magnetic field **H**, the Zeeman energy density can be written in the form

$$E_{\text{ext}} = -M_S \mathbf{H} \cdot \sum_{k=1}^{N} \boldsymbol{m}_k \tag{1.5}$$

In micromagnetic theory the exchange energy can be expressed as a volume integral of the form

$$\tilde{E}_{exch} = \frac{A}{M_S^2} \int_{part} \sum_{j=1}^{3} (\nabla M_j)^2 dV = A \int_{part} \sum_{j=1}^{3} (\nabla m_j)^2 dV. \tag{1.6}$$

where the subscript "part" denotes the volume of a general magnetic particle, *A* is the exchange stiffness constant and ∇ denotes the gradient applied to a given component of the magnetization. In this case the exchange contribution is independent of *z* and the derivatives are calculated as finite elements. Using the first-neighbours model, the exchange energy density can be written as follows:

$$E_{exch} = \frac{A}{l_c^2} \sum_{k=1}^{N} \sum_{n=1}^{4} (1 - \boldsymbol{m}_k \cdot \boldsymbol{m}_n) \tag{1.7}$$

where l_c is the micromagnetic cell size, *k* varies over all micromagnetic cells and the sum over *n* ranges over the neighbours of the *k* -th cell. If the *k* micromagnetic cells are situated at the edges, one must impose boundary conditions.

In order to calculate the demagnetizing energy density, the method of the demagnetizing tensor has been taken into account. In the following the term “dipolar” can replace the term “demagnetizing”, because the higher-order terms of the expansion vanish in the practical cases examined.

Generally, the dipolar energy density can be written as follows:

$$E_{dem} = \frac{1}{2}\sum_{kj} \boldsymbol{M}_k \cdot \overleftrightarrow{N}_{kj} \boldsymbol{M}_j - \frac{M_S^2}{2}\sum_{kj}(m_{xk}, m_{yk}, m_{zk}) \begin{pmatrix} N_{xx} & N_{xy} & N_{xz} \\ N_{yx} & N_{yy} & N_{yz} \\ N_{zx} & N_{zy} & N_{zz} \end{pmatrix} \begin{pmatrix} m_{xj} \\ m_{yj} \\ m_{zj} \end{pmatrix} \tag{1.8}$$

This equation includes self-energy; $N_{\alpha\beta} = N_{\alpha\beta}(\vec{r}_{kj})$, with $\alpha,\beta=x,y,z$ are the elements of demagnetization tensor. Each component of the demagnetizing tensor is related to the interaction between two rectangular surfaces defined here with S and S'. Under the assumption of uniform magnetization in the calculation of the demagnetizing field, by using a version of Gauss’s theorem the demagnetizing tensor can be written as

$$\overleftrightarrow{N}(\boldsymbol{r}_{kj}) = \frac{1}{V}\int_{S_k} d\boldsymbol{S} \int_{S_j} \frac{d\boldsymbol{S}'}{|\boldsymbol{r}-\boldsymbol{r}'|}. \tag{1.9}$$

where $V = l_c^2 L$.

The magnetocrystalline uniaxial anisotropy contribution is:

$$E_{ani} = \sum_{k=1}^{N} K^{(1)} \sin^2 \alpha_k = \sum_{k=1}^{N} K^{(1)}(1-\cos^2 \alpha_k) = \sum_{k=1}^{N} K^{(1)}\left[1-(\boldsymbol{m}_k \cdot \mathbf{u})^2\right] \tag{1.10}$$

where $K^{(1)}$ is the first-order anisotropy uniaxial coefficient that has the dimension of an energy density and **u** is the unit vector that indicates the preferential direction.

1.5 Spin waves

From a classical point of view, a SW represents a phase coherent precession of microscopic vectors of magnetization of the magnetic medium. From the equivalent quasi-particle point of view, SWs are known as magnons, which are boson modes of the spin lattice that correspond roughly to the phonon excitations of the nuclear lattice. As temperature increases, the thermal excitation of SWs reduces a ferromagnet's spontaneous magnetization. In Fig. 1.7 a schematic representation of the precession of the magnetization around the direction of the external magnetic field is depicted.

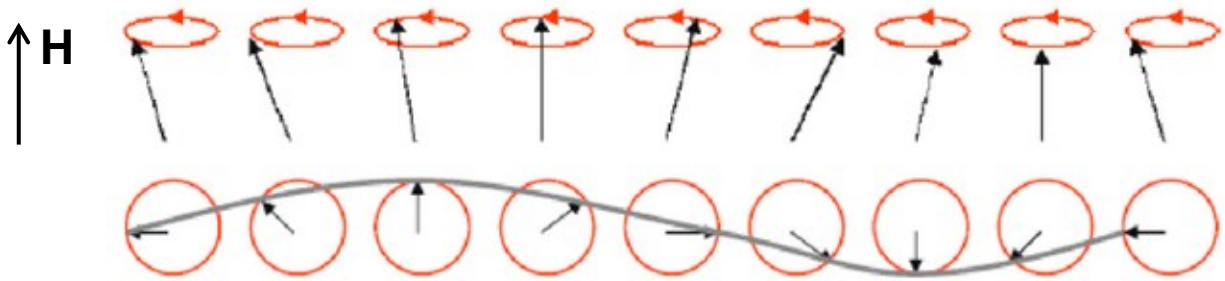

Fig. 1.7. Schematic representation of the dynamic magnetization together with the corresponding SW and the direction of the external magnetic field.

The first experimental evidence for the existence of SWs came from measurements of thermodynamic properties of ferromagnets, in particular the temperature dependence of the saturation magnetization. The Bloch law is an indirect confirmation of the existence of SWs in nature. The first direct observation of SWs was made using FMR for the case of uniform precession, which can be viewed as a SW with zero wave vector; later BLS experiments confirmed the existence of SWs with non-zero wave vectors. In some respects SWs can be considered as a magnetic analogue of the sound or light wave. Experimental and theoretical research have demonstrated that SWs exhibit most of the properties inherent in waves of other origin: excitation and propagation, interference and diffraction, focusing and self-focusing, tunneling of SWs and Doppler effect as well as formation of SW envelope solitons were observed. The main direction of magnonics is connected with the ability of SWs to carry and process information on the nanoscale. Research is particularly challenging since the SWs exhibit several peculiar characteristic that make them different from sound and light waves. In the case of thin ferromagnetic film, the dispersion relation $\omega(k)$ for SWs is highly dispersive and starts from $\omega_0 = \omega$ ($k = 0$) that depends on the strength and orientation of the applied magnetic field as well as on the size of the ferromagnetic sample. The SWs in a ferromagnetic continuous thin film propagate in the whole structure. As an example are the called Damon-Esbach surface modes[65] and the backward mode. In addition, $\omega(k)$ law is anisotropic even in the case of an isotropic magnetic medium. SWs are also governed by different interactions dominating on different length scales: the exchange and the dipolar interactions dominate on nanometer and micrometre length scales, respectively [66]. The Fig. 1.8(a) shows an approximate trend of the dispersion relation when different interactions dominates the frequency expression of the SWs. In Fig. 1.8(b) the range of wave vector in which each interaction has the dominant role in the determination of the SWs frequency is shown.

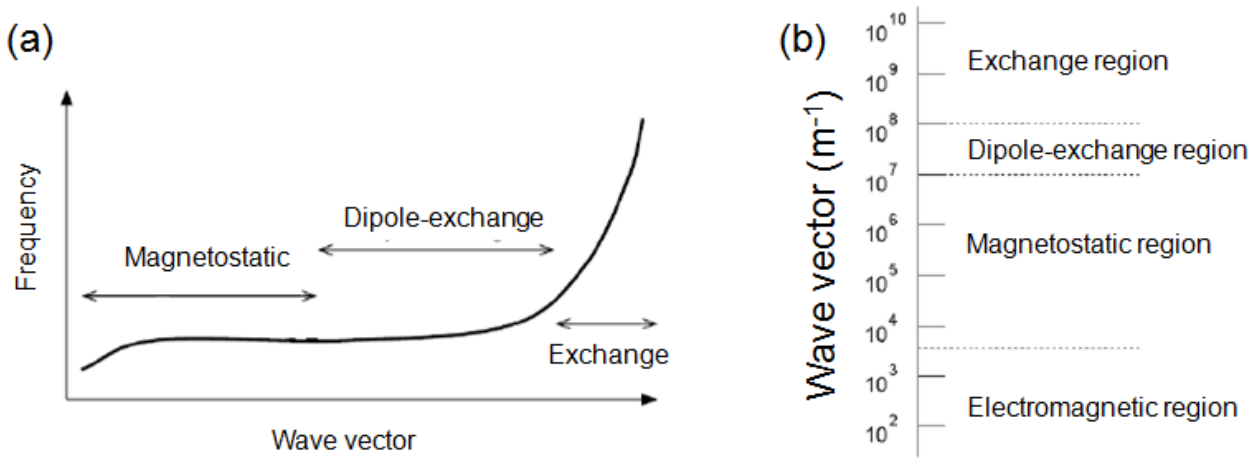

Fig. 1.8. (a) Indicative dispersion relation of SW together with the three different range interaction. (b) Different range for the interactions that influence the SW frequencies.

Recently SWs are observed and extensively studied in laterally confined magnetic structures and in these media SWs quantization is observed. SWs quantization is due to the lateral finite size effect. Very interesting properties associated to the laterally confined isolated nanostructures are found in the SWs spectrum: in magnetic elements of different shapes and of different materials, the SW modes have almost flat bands[67,68]. Because of the small lateral dimensions, dots are in a single domain state and their magnetization orientation is changed in a domino like cascade whereby the orientation of the magnetization propagates along a line or inside a cluster of dots coupled by magnetic stray field between elements. In the elements of a closely packed array, the standing waves of individual elements interact via dynamic dipolar magnetic coupling and from collective spin excitations which show dispersive behaviour. These waves can be assumed to be Bloch-type modes[69]. Periodically structured materials play a special role in magnonics. Periodically modulated materials are now explored to form MCs that are the analogue of photonic crystals. The SW spectrum has been modified by patterning and shows a tailored band structure in periodic magnetic materials. The band spectrum consists of bands of allowed magnonic states and forbidden frequency gaps in which there are no allowed magnonic states. MCs have been created to have full control of SWs, similarly to what photonic crystals already do for light: such crystals represent the magnetic medium in which the magnetic properties are varied periodically.

Chapter 2

Dynamical Matrix Method: Micromagnetic Formalism

Chapter 2 is devoted to the micromagnetic methods used to investigate the properties of the magnetic nanostructures treated in this Thesis. Static properties of the magnetization in magnetic systems have been calculated by means of the Object Oriented MicroMagnetic Framework (OOMMF)[49] while to study the dynamical properties the Dynamical Matrix Method (DMM)[51] has been used. The dynamic matrix approaches has been widely used in molecular dynamics but it can be applied to the magnetic structures. It relates the oscillating properties of the magnetization to the results of a dynamical matrix calculation, especially in the context of micromagnetism. The DMM is a power software able to determine the frequencies and spatial profiles of all spin-wave modes in a single calculation. Through the use of both the OOMMF and DMM code, the outcome of the first as a input file of the latter, it is possible to determine with high accuracy the properties of magnetic nanostructures having different shapes, materials and geometries.

In the Section 2.1 the OOMMF code is briefly described for the calculation of the static properties of the magnetization in magnetic nanostructures. The OOMMF software allows the analysis of the ground-state of the magnetization in non-interacting elements, periodic systems and single or multimaterials systems. The Section 2.2 presents the DMM in the case of non-interacting elements together with the details of the

calculation of the derivatives of the energy terms. In Section 2.3, the DMM is presented for interacting elements, and in Section 2.4 for the case of multicomponent interacting elements. The DMM presents several advantages with respect to other micromagnetic methos: *a)* all the modes are obtained in a single calculation giving both frequencies and eigenvectors (i.e. dynamical magnetization profiles), *b*) the spectrum is computed directly in the frequency domain, *c*) the mode degeneracy is successfully solved, *d*) the spatial profiles of the spin-wave modes are directly determined as eigenvectors and, finally, *e*) the differential scattering cross-section can be calculated accurately from the eigenvectors associated to each spin-wave.

2.1 Object Oriented MicroMagnetic Framework

At the present, several software based on micromagnetism have been developed to study the static and dynamic properties of the magnetization in magnetic nanostructures. In particular, OOMMF is a public domain software produced by the National Institute of Standards and Technology[49]. Given a problem description, the OOMMF code integrates the Landau-Lifshitz Gilbert (LLG) equation:

$$\frac{d\boldsymbol{m}}{dt} = -\gamma\left(\boldsymbol{m}\times\mathbf{H}_{\mathbf{eff}}\right) + \frac{\alpha}{M_s}\left(\boldsymbol{m}\times\frac{d\boldsymbol{m}}{dt}\right) \tag{2.1}$$

where α is the Gilbert damping coefficient and $\mathbf{H}_{\mathbf{eff}}$ is the effective field that includes the Zeeman field, the exchange field, the demagnetizing field and the anisotropy field. In this Thesis the systems are studied is a conservative regime and according to this hypothesis the damping coefficient is set equal to zero (α = 0).

According to this approximation the Eq. 2.1 reduces to the Landau-Lifshitz (LL) equation

$$\frac{d\boldsymbol{m}}{dt} = -\gamma\left(\boldsymbol{m}\times\mathbf{H}_{\mathbf{eff}}\right) \tag{2.2}$$

The integration is stopped and the equilibrium is reached when the maximum value of the torque $\frac{\left|\boldsymbol{m}\times\mathbf{H}_{\mathbf{eff}}\right|}{M_s^2}$ is below a specific value imposed in the problem description. Thanks to OOMMF it is possible to determine the ground-state of the magnetization in magnetic nanostructures composed by one or several ferromagnetic materials and for isolated or periodic nanostructures.

2.2 Dynamical matrix method for non-interacting elements

2.2.1 Dynamic equations

The total energy density is given by $E = E_{ext} + E_{exch} + E_{dem} + E_{ani}$ where the different contributions are expressed in Chap. 1, Sect. 1.2.3. The second derivatives of the energy density terms are included into the dynamic equation, their expression will be shown in the next sections. Note that the system is supposed to be governed by a purely precessional motion. Hence, within this formalism, the intrinsic Gilbert damping is not taken into account in the spin dynamics. This means that the dynamic is conservative and is thus described by an Hamiltonian formalism. Hence, it is possible to derive from the Hamilton equations applied to a magnetic dipole the following linear and homogeneous system of equations in which are included the second derivatives of the energy density calculated at the equilibrium. The variables are, of course, the small variations of the angles: $\delta\theta_k$ and $\delta\phi_k$. In particular, the energy density can be expressed as a power Taylor expansion up to the second order in the form

$$E = E_0 + \frac{1}{2}\sum_{k=1}^{N}\sum_{l=1}^{N}\left[E_{\phi_k\phi_l}\delta\phi_k\delta\phi_l + 2E_{\phi_k\theta_l}\delta\phi_k\delta\theta_l + E_{\theta_k\theta_l}\delta\theta_k\delta\theta_l \right] \tag{2.3}$$

By substituting the energy density of Eq. (2.3) into the Hamilton equations yields the $2N$ system of linear and homogeneous equations for k=1,...N:

$$\begin{cases} \sum_{l=1}^{N}\left(-\frac{E_{\theta_k\phi_l}}{\sin\theta_k}\right)\delta\phi_l + \sum_{l=1}^{N}\left(-\frac{E_{\theta_k\theta_l}}{\sin\theta_k}\right)\delta\theta_l - \tilde{\lambda} \\ \sum_{l=1}^{N}\left(\frac{E_{\phi_k\phi_l}}{\sin\theta_k}\right)\delta\phi_l + \sum_{l=1}^{N}\left(\frac{E_{\phi_k\theta_l}}{\sin\theta_k}\right)\delta\theta_l - \tilde{\lambda} \end{cases} \tag{2.4}$$

with

$$\tilde{\lambda} \quad \gamma \tag{2.5}$$

the eigenvalues of the problem. The sum is extended over the total number of the micromagnetic cells. The unknown factors $\delta\phi_l, \delta\theta_l$ represent the eigenvectors of the problem and are expressed by the small angular deviation from the equilibrium position of the azimuthal (ϕ_l) and polar (θ_l) angles in the l-th micromagnetic cell. The system above has a solution only if the determinant is zero. By suitable exchanges

of rows (columns) the linear and homogeneous system given in Eq.(2.4) can be written as an eigenvalue problem:

$$C\mathbf{v} = \lambda\mathbf{v} \qquad . \tag{2.6}$$

In Eq.(2.6), **v** is the set of the unknown factors representing the eigenvectors of the problem that take the form

$$\mathbf{v} = \begin{pmatrix} d\phi_1 \\ d\theta_1 \\ d\phi_2 \\ d\theta_2 \\ . \\ . \\ d\phi_N \\ d\theta_N \end{pmatrix} \tag{2.7}$$

C is the matrix whose elements are expressed as

$$\left.\begin{aligned} \mathrm{C}_{2k-1,2l-1} &= -\frac{E_{\theta_k\phi_l}}{\sin\theta_k} \\ \mathrm{C}_{2k-1,2l} &= -\frac{E_{\theta_k\theta_l}}{\sin\theta_k} \\ \mathrm{C}_{2k,2l-1} &= \frac{E_{\phi_k\phi_l}}{\sin\theta_k} \\ \mathrm{C}_{2k,2l} &= \frac{E_{\phi_k\theta_l}}{\sin\theta_k} \end{aligned}\right\} k = 1....N, \quad l = 1....N. \tag{2.8}$$

The matrix C can be seen as composed by two submatrices 2×2 for each pair of values (k,l). In the diagonal submatrices $(k = l)$ the following relation is verified:

$$C_{2k-1,2k-1} = -C_{2k,2k} \tag{2.9}$$

For the elements of two different submatrices (k,l) e (l,k), that are not diagonal $(k \neq l)$, are valid the following symmetries:

$$
\begin{aligned}
&\sin\theta_k C_{2k-1,2l-1} = -\sin\theta_l C_{2l,2k} \\
&\sin\theta_k B_{2k-1,2l} = \sin\theta_l C_{2l-1,2k} \\
&\sin\theta_k C_{2k,2l-1} = \sin\theta_l C_{2l,2k-1} \\
&\sin\theta_k C_{2k,2l} = -\sin\theta_l C_{2l-1,2k-1}.
\end{aligned}
\tag{2.10}
$$

The following sections are devoted to the calculation of the second derivatives of the energy terms that are considered.

2.2.2 Derivatives of the energy densities

As the dynamical matrix components are expressed in terms of the second derivatives of the energy density it is necessary to calculate them from the expressions given in Chap.1 Sect. 1.2.3. The first and second derivatives of the magnetization have been calculated with respect to the polar and azimuthal angles of the given micromagnetic cell that represent the degrees of freedom of the system. Indeed, the second derivatives of the magnetization appear in the final expressions of the second derivatives of the energy density.

$$
\begin{aligned}
&\frac{\partial \boldsymbol{m}_k}{\partial \phi_k} = (-\sin\theta_k \sin\phi_k, \sin\theta_k \cos\phi_k, 0) \\
&\frac{\partial \boldsymbol{m}_k}{\partial \theta_k} = (\cos\theta_k \cos\phi_k, \cos\theta_k \sin\phi_k, -\sin\theta_k) \\
&\frac{\partial^2 \boldsymbol{m}_k}{\partial \phi^2_k} = (-\sin\theta_k \cos\phi_k, -\sin\theta_k \sin\phi_k, 0) \\
&\frac{\partial^2 \boldsymbol{m}_k}{\partial \phi_k \partial \theta_k} = (-\cos\theta_k \sin\phi_k, \cos\theta_k \cos\phi_k, 0) \\
&\frac{\partial^2 \boldsymbol{m}_k}{\partial \theta^2_k} = (-\sin\theta_k \cos\phi_k, -\sin\theta_k \sin\phi_k, -\cos\theta_k).
\end{aligned}
$$

The first derivative of the Zeeman energy density is

$$
\frac{\partial E_{ext}}{\partial \theta_k} = -M_S \boldsymbol{H} \cdot \frac{\partial \boldsymbol{m}_k}{\partial \theta_k} \tag{2.11}
$$

therefore the second derivative becomes:

$$\frac{\partial^2 E_{ext}}{\partial\theta_k\partial\theta_l}=\begin{cases}-M_S\boldsymbol{H}\cdot\dfrac{\partial^2\boldsymbol{m}_k}{\partial\theta_k\partial\theta_l} & l=k\\ 0 & l\neq k\end{cases} \tag{2.12}$$

As outlined in Chap.1, Sect.1.2.3, for the calculation of the exchange contribution the nearest-neighbour model is taken into account. The first derivative with respect to θ_k includes in the sum a term in which $i=k$ and thus $n\neq k$ and also the other terms with $n=k$ and with i one of the nearest-neighbours. Thanks to a proper change of indices in the second term, the following equation is obtained:

$$\frac{\partial E_{exch}}{\partial\theta_i}=-\frac{A}{a^2}\sum_{n=1}^{4}\frac{\partial\boldsymbol{m}_k}{\partial\theta_k}\cdot\boldsymbol{m}_n-\frac{A}{a^2}\sum_{n=1}^{4}\boldsymbol{m}_n\cdot\frac{\partial\boldsymbol{m}_k}{\partial\theta_k}=-\frac{2A}{a^2}\sum_{n=1}^{4}\frac{\partial\boldsymbol{m}_k}{\partial\theta_k}\cdot\boldsymbol{m}_n \tag{2.13}$$

where the sum over n is made up over the nearest-neighbour cells of the k-th cell.

In the special case of the adopted first neighbours model, the second derivatives are

$$\frac{\partial^2 E_{exch}}{\partial\theta_k\partial\theta_l}=\begin{cases}-\dfrac{2A}{l_c^2}\sum_{n=1}^{4}\dfrac{\partial^2\boldsymbol{m}_k}{\partial\theta_k\partial\theta_l}\cdot\boldsymbol{m}_n & l=k\\ -\dfrac{2A}{l_c^2}\dfrac{\partial\boldsymbol{m}_k}{\partial\theta_k}\cdot\dfrac{\partial\boldsymbol{m}_l}{\partial\theta_l} & l,k:\,nearest-neighbour\\ 0 & other\ cases\end{cases} \tag{2.14}$$

The first derivative of the dipolar energy density, calculated according to the demagnetizing tensor is

$$\begin{aligned}\frac{\partial E_{dip}}{\partial\theta_k}&=M_S^2\left[\frac{1}{2}\sum_{i\neq k}\boldsymbol{m}_k\cdot\overleftrightarrow{N}(k,i)+\frac{1}{2}\sum_{j\neq i}\frac{i}{\partial\theta_i}\cdot\overleftrightarrow{N}(i,j)\boldsymbol{m}_j+\frac{1}{2}\frac{}{\partial\theta_i}(\boldsymbol{m}_i\cdot\overleftrightarrow{N}(i,i)\boldsymbol{m}_i\right]=\\ &=M_S^2\sum_{k=1,i\neq k}^{N}\boldsymbol{m}_k\cdot\overleftrightarrow{N}(k,i)\frac{i}{\partial\theta_i}+\boldsymbol{m}_i\cdot\overleftrightarrow{N}(i,i)\frac{i}{\partial\theta_i}.\end{aligned} \tag{2.15}$$

In the sum, the contribution of the terms with the same index $k=j=i$ has been separated; moreover by taking into account that the tensor $\overleftrightarrow{N}$ is even, namely $\overleftrightarrow{N}(i,j)=\overleftrightarrow{N}(j,i)$ and symmetric ($N_{nm}=N_{mn}$). Thanks to the previous consideration, it is possible to write whitin the expression of the first derivative

$$\frac{\partial\boldsymbol{m}_k}{\partial\theta_k}\cdot\overleftrightarrow{N}(k,i)\boldsymbol{m}_i-\boldsymbol{m}_i\cdot\overleftrightarrow{N}(k,i)\frac{\boldsymbol{i}_k}{\partial\theta_k} \tag{2.16}$$

and therefore:

$$\frac{\partial}{\partial\theta_i}\left(\boldsymbol{m}_i\cdot\overleftrightarrow{N}(i,i)\boldsymbol{m}_i\right)-\frac{i}{\partial\theta_i}\cdot\overleftrightarrow{N}(i,i)\boldsymbol{m}_i+\boldsymbol{m}_i\cdot\overleftrightarrow{N}(i,i)\frac{i}{\partial\theta_i}=$$
$$=2\boldsymbol{m}_i\cdot\overleftrightarrow{N}(i,i)\frac{\boldsymbol{m}_i}{\partial\theta_i} \tag{2.17}$$

By using Eqs.(2.16-2.17) one obtains the last member of Eq.(2.15).

The second derivative must take into account the two cases: $i\neq l, i=l(j=i)$

$$\frac{\partial^2 E_{dip}}{\partial\theta_l\partial\theta_i}=\begin{cases}M_S^2\left(\sum_{k=1}^{N}\boldsymbol{m}_k\cdot\overleftrightarrow{N}(k,l)\frac{l}{\partial\theta_l\partial\theta_i}+\frac{l}{\partial\theta_l}\cdot\overleftrightarrow{N}(l,i)\frac{i}{\partial\theta_i}\right) & l=i\\ M_S{}^2\frac{\partial\boldsymbol{m}_l}{\partial\theta_l}\cdot\overleftrightarrow{N}(l,i)\frac{\boldsymbol{m}_i}{\partial\theta_i} & l\neq i.\end{cases} \tag{2.18}$$

The $k=i$ term resulting from the derivative of the second term has been included in the sum over *k*.

The first derivative of the anisotropy term is:

$$\frac{\partial E_{ani}}{\partial\theta_k}=-K^{(1)}2(\boldsymbol{m}_k\cdot\mathbf{v})\cdot(\frac{\partial\boldsymbol{m}_k}{\partial\theta_k}\cdot\mathbf{v}) \tag{2.19}$$

and the second derivative results:

$$\frac{\partial^2 E_{ani}}{\partial\phi_j\partial\theta_k}=\begin{cases}-2K^{(1)}\left[(\frac{\partial\boldsymbol{m}_k}{\partial\phi_j}\cdot\mathbf{v})\cdot(\frac{\partial\boldsymbol{m}_k}{\partial\theta_k}\cdot\mathbf{v})+(\boldsymbol{m}_k\cdot\mathbf{v})\cdot(\frac{\partial^2\boldsymbol{m}_k}{\partial\phi_j\partial\theta_k}\cdot\mathbf{v})\right] & \text{for } \theta,\phi\\ -2K^{(1)}\left[(\frac{\partial\boldsymbol{m}_k}{\partial\phi_k}\cdot\mathbf{v})^2+(\boldsymbol{m}_k\cdot\mathbf{v})\cdot(\frac{\partial^2\boldsymbol{m}_k}{\partial\phi_k{}^2}\cdot\mathbf{v})\right] & \text{for } \phi,\phi \text{ or } \theta,\theta\end{cases} \tag{2.20}$$

$$\frac{\partial^2 E_{ani}}{\partial\phi_j\partial\theta_k}=0 \qquad k\neq j \tag{2.21}$$

2.2.3 Generalized Hermitian eigenvalue problem

The equations of motion can be recast as a generalized Hermitian eigenvalue problem:

$$A\mathbf{v} = \lambda B\mathbf{v} \tag{2.22}$$

where B is a Hessian matrix expressed by the second derivatives of the energy density at equilibrium. B is given by:

$$\left.\begin{aligned} B_{2k-1,2l-1} &= E_{\phi_k\phi_l} \\ B_{2k-1,2l} &= E_{\phi_k\theta_l} \\ B_{2k,2l-1} &= E_{\theta_k\phi_l} \\ B_{2k,2l} &= E_{\theta_k\theta_l} \end{aligned}\right\} k = 1....N, \quad l = 1...N; \tag{2.23}$$

The matrix A is an Hermitian matrix:

$$A = \begin{pmatrix} 0 & i\sin\theta_1 & 0 & 0 & ... \\ -i\sin\theta_1 & 0 & 0 & 0 & ... \\ 0 & 0 & 0 & i\sin\theta_2 & ... \\ 0 & 0 & -i\sin\theta_2 & 0 & ... \\ ... & & & & ... \end{pmatrix} \tag{2.24}$$

and $\lambda = \dfrac{\gamma}{M_S\omega}$ are the eiegenvalues.

The matrix B is symmetric (also in the case of interacting dots). Moreover, since the static magnetization corresponds to a minimum of the energy and the matrix B is its Hessian, the matrix B is also defined positive. The matrix A is Hermitian. This allows to solve the system as a generalized eigenvalue Hermitian problem. To further reduce the numerical calculation time it is possible to evaluate only some eigenvalues and eigenvectors (that are in a specific range). Once the eigenvectors $\mathbf{v}$ are obtained, the dynamic magnetization $\delta\boldsymbol{m}_k$ in Cartesian coordinates and in unit of M_S is given by :

$$\delta\boldsymbol{m}_k = \left(-\sin\theta_k\sin\phi_k\delta\phi_k + \cos\theta_k\cos\phi_k\delta\theta_k, \sin\theta_k\cos\phi_k\delta\phi_k + \cos\theta_k\sin\phi_k\delta\theta_k, -\sin\theta_k\delta\theta_k\right) \tag{2.25}$$

For each solution of eigenvalue problem, the collection of all $\delta \boldsymbol{m}_k$ defines the mode profile. It must be remarked that $\delta \boldsymbol{m}_k$ is a complex vector, because $\delta\theta_k, \delta\phi_k$ are, in general, complex.

The expression of the components of the generic dynamic magnetization $\delta \boldsymbol{m}$:

$$\delta \boldsymbol{m} = \frac{\partial \boldsymbol{m}}{\partial \phi}\delta\phi + \frac{\partial \boldsymbol{m}}{\partial \theta}\delta\theta = (-\sin\theta\ \sin\phi\ \delta\phi + \cos\theta\ \cos\phi\ \delta\theta, \sin\theta\ \cos\phi\ \delta\phi + \cos\theta\ \sin\phi\ \delta\theta, -\sin\theta\ \delta\theta) \quad (2.26)$$

yielding to $|\delta \boldsymbol{m}|^2 = \sin^2\theta\delta\phi^2 + \delta\theta^2$.

Thanks to these equations, the tangential and the radial components of the dynamic magnetization can be calculated in the *k*-th micromagnetic cell.

$$\alpha_k = -\tan^{-1}\frac{x_k}{y_k} + \pi \quad \text{if } y_k < 0$$

$$\delta m_t = \cos\alpha_k \delta m_x + \sin\alpha_k \delta m_y$$
$$\delta m_r = -\sin\alpha_k \delta m_x + \cos\alpha_k \delta m_y.$$

with α_k the angle between the radial direction and *x*-axis in the k-th cell. The tangential component is oriented clockwise whereas the radial component is oriented outward.

2.3 Dynamical matrix method for interacting elements

The DMM is also extended to interacting and periodic system . Let's suppose to have a 2D periodic array of interacting nanodots characterized by the primitive $\boldsymbol{a}_1$ and $\boldsymbol{a}_2$; for example, for the specific case of a rectangular lattice their values are $\boldsymbol{a}_1=\lambda_x \mathbf{x}$ and $\boldsymbol{a}_2=\lambda_y \mathbf{y}$ where λ_x and λ_y represent the periodicity along *x*-axis and *y*-axis. The primitive vector of the reciprocal lattice are $\boldsymbol{b}_1$ and $\boldsymbol{b}_2$ and result $\boldsymbol{b}_1 = 2\pi\frac{(\boldsymbol{a}_2\times\boldsymbol{a}_1)\times\boldsymbol{a}_2}{(\boldsymbol{a}_1\times\boldsymbol{a}_2)^2}$ and $\boldsymbol{b}_2 = 2\pi\frac{(\boldsymbol{a}_1\times\boldsymbol{a}_2)\times\boldsymbol{a}_1}{(\boldsymbol{a}_1\times\boldsymbol{a}_2)^2}$. For the specific case of a rectangular lattice the primitive vectors become $\boldsymbol{b}_1 = \frac{2\pi}{\lambda_x}\boldsymbol{x}$ and $\boldsymbol{b}_2 = \frac{2\pi}{\lambda_y}\boldsymbol{y}$. Thanks to the analogy with the Bloch wave (analogy and not identity, because the wave function has not a physical meaning like instead has the magnetization) it is possible to write the following periodicity rule valid for the dynamic magnetization

$$\delta \boldsymbol{m}(\boldsymbol{r}+\boldsymbol{R}) = e^{i\boldsymbol{K}\cdot\boldsymbol{R}}\delta \boldsymbol{m}(\boldsymbol{r}) \tag{2.27}$$

where $\boldsymbol{R}$ is a vector of the lattice defined as

$$\boldsymbol{R} = i_1\boldsymbol{a}_1 + i_2\boldsymbol{a}_2 \tag{2.28}$$

With $i_1, i_2 \in \mathbb{Z}$ ir values are in the range $i_1, i_2 = -\frac{N_i}{2}....\frac{N_i}{2} - 1;$ and $\boldsymbol{r}$ is confined into the first cell and the Bloch vector takes the following values: $\boldsymbol{K} = \frac{n_1}{N_1}\boldsymbol{b}_1 + \frac{n_2}{N_2}\boldsymbol{b}_2,$ $n_i \in \mathbb{Z}$ $= -\frac{N_i}{2}....\frac{N_i}{2} - 1;$ $N_1, N_2 \in \mathbb{N}$ and they are even natural numbers and indicate the number of cells n in direction $\boldsymbol{a}_1$ and $\boldsymbol{a}_2$ respectively. In order to confirm the hypothesis on the magnetization N_1, N_2 must be very large.

2.3.1 Equation of motion

If the magnetizations of the different primitive cells and of the different micromagnetic cells were independent, then one would have a dynamic system with variables $\theta_{k\boldsymbol{R}}$ and $\phi_{k\boldsymbol{R}}$, where the k index changes inside the magnetic particle and $\boldsymbol{R}$ can assume the values indicated in Eq. (2.28). In this case the system of 2*N* linear and homogeneous equations of motion is

$$\begin{cases} \sum_{l,\boldsymbol{R}'}\left(-\frac{E_{\theta_{k_R}\phi_{l_R}'}}{\sin\theta_{k\boldsymbol{R}}}\right)\delta\phi_{l\boldsymbol{R}'} + \sum_{l,\boldsymbol{R}'}\left(-\frac{E_{\theta_{k_R}\theta_{l_R}'}}{\sin\theta_{jk\boldsymbol{R}}}\right)\delta\theta_{l\boldsymbol{R}'} - \lambda\,\delta\phi_{k\boldsymbol{R}} = 0 \\ \sum_{l,\boldsymbol{R}'}\left(\frac{E_{\phi_{k_R}\phi_{l_R}'}}{\sin\theta_{k\boldsymbol{R}}}\right)\delta\phi_{l\boldsymbol{R}'} + \sum_{l,\boldsymbol{R}'}\left(\frac{E_{\phi_{k_R}\theta_{l_R}'}}{\sin\theta_{k\boldsymbol{R}}}\right)\delta\theta_{l\boldsymbol{R}'} - \lambda\,\delta\theta_{k\boldsymbol{R}} = 0 \end{cases} \tag{2.30}$$

where the sums over l runs from 1 to *N,* $k = 1...N$, $\boldsymbol{R}$ is expressed in Eq.(2.28) , the sum over $\boldsymbol{R'}$ is on the same values of $\boldsymbol{R}$ and with $\lambda = i\frac{M_S}{\gamma}\omega$ the eigenvalues of the problem. Instead, thanks to the Bloch condition expressed in Eq. (2.27), one can consider the equations only at $\boldsymbol{R}$ =0; moreover, taking into account the same condition, the variables appearing for $\boldsymbol{R'}\neq\boldsymbol{0}$ can be replaced by using the same condition. Now,

rewriting the system, the index $\boldsymbol{R}$ is omitted when it has value equal to 0 or is irrelevant. Owing to these considerations, the system given in Eq.(2.30) can be rewritten in the form

$$\begin{cases} \sum_{l=1}^{N}\left(-\frac{\sum_{\boldsymbol{R}'} E_{\theta_k\phi_{l_R}} e^{i\boldsymbol{K}\cdot\boldsymbol{R}'}}{\sin\theta_k}\right)\delta\phi_l + \sum_{l=1}^{N}\left(-\frac{\sum_{\boldsymbol{R}'} E_{\theta_k\theta_{l_R}} e^{i\boldsymbol{K}\cdot\boldsymbol{R}'}}{\sin\theta_k}\right)\delta\theta_l - \lambda\,\delta\phi_k = 0 \\ \sum_{l=1}^{N}\left(\frac{\sum_{\boldsymbol{R}'} E_{\phi_k\phi_{l_R}} e^{i\boldsymbol{K}\cdot\boldsymbol{R}'}}{\sin\theta_k}\right)\delta\phi_l + \sum_{l=1}^{N}\left(\frac{\sum_{\boldsymbol{R}'} E_{\phi_k\theta_{l_R}} e^{i\boldsymbol{K}\cdot\boldsymbol{R}'}}{\sin\theta_k}\right)\delta\theta_l - \lambda\,\delta\theta_k = 0 \end{cases} \tag{2.31}$$

Eq.(2.31) is similar to Eq.(2.4) making the following replacement

$$E_{\alpha_k\beta_l} \rightarrow \sum_{\boldsymbol{R}'} e^{i\boldsymbol{K}\cdot\boldsymbol{R}'} E_{\alpha_{k\vec{0}}\ l_{\cdot\cdot}} \tag{2.32}$$

and recalling that now the energy is referred to the whole system of particles. The symmetry for the matrix elements that was valid for a single cell now is not respected except in $\boldsymbol{K}$=0 or $\boldsymbol{K}$=$\boldsymbol{G}$/2:

$$\begin{aligned} \sum_{\boldsymbol{R}'} e^{i\boldsymbol{K}\cdot\boldsymbol{R}'} E_{\alpha_{k0}\beta_{l_R}} &= \sum_{\boldsymbol{R}'} e^{i\boldsymbol{K}\cdot\boldsymbol{R}'} E_{\beta_{l_R}\alpha_{k0}} = \sum_{\boldsymbol{R}'} e^{i\boldsymbol{K}\cdot\boldsymbol{R}'} E_{\beta_{l0}\alpha_{k-_R}} = \sum_{\boldsymbol{R}''} e^{-i\boldsymbol{K}\cdot\boldsymbol{R}''} E_{\beta_{l0}\alpha_{k_R}} \\ &\neq \sum_{\boldsymbol{R}'} e^{i\boldsymbol{K}\cdot\boldsymbol{R}'} E_{\beta_{l0}\alpha_{k_R}}, \qquad \boldsymbol{K}\neq 0, \boldsymbol{K}\neq\frac{\boldsymbol{G}}{2} \end{aligned} \tag{2.33}$$

where $\boldsymbol{R}$''= - $\boldsymbol{R}$'.

Eq.(2.31) is again an eigenvalue problem like for the case of isolated element and can be solved as a complex generalized Hermitian eigenvalue problem.

2.3.2 Calculation of energy derivatives

The primitive cell has at the centre a single dot that occupies only a part of it. The interdot exchange coupling is zero. Because of the latest considerations and due to the fact that derivatives of Zeeman, exchange, anisotropy, energy density are referred only to the cell of the first variable (α_{k0}) or at most to the nearest-neighbour, all terms of the sum in Eq.(2.31) with $\boldsymbol{R'\neq 0}$ are zero. Hence, for these energy density terms the equations are the same as those of the single particle case and the same occurs for their corresponding derivatives appearing the equations of motion. The only energy density term that differs from

the one obtained for the isolated element is the demagnetizing energy density. For a system of interacting nanoelements, the demagnetizing energy density is:

$$E_{\text{dem}} = \frac{1}{2} \sum_{\boldsymbol{R},\boldsymbol{R'},k,k'} \boldsymbol{m}_k(\boldsymbol{R}) \overleftrightarrow{N}(\boldsymbol{R},\boldsymbol{R'},k,k') \boldsymbol{m}_{k'}(\boldsymbol{R'}) \tag{2.34}$$

where, in addition to the sum over the k and k' micromagnetic cells belonging to the primitive cell, one must take into account also the sum (labeled generically by $\boldsymbol{R}$ and $\boldsymbol{R'}$) over the primitive cells. In order to calculate the first derivative, two properties of the demagnetizing tensor have been considered:

$$\langle v|N|\omega\rangle = \langle \omega|N^{+}|v\rangle^{*} = \langle \omega|N^{+}|v\rangle = \langle \omega|N^{t}|v\rangle = \langle \omega|N|v\rangle \tag{2.35}$$

where v and w are two vectors. Since N is real and symmetric and

$$\overleftrightarrow{N}(\boldsymbol{R},\boldsymbol{R'},k,k') = \overleftrightarrow{N}(\boldsymbol{R}-\boldsymbol{R'}+\boldsymbol{r}_{k'}-\boldsymbol{r}_k) = \overleftrightarrow{N}(-\boldsymbol{R}+\boldsymbol{R'}-\boldsymbol{r}_{k'}+\boldsymbol{r}_k) = \overleftrightarrow{N}(\boldsymbol{R'},\boldsymbol{R},k',k) \tag{2.36}$$

thanks to the inversion symmetry. Hence, the first derivative of the energy density is:

$$\begin{aligned}
\frac{\partial E_{dem}}{\partial \alpha_k(0)} = \frac{M_S^2}{2} \Bigg[& \sum_{\substack{\boldsymbol{R'}k' \\ (\boldsymbol{R'},k')\neq(0,k)}} \boldsymbol{m}_{k'}(\boldsymbol{R'}) \cdot \overleftrightarrow{N}(\boldsymbol{R'},0,k',k) \frac{\partial \boldsymbol{m}_k(0)}{\partial \alpha_k(0)} + \\
& + \sum_{\substack{\boldsymbol{R'}k' \\ (\boldsymbol{R'},k')\neq(0,k)}} \frac{\partial \boldsymbol{m}_k(0)}{\partial \alpha_k(0)} \cdot \overleftrightarrow{N}(0,\boldsymbol{R'},k,k') \boldsymbol{m}_{k'}(\boldsymbol{R'}) + \frac{}{\partial \alpha_k(0)} \left(\boldsymbol{m}_k(0) \cdot \overleftrightarrow{N}(0,0,k,k') \boldsymbol{m}_k(0) \right) \Bigg] = \\
= M_S^2 \Bigg[& \sum_{\substack{\boldsymbol{R'}k' \\ (\boldsymbol{R'},k')\neq(0,k)}} \boldsymbol{m}_{k'}(\boldsymbol{R'}) \cdot \overleftrightarrow{N}(\boldsymbol{R'},0,k',k) \frac{\boldsymbol{m}}{\partial \alpha_k(0)} + \boldsymbol{m}_k(0) \cdot \overleftrightarrow{N}(0,0,k,k') \frac{\partial \boldsymbol{m}_k(0)}{\partial \alpha_k(0)} \Bigg].
\end{aligned} \tag{2.37}$$

The second derivative is:

$$\frac{\partial^2 E_{dem}}{\partial \alpha_k(0) \partial \beta_l(\boldsymbol{R})} = \begin{cases} M_S^2 \Bigg[\sum_{\boldsymbol{R'}k'} \boldsymbol{m}_{k'}(\boldsymbol{R'}) \cdot \overleftrightarrow{N}(\boldsymbol{R'},0,k',k) \frac{\partial^2 \boldsymbol{m}_k(0)}{\partial \alpha_k(0) \partial \beta_k(0)} + \\ + \frac{\partial \boldsymbol{m}_k(0)}{\partial \beta_k(0)} \cdot \overleftrightarrow{N}(0,0,k,k) \frac{\partial \boldsymbol{m}_k(0)}{\partial \alpha_k(0)} \Bigg] & \boldsymbol{R}=0,\ l=k \\ M_S^2 \frac{\partial \boldsymbol{m}_l(0)}{\partial \beta_l(0)} \cdot \overleftrightarrow{N}(\boldsymbol{R},0,l,k) \frac{\partial \boldsymbol{m}_k(0)}{\partial \alpha_k(0)} & (\boldsymbol{R},l) \neq (0,k). \end{cases} \tag{2.38}$$

In the sum it is included the case in which $(\boldsymbol{R}', k') = (0, k)$ that is generated from the derivative of the second term in Eq.(2.37). Now it is possible to calculate the terms that enter into system of Eq.(2.31), starting with the one corresponding to $l = k$:

$$\begin{aligned}
&\sum_{\boldsymbol{R}} e^{i\boldsymbol{K}\cdot\boldsymbol{R}} E_{\alpha_{k0}\beta_{lR}} = \sum_{\boldsymbol{R}} e^{i\boldsymbol{K}\cdot\boldsymbol{R}} E_{\alpha_{k0}\beta_{kR}} = \\
&= M_S^2 \left[\sum_{\boldsymbol{R}'k'} \boldsymbol{m}_{k'}(0) \cdot \overleftrightarrow{N}(\boldsymbol{R}, \upsilon, \kappa, \kappa) \frac{\boldsymbol{m}}{\partial\alpha_k(0)\partial\beta_k(0)} + \frac{\boldsymbol{m}}{\partial\beta_k(0)} \cdot \overleftrightarrow{N}(0, \upsilon, \kappa, \kappa) \frac{\boldsymbol{m}_k(0)}{\partial\alpha_k(0)} \right] + \\
&+ \sum_{\boldsymbol{R}\neq 0} e^{i\boldsymbol{K}\cdot\boldsymbol{R}} M_S^2 \frac{\partial \boldsymbol{m}_k(0)}{\partial\beta_k(0)} \cdot \overleftrightarrow{N}(\boldsymbol{R}, \upsilon, k, k) \frac{\partial \boldsymbol{m}_k(0)}{\partial\alpha_k(0)} = \\
&= M_S^2 \sum_{\boldsymbol{R}} \left[\sum_{k'} \boldsymbol{m}_{k'}(0) \cdot \overleftrightarrow{N}(\boldsymbol{R}, \upsilon, \kappa, \kappa) \frac{\boldsymbol{m}}{\partial\alpha_k(0)\partial\beta_k(0)} + e^{\boldsymbol{K}\boldsymbol{R}} \frac{\boldsymbol{m}}{\partial\beta_k(0)} \cdot \overleftrightarrow{N}(\boldsymbol{R}, \upsilon, \kappa, \kappa) \frac{\boldsymbol{m}_k(0)}{\partial\alpha_k(0)} \right]
\end{aligned} \quad . \tag{2.39}$$

When $l \neq k$ the term turns out to be:

$$\sum_{\boldsymbol{R}} e^{i\boldsymbol{K}\cdot\boldsymbol{R}} E_{\alpha_{k0}\beta_{lR}} = M_S^2 \left[\sum_{\boldsymbol{R}} e^{i\boldsymbol{K}\cdot\boldsymbol{R}} \frac{\partial \boldsymbol{m}_l(0)}{\partial\beta_l(0)} \cdot \overleftrightarrow{N}(\boldsymbol{R}, \upsilon, l, k) \frac{\partial \boldsymbol{m}_k(0)}{\partial\alpha_k(0)} \right]. \tag{2.40}$$

Due to the properties of the demagnetizing tensor the symmetry

$$\sum_{\boldsymbol{R}'} e^{i\boldsymbol{K}\cdot\boldsymbol{R}'} E_{\alpha_{k0}\beta_{lR}'} = \sum_{\boldsymbol{R}'} e^{i\boldsymbol{K}\cdot\boldsymbol{R}'} E_{\alpha_{l0}\beta_{kR}'} \tag{2.41}$$

is fulfilled when $l = k$, but it is not fulfilled when $l \neq k$.

The formalism previously developed can be extended to a system of ADs. In this case it is necessary to add the exchange interaction between primitive cells [70]. In extended magnetic system like AD arrays in addition to the usual nearest-neighbours exchange interaction between micromagnetic cells, the exchange contribution across the nearest-neighbours micromagnetic cells belonging to adjacent surface primitive cells must be taken into account. Hence, the exchange energy density of the given primitive cell takes the form:

$$E_{exch} = A \sum_{k}^{N} \sum_{n}^{4} \frac{(1 - \boldsymbol{m}_k \cdot \boldsymbol{m}_n)}{l_c^2 kn} \tag{2.42}$$

The first sum runs over all the micromagnetic cells of the primitive cell, the second sum runs over the nearest-neighbours of the *k*-th micromagnetic cell. The variable l_c is the distance between the centers of two

adjacent cells of index k and n respectively. When the k th micromagnetic cell is on one of the edges (vertices) of the given primitive cell, the interaction with one (two) micromagnetic cell(s) belonging to the correct nearest primitive cell must be added.

2.4 Dynamical matrix method for multicomponent periodic systems

The DMM with periodic boundary conditions (PBCs), developed for extended and periodic ferromagnetic systems composed by one material and described in the previous Sections, is generalized to systems composed by j different ferromagnetic materials with j = 1,2,3,…F[31]. As for the case of the single component ferrromagnetic system, the index k labels the micromagnetic cells with k = 1,2,… N where N is the total number of micromagnetic cells within the primitive cell. The number of micromagnetic cells assigned to the jth ferromagnetic material within the primitive cell is N_j such that $N_1 + N_2 + \ldots + N_F = N$. For each micromagnetic cell the reduced magnetization takes the form $\boldsymbol{m}_k = \mathbf{M}_k / M_{\mathrm{S}}(k)$ where $\mathbf{M}_k$ ($M_{\mathrm{S}}(k)$) is the magnetization (saturation magnetization) in the kth cell. Since the system understudy contains different magnetic materials, also the saturation magnetization depends on the jth ferromagnetic material through the index k. Hence, in a polar reference frame the reduced magnetization reads

$$\boldsymbol{m}_k = (\sin\theta_k \cos\phi_k, \sin\theta_k \sin\phi_k, \cos\theta_k) \tag{2.43}$$

where ϕ_k (θ_k) is the azimuthal (polar) angle of the magnetization (the time dependence is omitted). The total energy density $E = \dfrac{\tilde{E}}{V}$, with $\tilde{E}$ the energy and V the volume of the system, respectively, is a function of θ_k and ϕ_k, namely $E = E(\theta_k, \phi_k)$ with $\mathcal{H} = \tilde{E}$ being $\mathcal{H}$ the Hamiltonian in a conservative system[30].

While the expressions of E_{ext}, E_{dem} and E_{ani} are similar to the ones of the one-component system, the physics underlying in the exchange energy density term E_{exch} is different. Indeed, E_{exch} includes also the interaction between two micromagnetic cells belonging to two adjacent ferromagnetic materials. Using the first-neighbours model, the exchange energy density in the primitive cell takes the form[31]

$$E_{exch} = \sum_{k=1}^{N} \sum_{n \in \{\mathrm{n.n.}\}} A\,(k,n) \frac{1 - \boldsymbol{m}_k \cdot \boldsymbol{m}_n}{a_{kn}^2} \tag{2.44}$$

where A is the exchange stiffness constant depending on the ferromagnetic materials through the indexes k and n, respectively and the variable a_{kn} is the distance between the centers of two adjacent micromagnetic cells of indexes k and n, respectively. In the first sum on the second member of Eq. (2.44) k varies over all N micromagnetic cells, while the second sum depending on n ranges over the nearest neighbouring (n.n.) micromagnetic cells of the k th micromagnetic cell that can belong to a different ferromagnetic material. As

for the case of 2D AD lattices[71], when the *k*th micromagnetic cell is on one of the edges (vertices) of the proper primitive cell, the interaction with the micromagnetic cells belonging to the correct nearest supercell (primitive cell) must be taken into account. Like for the one-component systems, by substituting the energy density into the Hamilton equations[31] yields the 2*N* system of linear and homogeneous equations

$$\begin{cases} \dfrac{\partial}{\partial t}\delta\phi_k = -\dfrac{\gamma(k)}{M_{\mathrm{s}}(k)\sin\theta_k}\displaystyle\sum_{l=1}^{N}\left[E_{\theta_k\phi_l}\delta\phi_l + E_{\theta_k\theta_l}\delta\theta_l\right] \\ \dfrac{\partial}{\partial t}\delta\theta_k = \dfrac{\gamma(k)}{M_{\mathrm{s}}(k)\sin\theta_k}\displaystyle\sum_{l=1}^{N}\left[E_{\phi_k\phi_l}\delta\phi_l + E_{\phi_k\theta_l}\delta\theta_l\right], \end{cases} \tag{2.45}$$

where $\gamma(k)$ is the gyromagnetic ratio in the *k*th cell. Also the gyromagnetic ratio depends on the *j*th ferromagnetic material through the index *k*. In order to find the final form of the equations of motion it is necessary to introduce: 1) the time dependence of the small angular deviations from the equilibrium magnetization in the usual exponential form 2) the Bloch condition applied to the dynamic magnetization of a periodic system.

The dynamic magnetization in the *k*th cell may be represented in the form

$$\delta\boldsymbol{m}_k = M_{\mathrm{s}}(k)\left(-\sin\theta_k\sin\phi_k\delta\phi_k + \cos\theta_k\cos\phi_k\delta\theta_k, \sin\theta_k\cos\phi_k\delta\phi_k + \cos\theta_k\sin\phi_k\delta\theta_k, -\sin\theta_k\delta\theta_k\right) \tag{2.46}$$

where the dependence on the Bloch wave vector is implicit. Note that, like for the one-component systems in the form either of isolated or periodic magnetic elements, $\delta\boldsymbol{m}_k$ is a complex vector, because the small angular deviations $\delta\phi_k$ and $\delta\theta_k$ are, in general, complex. Due to the PBCs and the Bloch rule, the number of independent variables in the system is limited to the number *N* of micromagnetic cells in the primitive cell also for an infinite array.

By omitting the index $\mathbf{R}$ when it has value equal to $\mathbf{0}$, because of the Bloch condition, or when it is irrelevant and by taking into account that the Bloch rule can be applied to the dynamical variables for $\mathbf{R}' \neq \mathbf{0}$, the 2*N* system of linear and homogeneous equations can be rewritten in a form similar to the ones of the one- component periodic system[31], namely

$$\begin{cases} \displaystyle\sum_{l=1}^{N}\left(-\frac{\sum_{\mathbf{R}'} E_{\theta_k\phi_l\mathbf{R}'}\, e^{i\mathbf{K}\mathbf{R}'}}{\sin\theta_k}\right)\delta\phi_l + \sum_{l=1}^{N}\left(-\frac{\sum_{\mathbf{R}'} E_{\theta_k\theta_l\mathbf{R}'}\, e^{i\mathbf{K}\mathbf{R}'}}{\sin\theta_k}\right)\delta\theta_l - \tilde{\lambda} = 0 \\ \displaystyle\sum_{l=1}^{N}\left(\frac{\sum_{\mathbf{R}'} E_{\phi_k\phi_l\mathbf{R}'}\, e^{i\mathbf{K}\mathbf{R}'}}{\sin\theta_k}\right)\delta\phi_l + \sum_{l=1}^{N}\left(\frac{\sum_{\mathbf{R}'} E_{\phi_k\theta_l\mathbf{R}'}\, e^{i\mathbf{K}\mathbf{R}'}}{\sin\theta_k}\right)\delta\theta_l - \tilde{\lambda} = 0 \end{cases} \tag{2.47}$$

where $\tilde{\lambda}$ $\frac{\Gamma_s(k)}{\gamma(k)}\omega$ are the complex eigenvalues. The indexes k and l range over the total number N of micromagnetic cells inside the primitive cell which are assigned to F different ferromagnetic materials. Note that Eq. (2.47) represents an eigenvalue problem that can be written in the compact form $\mathrm{C}\mathbf{v} = \tilde{\lambda}$ where C is a complex and non-symmetric matrix containing the second derivatives of the energy density calculated at the equilibrium and $\mathbf{v} = [\delta\phi_1, \delta\theta_1, \delta\phi_2, \delta\theta_2, ..., \delta\phi_N, \delta\theta_N]^{\mathrm{T}}$ are the eigenvectors. For each solution of the eigenvalue problem, the collection of all $\delta \boldsymbol{m}_k$ given in Eq. (2.46) defines the mode profile. For computational reasons, as done for the one- component periodic ferromagnetic systems, it is convenient to recast the eigenvalue problem in the form of a complex generalized Hermitian one. In a compact form, like for the one-component systems[31]

$$A\,\mathbf{v} = \lambda\, B\,\mathbf{v}\,. \tag{2.48}$$

Because of the presence of different magnetic parameters (magnetization and gyromagnetic ratio) a different definition of the eigenvalue λ is given with respect to the one-component systems. It is convenient to define the real eigenvalues as $\lambda = \frac{1}{\omega}$ to make them independent of the ferromagnetic material. The new defined eigenvalues turn out to be inversely proportional to the angular frequency of the collective modes. The energy density terms entering in the Hessian matrix B express the second derivatives of the energy density calculated at equilibrium and is given by:

$$B = \begin{bmatrix} \sum_{\mathbf{R}'} E_{\phi_1\phi_1\mathbf{R}'} e^{i\mathbf{K}\mathbf{R}'} & \sum_{\mathbf{R}'} E_{\phi_1\theta_1\mathbf{R}'} e^{i\mathbf{K}\mathbf{R}'} & \dots & \dots & \sum_{\mathbf{R}'} E_{\phi_1\phi_N\mathbf{R}'} e^{i\mathbf{K}\mathbf{R}'} & \sum_{\mathbf{R}'} E_{\phi_1\theta_N\mathbf{R}'} e^{i\mathbf{K}\mathbf{R}'} \\ \sum_{\mathbf{R}'} E_{\theta_1\phi_1\mathbf{R}'} e^{i\mathbf{K}\mathbf{R}'} & \sum_{\mathbf{R}'} E_{\theta_1\theta_1\mathbf{R}'} e^{i\mathbf{K}\mathbf{R}'} & \dots & \dots & \sum_{\mathbf{R}'} E_{\theta_1\phi_N\mathbf{R}'} e^{i\mathbf{K}\mathbf{R}'} & \sum_{\mathbf{R}'} E_{\theta_1\theta_N\mathbf{R}'} e^{i\mathbf{K}\mathbf{R}'} \\ \dots & \dots & \dots & \dots & \dots & \dots \\ \dots & \dots & \dots & \dots & \dots & \dots \\ \sum_{\mathbf{R}'} E_{\phi_N\phi_1\mathbf{R}'} e^{i\mathbf{K}\mathbf{R}'} & \sum_{\mathbf{R}'} E_{\phi_N\theta_1\mathbf{R}'} e^{i\mathbf{K}\mathbf{R}'} & \dots & \dots & \sum_{\mathbf{R}'} E_{\phi_N\phi_N\mathbf{R}'} e^{i\mathbf{K}\mathbf{R}'} & \sum_{\mathbf{R}'} E_{\phi_N\theta_N\mathbf{R}'} e^{i\mathbf{K}\mathbf{R}'} \\ \sum_{\mathbf{R}'} E_{\theta_N\phi_1\mathbf{R}'} e^{i\mathbf{K}\mathbf{R}'} & \sum_{\mathbf{R}'} E_{\theta_N\theta_1\mathbf{R}'} e^{i\mathbf{K}\mathbf{R}'} & \dots & \dots & \sum_{\mathbf{R}'} E_{\theta_N\phi_N\mathbf{R}'} e^{i\mathbf{K}\mathbf{R}'} & \sum_{\mathbf{R}'} E_{\theta_N\theta_N\mathbf{R}'} e^{i\mathbf{K}\mathbf{R}'} \end{bmatrix} \tag{2.49}$$

where $\sum_{\mathbf{R}'} E_{\alpha_k\beta_l\mathbf{R}'} e^{i\mathbf{K}\mathbf{R}'} \neq \sum_{\mathbf{R}'} E_{\beta_l\alpha_k\mathbf{R}'} e^{i\mathbf{K}\mathbf{R}'}$ and $\alpha,\beta = \theta,\phi$ for $\mathbf{K} \neq \mathbf{0}$ and $\mathbf{K} \neq \frac{\mathbf{G}}{2}$ with $\mathbf{G}$ a primitive vector of the reciprocal lattice. Hence, like for the one-component periodic magnetic system, matrix B is not symmetric. In a compact form its matrix elements can be written as

$$\left.\begin{aligned}
\widehat{\nu}_{2k-1,2l-1} &= \sum_{\mathbf{R}'} E_{\phi_k \phi_{l\mathbf{R}'}} e^{i\mathbf{K}\,\mathbf{R}'} \\
\widehat{\nu}_{2k-1,2l} &= \sum_{\mathbf{R}'} E_{\phi_k \theta_{l\mathbf{R}'}} e^{i\mathbf{K}\,\mathbf{R}'} \\
\widehat{\nu}_{2k,2l-1} &= \sum_{\mathbf{R}'} E_{\theta_k \phi_{l\mathbf{R}'}} e^{i\mathbf{K}\,\mathbf{R}'} \\
\widehat{\nu}_{2k,2l} &= \sum_{\mathbf{R}'} E_{\theta_k \theta_{l\mathbf{R}'}} e^{i\mathbf{K}\,\mathbf{R}'}
\end{aligned}\right\} k = 1,....,N, \quad l = 1,...,N \ . \tag{2.50}$$

While the matrix A takes the form

$$A = \begin{bmatrix}
0 & i\frac{M_s(1)}{\gamma(1)}\sin\theta_1 & 0 & 0 & \dots & \dots & \dots & 0 & 0 \\
-i\frac{M_s(1)}{\gamma(1)}\sin\theta_1 & 0 & 0 & 0 & \dots & \dots & \dots & 0 & 0 \\
0 & 0 & 0 & i\frac{M_s(2)}{\gamma(2)}\sin\theta_2 & \dots & \dots & \dots & 0 & 0 \\
0 & 0 & -i\frac{M_s(2)}{\gamma(2)}\sin\theta_2 & 0 & \dots & \dots & \dots & 0 & 0 \\
\dots & \dots & \dots & \dots & \dots & \dots & \dots & 0 & 0 \\
\dots & \dots & \dots & \dots & \dots & \dots & \dots & 0 & 0 \\
\dots & \dots & \dots & \dots & \dots & \dots & \dots & 0 & 0 \\
0 & 0 & 0 & 0 & 0 & 0 & 0 & 0 & i\frac{M_s(k)}{\gamma(k)}\sin\theta_N \\
0 & 0 & 0 & 0 & 0 & 0 & 0 & -i\frac{M_s(k)}{\gamma(k)}\sin\theta_N & 0
\end{bmatrix} \tag{2.51}$$

Matrix A depends on saturation magnetizations $M_s(k)$ and on the corresponding gyromagnetic ratios $\gamma(k)$. It may be decomposed into F submatrices $2N_1 \times 2N_1$, $2N_2 \times 2N_2$, …$2N_F \times 2N_F$ fulfilling the condition $N_1 + N_2 + \ldots + N_F = N$. Moreover, it is Hermitian like for the one-component ferromagnetic periodic systems.

2.5 Scattering cross-section

It is useful to give the expression of the differential scattering cross section used to interpret the micromagnetic results obtained in Chapter 3, 4 and 5. The evaluation of the differential cross section allows to assign unambiguously to a given spin-wave mode a given BLS peak. The differential scattering cross section associated to each magnonic mode[68] of the spectrum turns out to be proportional to the square

modulus of the amplitude of the scattered field, viz. $\tilde{\boldsymbol{E}}$, and takes thus the form

$$\left(\frac{d^2\sigma}{d\Omega\, d\omega}\right)_{p\to s} = CN\left(\left|\omega'-\omega\right|\right)\frac{\left|\left(\sum_{\boldsymbol{R}=\boldsymbol{R}_1}^{\boldsymbol{R}_N} e^{i(\Delta\boldsymbol{k}+\boldsymbol{q})\cdot\boldsymbol{R}}\right)\int_{\text{cell}} e^{i\Delta\boldsymbol{k}\cdot\boldsymbol{r}} A(\boldsymbol{r})\, d\boldsymbol{r}\right|^2}{\left|\tilde{\boldsymbol{E}}_{\text{i}}\right|^2}\delta\left(\Omega-\left|\omega'-\omega\right|\right), \tag{2.52}$$

where σ is the scattering cross section, $d\Omega$ is the differential solid angle and the subscripts *p* and *s* refer to the *p*- and *s*-polarization of the incident and scattered light, respectively. *C* is a constant depending on geometric and optical parameters, $N\left(\left|\omega'-\omega\right|\right)$ is the Bose-Einstein thermal factor with ω' and ω the angular frequency of the scattered and incident light, respectively, the sum $\sum_{\boldsymbol{R}=\boldsymbol{R}_1}^{\boldsymbol{R}_N} e^{i(\Delta\boldsymbol{k}+\boldsymbol{q})\cdot\boldsymbol{R}}$ is performed over *N* illuminated cells, $\tilde{\boldsymbol{i}}$ is the amplitude of the incident electric field, $\Delta k_\alpha = k_\alpha - k'_\alpha$, $\delta\left(\Omega-\left|\omega'-\omega\right|\right)$ is the Dirac delta and Ω is the angular frequency of the given collective mode. Here k'_α $\left(k_\alpha\right)$ is the α – component ($\alpha = x, y$) of the scattered (incident) wave vector projected on the surface and $A(\boldsymbol{r})$ is a quantity depending on the dynamical magnetization and optical properties of the media. In the numerical calculations, the differential scattering cross section associated to each collective mode at a given frequency and for a given Bloch wave vector is determined, because it is assumed in Eq.(2.52) the selection rule $\Delta\boldsymbol{k} = -\boldsymbol{q}$, which holds rigorously only when the area illuminated by light is infinite.

Chapter 3
Mono-material 2D magnonic crystals

Two-dimensional (2D) mono-material MCs can be realized in the form of a periodic array of interacting nanomagnets (dots)[53,54] or holes in a ferromagnetic film (i.e., AD array)[70]. In this respect, propagation of SWs in AD lattices, consisting of 2D periodic arrays of nanopatterned holes etched into a continuous ferromagnetic film, has been extensively investigated in the last years because of the possibility to control SW propagation on the nanoscale[71,72]. On the other hand great attentions has been devoted to the study of soft and Goldstone modes in condensed matter physics. Thanks to a detailed investigation, both experimental and theoretical, the softening of phonon modes was observed and proved by theoretical calculations in superconductors[73,74,75]. In magnetic nanostructures a lot of investigations concern the analysis of soft and pseudo-Goldstone modes as a function of the external magnetic field have been performed. Soft modes of acoustical nature and pseudo-Goldstone modes have been found, respectively, in antiferromagnetically in-plane magnetized Fe/Cr multilayers and trilayers[76,77]. The frequency of these modes, in both cases, vanishes at a critical magnetic field. In recent years, the investigation is focused on the softening mechanism in confined magnetic systems. As an example, the mode softening has been studied in the case of isolated elliptical dots showing that the frequency of the end mode vanishes for a particular value of the external magnetic field corresponding to the magnetization reversal[78]. Recently, the static and dynamic properties of ferromagnetic2D AD lattices as prototypes of MCs have been deeply investigated[79,80,81]. An investigation of the frequency dependence on **H** for AD lattices with different hole size was carried out by using the FerroMagnetic Resonance technique and by describing the field dependence of the most relevant modes with the Kittel equation[81]. In the range of magnetic fields explored, neither end-modes (EMs), i.e. modes localized close to the border of holes, nor softening of the resonance modes was found with FMR, while these modes

were observed by means of BLS technique[81]. Interestingly, 2D mono-material MCs show also interesting properties in the SWs manipulation and propagation. Recently some combined theoretical and experimental studies analyze the SW propagation in in-plane and in out-of-plane magnetized ADs[82]. However, there are not studied that shows the dependence of the static and dynamic properties on the ground-state magnetization.

Hence, this Chapter focuses on the study of the static and dynamic magnetic properties of 2D mono-material MCs. Principally, two different analysis have been performed. In the Section 3.1 is proved the existence of soft modes in 2D AD lattices, that is the softening of the EM and of the Fundamental (F) mode (the quasi-uniform mode of the spectrum) frequencies, both characterized by the presence of finite frequency gaps. This phenomena is totally confirmed by the experimental measurements obtained by means of the BLS technique performed at the Department of Physics and Geology of the University of Perugia. The underlying physics at the basis of the softening mechanism is explained by means of a simple phenomenological model that describes the occurring reorientational and continuous phase transition. The effect of the demagnetizing field on the frequency behaviour of the most relevant collective modes is also discussed.

Moreover in section 3.2, the effect of the ground-state magnetization on the SWs frequencies in the ADs system has been studied by means of the DMM. Moreover the group velocity and the band width of the most relevant modes have been evaluated for both the static magnetization distributions.

3.1 Soft magnonic modes in 2D antidot lattices

3.1.1 Antidot lattices

A systematic investigation of the dependence of the magnetic normal modes on the magnetic field **H** for four arrays of AD lattices has been carried out. The samples have been fabricated by the Professor Adeyeye at the National University of Singapore. The geometric parameters of the four samples are the following: the lattice constant (a = 420 nm) and the thickness (L = 30 nm) are fixed while the circular holes have different diameter d_i (separation s_i) with i =1,2,3,4: d_1 = 140 nm (s_1 = 280 nm), d_2 = 180 nm (s_2 = 240 nm), d_3 = 220 nm (s_3 = 200 nm) and d_4 = 260 nm (s_4 = 160 nm). In Fig. 3.1 are shown the SEM images provided by the Professor Adeyeye at the National University of Singapore of the four systems investigated.

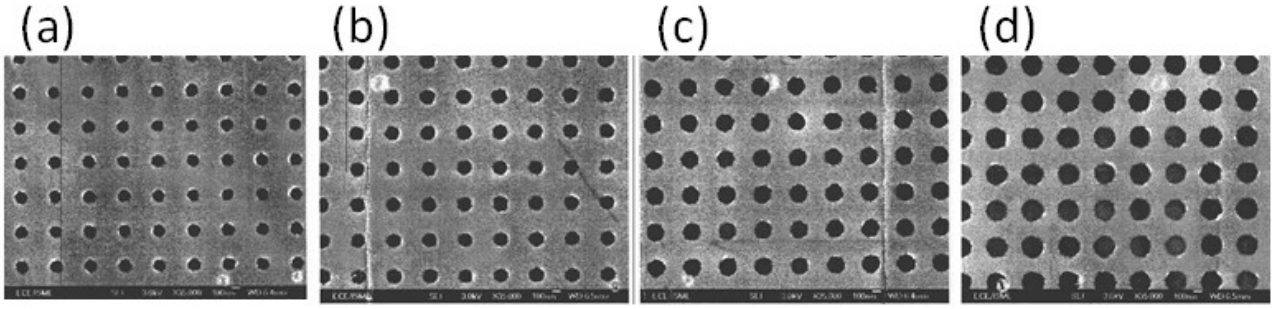

Fig. 3.1. SEM images of the four samples studied provided by Professor Adeyeye, National University of Singapore. (a) sample with d_1 = 140 nm, (b) d_2 = 180 nm, (c) d_3 = 220 and (d) d_4 = 260 nm.

The ground-state magnetization is calculated by means of the OOMMF code with periodic boundary conditions[49] by subdividing the system into micromagnetic cells of 5 nm × 5 nm × 30 nm. Thanks to the DMM with implemented 2D boundary conditions, the spectrum of magnetic normal modes has been calculated. The parameters used in the simulations have been obtained by fitting the dispersion curve of the DE mode in the corresponding continuous Permalloy (Py) ($Ni_{80}Fe_{20}$) film in the dipolar-exchange regime for a fixed value of K = 0 according to Eq. (3.1)

$$\nu^{\mathrm{DE}} = \frac{\gamma}{2\pi}\left[\left(H + \frac{2A}{M_{\mathrm{S}}}K^2\right)\left(H + \frac{2A}{M_{\mathrm{S}}}K^2 + 4\pi M_{\mathrm{S}}\right) + \left(2\pi M_{\mathrm{S}}\right)^2\left(1\text{-}e^{-2KL}\right)\right]^{\frac{1}{2}} \tag{3.1}$$

where L indicates the thickness of the sample and H is the external magnetic field that ranges from 0 to 2000 Oe. The magnetic parameters obtained are: $\gamma/2\pi$ = 2.8 GHz/kOe with γ the gyromagnetic ratio, saturation magnetization M_s = 800 emu/cm^3 and exchange stiffness constant $A = 1.3 \times 10^{-6}$ erg/cm.

3.1.2 Collective mode classification

The collective excitations has been classified by taking into account their spatial profiles calculated by means of the DMM calculations. In Fig. 3.2 are shown the spatial profiles of the most relevant modes for the system with d = 260 nm and for an external field of H = 2 kOe, but the collective mode classification is valid also for the AD lattices with holes of different diameter[70]. Starting from lower frequency part of the magnonic spectrum it is present the edge mode (EM), that is a SW mode strongly localized at the border of the ADs in the direction of **H** and along the local static magnetization **M** (it is important to remember that EM indicates in case of analysis of antidot array the edge mode while in the next chapter EM will indicates the end mode). The fundamental (F) mode has frequency higher than the EM and it is the quasi-uniform resonance modes of the spectrum. The F mode spreads in the horizontal channel comprised between ADs. The fundamental localized (F^{loc}) mode is similar to the F mode but it has maximum amplitude in the horizontal rows containing ADs. The F^{2loc} × 4BA mode exhibits two nodal planes perpendicular to the local static magnetization **M** along the horizontal rows of AD lattices, but, in addition, it has four nodal planes of

backward-like (BA) type along the horizontal channels (perpendicular to the local static magnetization **M**). This mode is mainly localized in the horizontal rows close to AD lattices and this kind of localization increases with decreasing *H*.

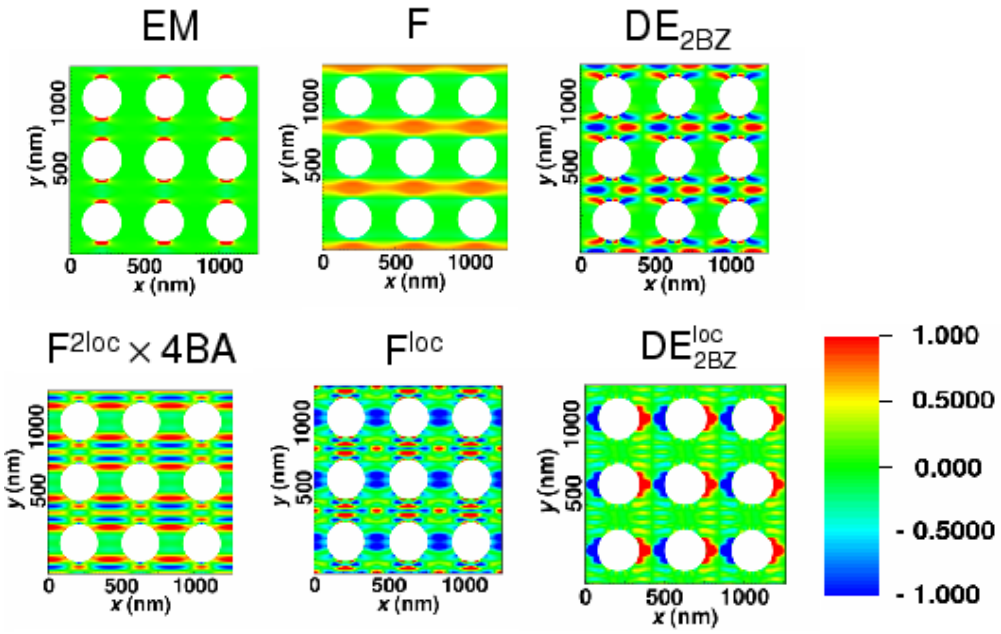

Fig. 3.2. Spatial profiles (real part of the out-of-plane component of the dynamic magnetization) in 3 × 3 primitive cells of the relevant modes are plotted for d = 260 nm and H = 2 kOe.

At high frequency it is present the Damon-Eshbach-like (DE) mode, named DE^{loc}_{2BZ} where 2BZ indicates that this mode has the largest calculated cross-section in the second BZ. Note that the calculated scattering cross-section of the DE^{loc}_{2BZ} mode is non-negligible up to **K** close to the centre of the 1BZ and vanishes exactly at **K = 0**. In addition, in the sample with d_4 = 260 nm, the DE_{2BZ} mode which is mainly concentrated in the horizontal channels and exhibits the same cross-section features as the DE^{loc}_{2BZ} has been studied. This is due to the fact that for this diameter the large demagnetizing field in the horizontal channels deforms the spatial profile of the detected DE_{2BZ} mode which becomes detectable at **K = 0**.

3.1.3 Softening of collective modes

The SWs frequencies obtained by means of the DMM as a function of **H** are reported in Fig. 3.3. The calculated frequencies are compared to the SWs frequencies measured experimentally by means of the BLS technique provided by the Department of Physics and Geology of the University of Perugia. As a general comment, by looking at Fig. 3.3, it is possible to note a very good agreement between the DMM calculations and the BLS measurements for all the diameters. The small discrepancies can be attributed to the fact that the periodic distribution of fabricated holes tends to become more irregular with increasing hole size. The

frequencies of the collective excitations have a common trend: they decrease by decreasing the intensity of **H**. It is also very interesting to note that for all the systems analyzed according to the DMM simulations, the softening of both the F mode and EM occur when **H** is reduced below a critical field $\mathbf{H}_c$. Furthermore, by inspection of the Fig. 3.3, one observes that $\mathbf{H}_c$ monotonically increases upon increasing the hole diameter. The calculated values of $\mathbf{H}_c$ for each diameter are: a) $\mathbf{H}_c$ (d_1) = 0.2 kOe b) $\mathbf{H}_c$ (d_2) = 0.32 kOe c) $\mathbf{H}_c$ (d_3)= 0.5 kOe and d) $\mathbf{H}_c$ (d_4)= 0.75 kOe. Moreover, at $\mathbf{H}_c$ the calculated frequency curves exhibit a finite gap whose value decreases by decreasing the hole diameter. These trends are confirmed by the BLS measurements, although in the experiments the softening is less pronounced. This discrepancy between theory and experiment may be ascribed to the size and shape distribution of the holes that could mask the observation of frequency softening for large diameters. For d_3 = 220 nm and d_4 = 260 nm the simulations predict a further minimum for the EM frequency below $\mathbf{H}_c$ due to a sudden jump of **M** towards the *x* direction. In Fig. 3.3 the BLS and calculated frequencies of the Damon-Eshbach mode of the unpatterned reference film are also shown as empty up triangles and dashed black lines, respectively.

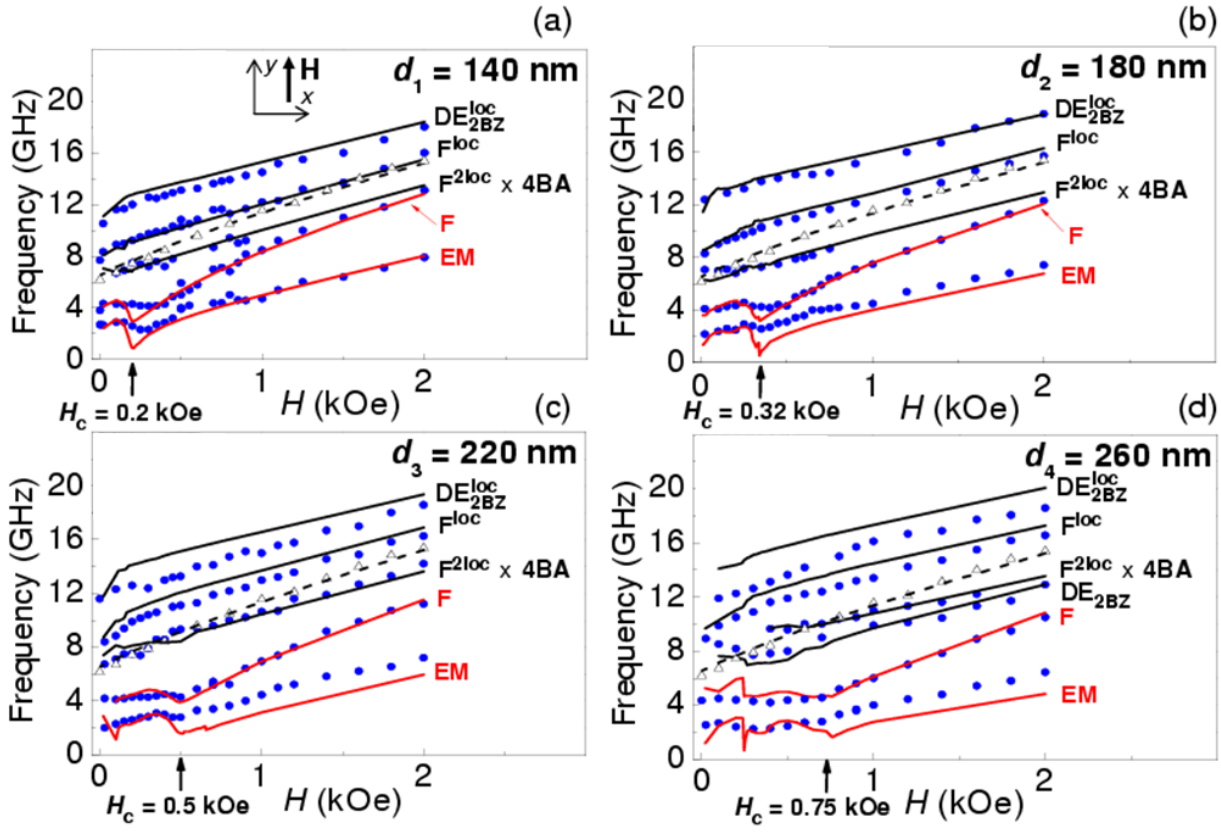

Fig. 3.3. Frequencies of spin-wave modes vs. *H* for (a) d_1 = 140 nm, (b) d_2 = 180 nm, (c) d_3= 220 nm, (d) d_4 = 260 nm. Solid red lines: calculated frequencies of EM and F mode. Solid black lines: calculated frequencies of the other relevant modes of the spectrum. Blue circles: BLS frequencies. Dashed black lines: calculated frequencies of the Damon-Eshbach mode of the continuous film. Empty up triangles: BLS frequencies of the Damon-Eshbach mode of the continuous film. The magnitude of the critical field H_c is shown and marked by an arrow for each diameter. In panel (a) a reference frame with the direction of **H** is shown.

It is important to note that in these AD lattices the softening does not involve only the lowest-frequency mode of the spectrum, that is the EM, but also the F mode[78]. This phenomena is in contrast with the mode softening and magnetization reversal in isolated nanorings where only the lowest-frequency mode softens[83]. In order to explain the softening mechanism of the EM and F mode it is necessary to observe the evolution of the mode localization as a function of the direction of **M**. The Fig. 3.4 shows the calculated ground-state magnetization distribution and the spatial profiles of the EM and F mode for $d_4 = 260$ nm and **H** = 1000 Oe. If the applied magnetic field is strong enough to saturate the system, the magnetization in every cell is almost parallel to **H**. In this case the EM is localized along the y direction close to the border of the ADs while the F mode spreads in the horizontal channels.

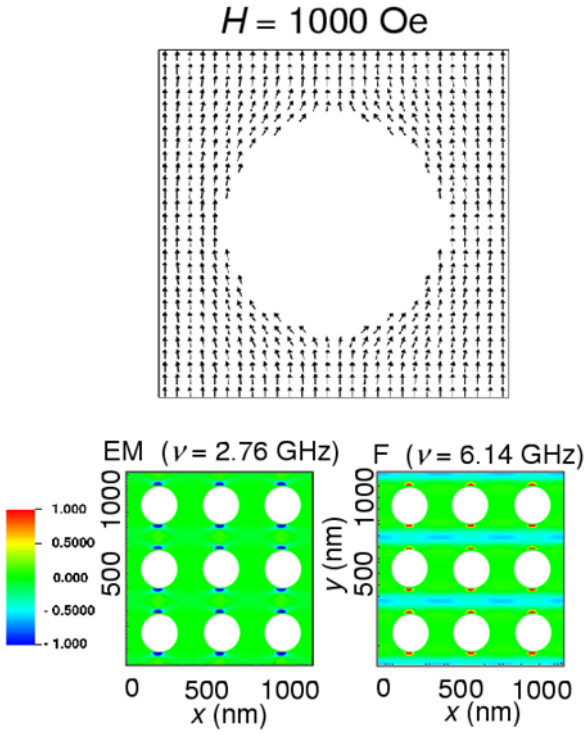

Fig. 3.4. Spatial profiles of the EM and of the F mode for $d_4 = 260$ nm in 3 × 3 primitive cells calculated at $H = 1000$ Oe ($H > H_c$) together with the ground-state magnetization distribution in the primitive cell.

If the applied magnetic field decreases in order that $H < H_c$ a continuous rotation of **M** from the hard axis, that is placed along the principal symmetry of the lattice (y direction), to the easy axis at $\phi = 45^o$ with ϕ denoting the in-plane angle formed by **M** with the y axis takes place (see Fig. 3.5). The continuous phase transition associated to the rotation of **M** corresponds to a lowering of the symmetry taking place with increasing H. This means that the phase where **M** is aligned along the y direction ($H > H_c$) is more ordered with respect to that where **M** forms an angle $\phi = 45^o$ with the y direction ($H < H_c$)[84,85]. By decreasing H, the spatial localization of the F mode and of the EM follows the rotation of **M** and, as a consequence, their amplitude is mainly concentrated along the diagonal of the primitive cell (see Fig. 3.5).

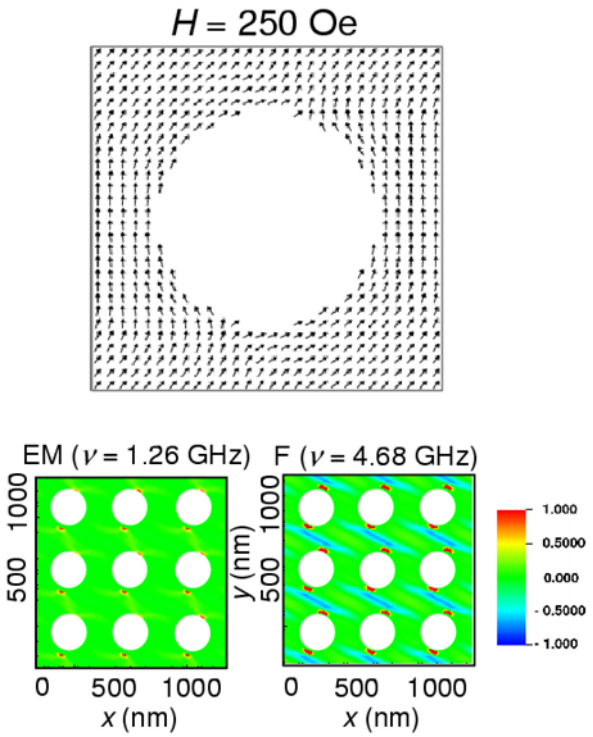

Fig. 3.5. Spatial profiles of the EM and of the F mode for d_4 = 260 nm in 3 × 3 primitive cells calculated at H = 250 Oe ($H < H_c$) together with the ground-state magnetization distribution in the primitive cell.

For $H < H_c$ the rate of decrease of the mean demagnetizing field is lower with respect to that of H resulting in an increase of the mean internal field $< H_{int} > = H + < H_{dem} >$ with $< H_{dem} >$ the y-component of the demagnetizing field averaged both over the y direction and over the x direction inside the primitive cell. Unlike the case of the surface mode in perpendicularly magnetized iron and cobalt (Co) films[78,86], the calculated finite frequency gaps of the F mode and of the EM are only due to the internal field contribution. This contribution is directly related to the strong localization, around H_c, of both modes close to the border of holes where the y-component of the demagnetizing field changes sign.

3.1.4 Demagnetizing fields of the most relevant collective modes

It is very interesting to investigate the frequency behaviour of the F and F^{loc} modes, which are the most relevant modes of the spectrum as a function of the geometric parameters of the samples. Since the frequencies of the SWs excitations are related to the internal magnetic field experienced by the SWs modes, it is useful to discuss the features of the mean demagnetizing field. Due to the surface magnetic charge distribution at the border of the ADs, $\mathbf{H}_{dem}$ is parallel to **H** in the horizontal rows and antiparallel to **H** in the horizontal channels . As a consequence, the F mode, that is mainly localized in the horizontal channels, experiences a negative mean demagnetizing field, whereas the F^{loc} mode, that is mainly concentrated in the horizontal rows, feels a positive mean demagnetizing field. The Fig. 3.6 shows the F and F^{loc} frequencies calculated at H = 2.0 kOe as a function of the aspect ratio $\eta = L/s$ and compare them to the experimental

frequency values. It is important to note that in the micromagnetic calculation of the mean demagnetizing field the average along the *y* direction for the F and F^{loc} modes is done considering the micromagnetic cells corresponding to the mode localization. The aspect ratio η for the F mode is calculated by taking into account the mode localization along the *y* direction in the horizontal channels that is less than the separation between holes.

By looking at the Fig. 3.6 it is possible to observe that the F mode frequencies decrease with increasing the aspect ratio, while the F^{loc} mode frequency has an opposite trend. Indeed, on increasing the diameter of the holes, the separation between holes reduces and, as a results, the mean demagnetizing field (*y* component) increases negatively leading to a decrease of the F mode frequencies. Instead, by increasing the hole diameter, increase also the mean demagnetizing field experienced by the F^{loc} mode yielding to a gain of the corresponding frequencies. In Fig. 3.6(b) is shown the trend of the mean demagnetizing field calculated by OOMMF with PBCs at $H = 2$ kOe experienced by the F and F^{loc} mode as a function of η.

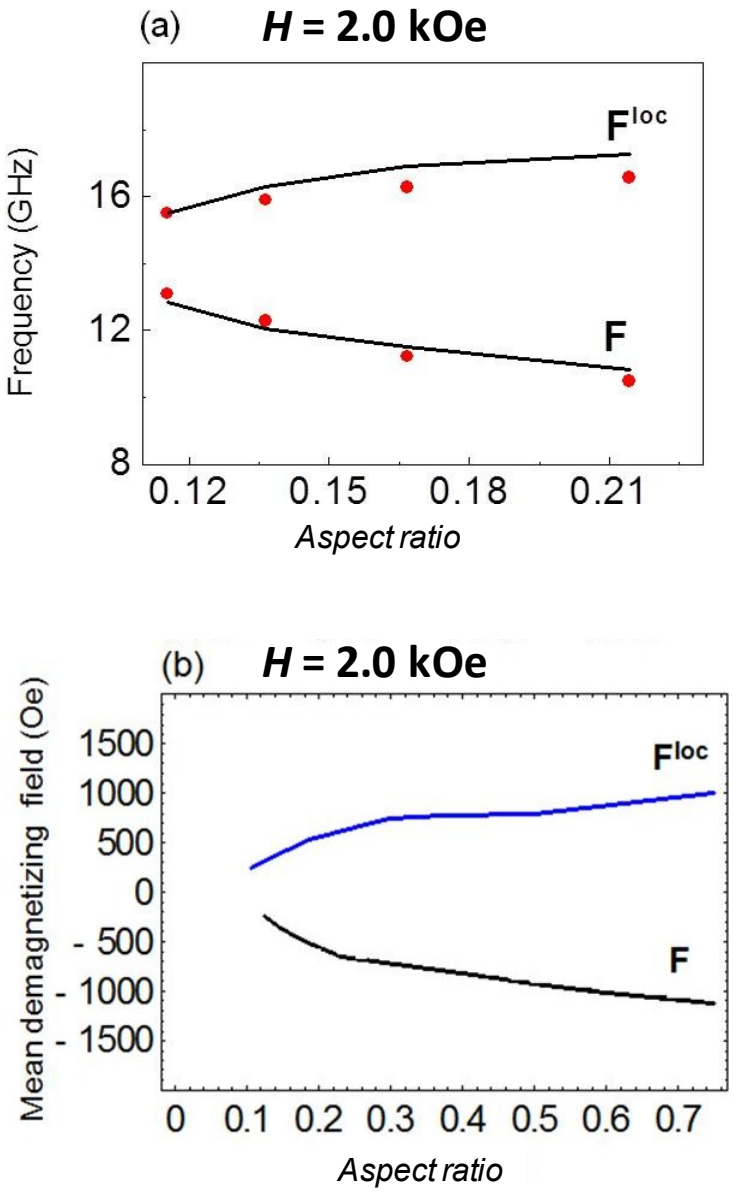

Fig. 3.6. (a) Measured (red points) and calculated (black lines) frequency behaviour vs. the aspect ratio for the F and F^{loc} modes, at H = 2.0 kOe. (b) Continuous black line: calculated mean demagnetizing field (y-component) vs. the aspect ratio for the F mode. Continuous blue line: calculated mean demagnetizing field (y-component) vs. the aspect ratio for the F^{loc} mode.

In order to completely understand the frequencies trend shown in Fig. 3.6, the mean demagnetizing field (y-component) averaged over the micromagnetic cells along the y-direction experienced by the F mode as a function of x has been calculated at H = 2.0 kOe. In Fig. 3.7(a) it is drawn in for two different diameters d = 140 nm and d = 180 nm, respectively, while in Fig. 3.7(b) it is plotted the corresponding one felt by the F^{loc} mode.

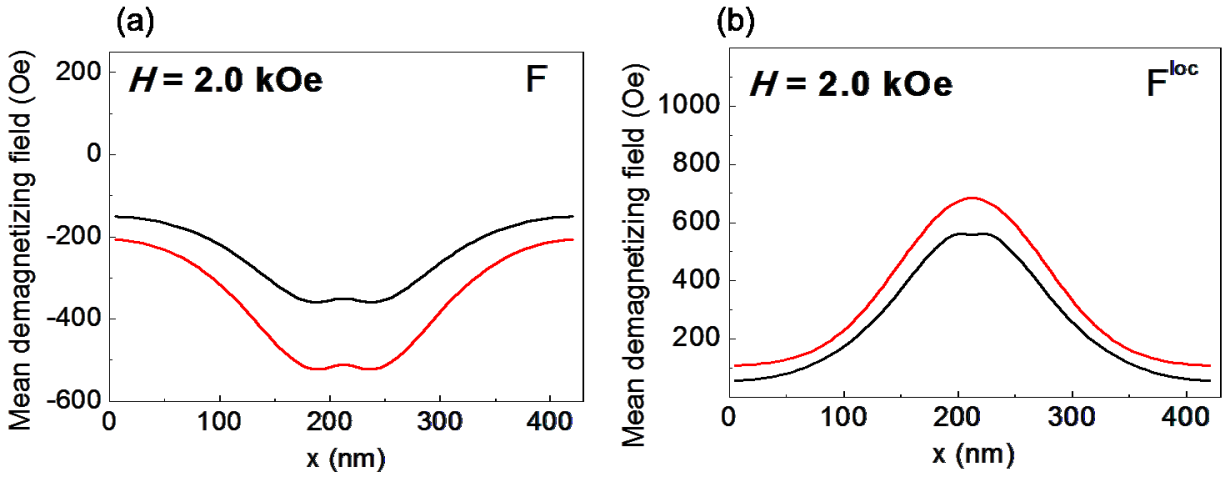

Fig. 3.7. (a) Continuous black (red) line: calculated mean demagnetizing field as a function of x for the F mode in the primitive cell at d_1= 140 nm (d_2= 180 nm). (b) As in panel (a), but for the F^{loc} mode.

3.2 Effect of the ground-state magnetization on the dynamic properties

3.2.1 System and method

The square ADs array is composed of circular nanoholes with diameter d = 200 nm, periodicity a = 610 nm embedded into a Cobalt-Iron-Borum (CoFeB) film having thickness of 41 nm[82]. The Fig. 3.8(a) shows the top of view of the ADs system including the primitive cell. The ground-state magnetization is calculated by means of the OOMMF code with PBCs[49] by subdividing the system into micromagnetic cells of 5 nm × 5 nm × 41 nm. Thanks to the DMM with implemented 2D boundary conditions, the spectrum of magnetic normal modes has been calculated for a fixed external magnetic field having an intensity of H = 20 kOe. In the simulations, the following magnetic parameters are used for CoFeB: $\gamma/2\pi$ = 2.8 GHz/kOe with γ the gyromagnetic ratio, saturation magnetization M_s = 1330 emu/cm^3 and exchange stiffness constant A = 2.75 × 10^{-6} erg/cm. The saturation magnetization is an effective magnetization because its value includes the perpendicular surface anisotropy typical of this ferromagnetic alloy. For the CoFeB material the value of the anisotropy constant is K = 3.7 erg/cm^2 .

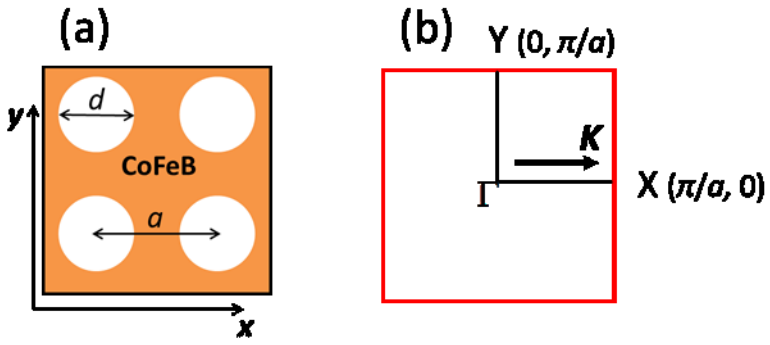

Fig. 3.8. (a) ADs square lattice with a the periodicity of the system and d the diameter of the ADs. (b) The 1BZ in the reciprocal space is draw and the x direction along which the SWs propagate is indicated.

The analysis of the SWs frequency is carried out along the x direction (see Fig. 3.8(b)) that is varying K_x and fixing K_y. K_x and K_y are the component of Bloch wave vector $\boldsymbol{K} = \left(\frac{2\pi}{a} n_x, \frac{2\pi}{a} n_y \right)$ with $K_x = \frac{2\pi}{a} n_x$ and $K_y = \frac{2\pi}{a} n_y$. Since the ADs system is periodic, with a periodicity a in direct lattice and periodicity K in reciprocal lattice, it is sufficient to calculate the frequency of SWs in the first BZ to obtain the frequency of SWs in all points in x direction of the reciprocal space.

3.2.2 Static and dynamic properties

The external magnetic field has been applied along two different directions: a) first **H** is parallel to the z-axis and secondly b) **H** is placed along the y direction. As a results, the ADs system is in the first case with an out-of-plane magnetization while in the second case in-plane magnetized. The Fig. 3.9 shows top of the views of the ground-state magnetization distributions in the primitive cell of the ADs system calculated by means of the OOMMF with PBCs. In the case of **H** placed parallel to the z direction, the static magnetization rotates in the out-of-plane direction and it is aligned with **H** (see Fig. 3.9(a)). Instead, when **H** is parallel to the y direction, it is possible to observe in Fig. 3.9(b) that the static magnetization is in-plane and along the y direction. By further inspection of the Fig. 3.9(a) and (b), a small bending of the static magnetization close to the ADs edges can be noted for both the ground states of the magnetization distributions due to the presence of the ADs.

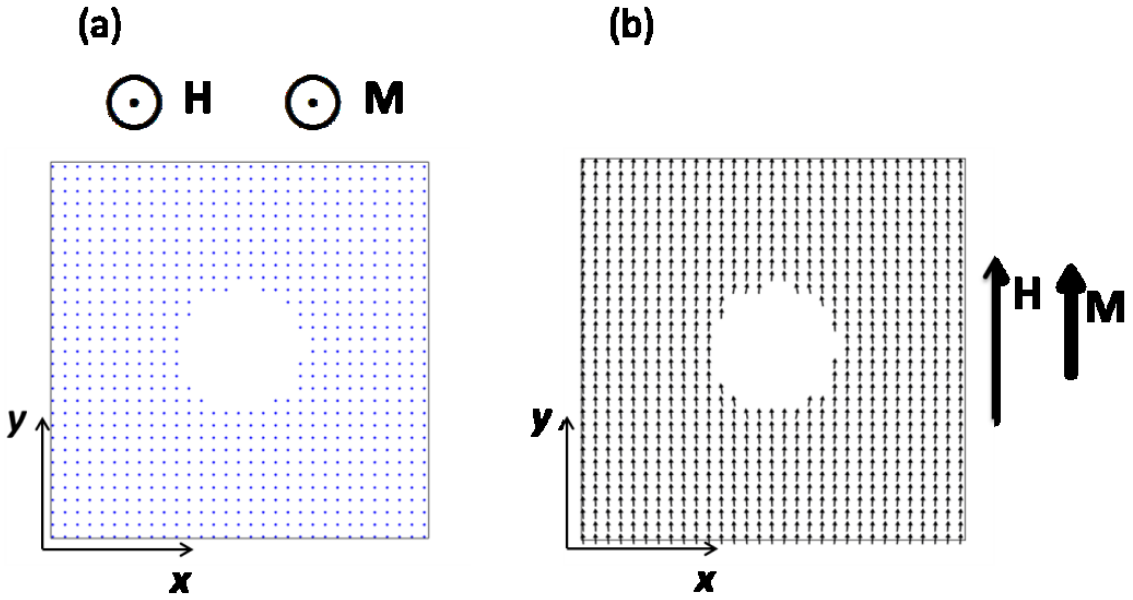

Fig. 3.9. (a) Top of the view of the distribution of the ground-state magnetization for the case of the out-of-plane external magnetic field in the primitive cell together with the **H** and **M** direction. (b) As in panel (a) but in the case of in-plane external field.

Starting from the two different distribution of the static magnetization, the dynamical properties of the ADs system have been calculated by means of the DMM. The analysis is focused on the SWs modes having an appreciable scattering cross section in the center of the BZ. When the **H** is applied along the *z* direction, it is present only one SW mode having relevant differential scattering cross-section. The characteristic mode of the out-of-plane magnetized ADs system is called relevant mode (RM) and it spreads in the whole primitive cell. The calculated spatial profile in the center of the BZ is shown in Fig. 3.10(a). While, in the case of the in-plane magnetization there are two SWs excitations with non-negligible scattering cross-section that are classified by taking into account their spatial localization in the primitive cell. The mode with lower frequency is the EM that is strongly localized at the edges of the holes and, at a higher frequency, the DE mode that spreads in the whole primitive cell and corresponds to the F mode in the center of the BZ. The spatial profiles of the EM and DE mode are shown in Fig. 3.10(b) and (c), respectively.

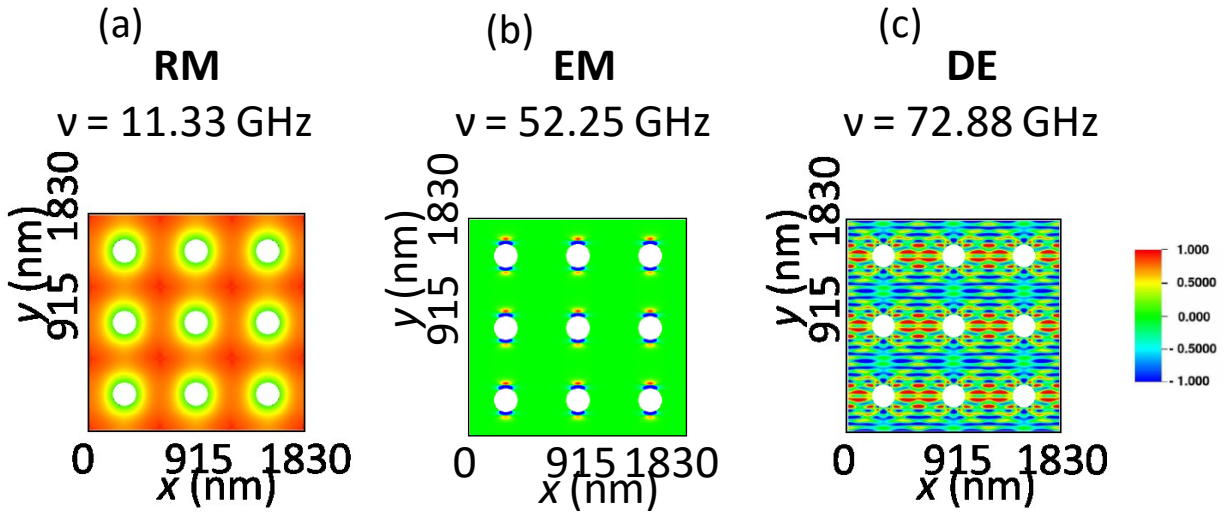

Fig. 3.10. (a) Calculated spatial profiles of the RM, real part of the *y* component of the dynamic magnetization, in 3 × 3 primitive cells for the out-of-plane magnetized AD lattice. (b) Spatial profile of the EM, real part of the out-of-plane component of the dynamic magnetization, in 3 × 3 primitive cells for the in-plane magnetized AD lattice. (c) As in panel (b), but for the DE mode.

In order to investigate the effect of the ground-state magnetization on the frequency of the SWs, the band structure for the collective excitations previously introduced are calculated at fixed external magnetic field H = 20 kOe for both the configuration according to the DMM. The dispersion curves are reported in Fig. 3.11(a) in the case of out-of-plane magnetization[83] and Fig. 3.11(b) in the case of in-plane magnetized ADs system.

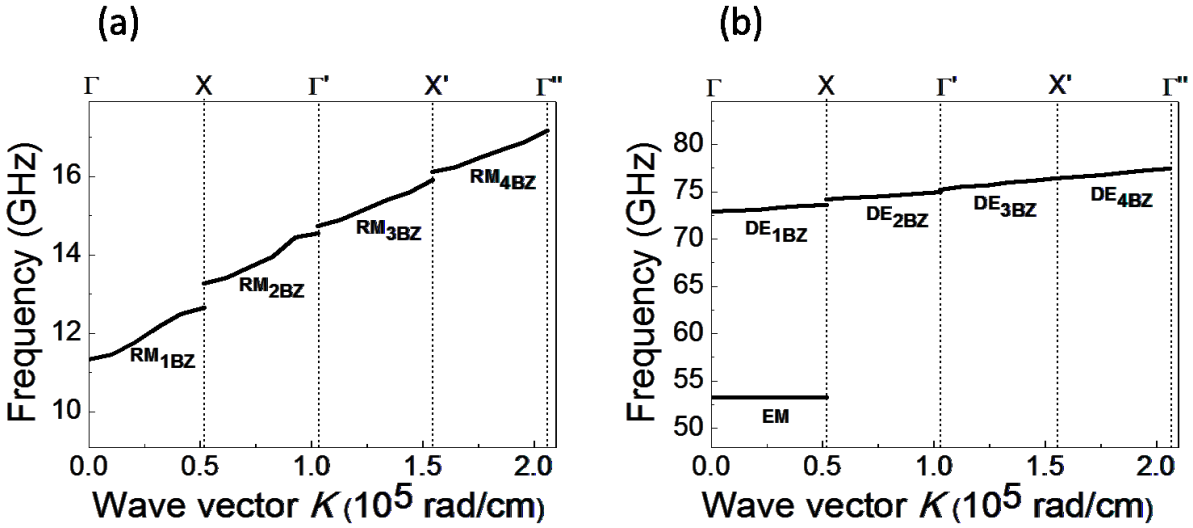

Fig. 3.11. Dispersion relation along the *x* direction perpendicular to the external magnetic field. (a) Dispersion curve of the RM in the case of **H** parallel to the *z*-axis. (b) Dispersion curves of the EM and DE mode in the case of **H** parallel to the *y*-axis.

As a general comment, it is possible to note that the frequencies of the RM in the out-of-plane magnetized system are lower than the frequencies of EM and DE mode in the in-plane magnetized one. This effect is related to the different internal magnetic field present in the two static configurations. The internal magnetic field ($\mathbf{H_{int}}$) can be decomposed in the sum of the demagnetizing field $\mathbf{H_{dem}}$ and the exchange field $\mathbf{H_{exch}}$, $\mathbf{H_{int}} = \mathbf{H_{dem}} + \mathbf{H_{exch}}$. While the $\mathbf{H_{exch}}$ minor influences $\mathbf{H_{int}}$, $\mathbf{H_{dem}}$ gives an important contribution to $\mathbf{H_{int}}$. In particular, by comparing the intensity of the internal magnetic field calculated for the case of in-plane magnetized system and in the case of out-of-plane magnetized system, it is possible to note that $\mathbf{H_{int}}$ is higher in the first case with respect to the latter. This can be attributed to the fact that the corresponding demagnetizing field that reduces the internal magnetic field is minor in the case of the out-of-plane magnetized system with respect to the one of the in-plane magnetized system. Moreover it is possible to observe the presence of band gaps at the border of each BZs for both the RM and DE mode. The formation of band gaps is due to the inhomogeneitiy of the $\mathbf{H_{int}}$ felt by the collective excitations. This explanation is valid for the in-plane and out-of-plane magnetized system, indeed due to the presence of the holes, the demagnetizing field influences the trend of the internal field when **M** is in-plane and also when **M** is out-of-plane.

By further inspection of Fig. 3.11, one observes that the band gaps amplitude decreases by increasing ***K*** for both the geometries analyzed. In particular, the values of the band gaps have been calculated as the frequencies difference of the RM and DE mode at the *n*BZ and (*n*+1)BZ (where *n* indicates the number of the BZ and *n* = 1,2,3,4.). Due to the frequency scale the band gaps of DE mode in Fig. 3.11(b) are not clearly visible, but their calculated values are collected in Tab. 3.1 together with the band gaps calculated for RM mode.

$\Delta\nu^{K}$ (GHz)	$RM_{n\mathrm{BZ}}$	$DE_{n\mathrm{BZ}}$
$\Delta\nu^{X}$ (GHz)	0.61	0.57
$\Delta\nu^{\Gamma}$ (GHz)	0.18	0.34
$\Delta\nu^{X'}$ (GHz)	0.21	0.07

Tab. 3.1. Frequency band gaps calculated for the most representative modes.

By looking at Tab. 3.1, it is possible to observe that the band gaps amplitude are almost similar for the RM and DE modes in the out-of-plane and in-plane magnetized system. This means that band gaps amplitude is not strictly related to the ground-state magnetization. Indeed, the amplitude of band gaps is always minor than 1 GHz and it decreases by increasing the Bloch wave vector. A different dependence from the static configuration is found for the bandwidth amplitude. In Tab. 3.2 are reported the bandwidths of the RM and DE mode calculated according to Eq. (3.2)

$$\Delta\nu = |\, \nu\,(K_x = n\pi/a) - \nu\,(K_x = (n-1)\pi/a)\,| \qquad (3.2)$$

where n indicates the number of the BZ and n = 1,2.

Band width (BW)	RM_{nBZ}	DE_{nBZ}
BW 1BZ (GHz)	1.33	0.72
BW 2BZ (GHz)	1.28	0.75

Tab. 3.2. Frequency bandwidths calculated for the most representative modes.

Tab. 3.2 shows that the band width of the RM is higher than the one of the DE mode both for the 1BZ and the 2BZ. This means that it is influenced by the distribution of the static magnetization. Therefore, the RM in the out-of-plane magnetized ADs system is more propagative than the DE mode in the in-plane magnetized system.

3.3 Conclusions

Summarizing, here the magnetic properties of different mono-material MCs have been studied. In particular, in Sect. 3.1, it has been shown that in 2D Py AD lattices with hole size in the nanometric range, the softening of the two lowest-frequency modes (EM and F mode) is the consequence of a continuous phase transition of the static magnetization which progressively rotates from the hard axis to the easy axis. It was also by means of micromagnetic simulations that frequencies of soft modes exhibit a finite gap at the critical field, because of internal field contributions related to their localization features. Moreover, the different trend of the frequencies at high external magnetic field of the most relevant collective modes, namely F and F^{loc} modes, as a function of the aspect ratio has been explained in terms of demagnetizing fields.

Finally, in Sect. 3.2 the effect of the ground-state magnetization on the spin dynamics has been investigated. Thanks to the micromagnetic simulations it has been demonstrated that the in the case of out-of-plane magnetization it is present only one relevant mode while in the case of in-plane magnetization there are two important different SWs excitations. The frequencies of the RM are higher with respect to those of the DE mode at a fixed external magnetic field. In addition the band gaps and the band widths of the RM and DE modes have been calculated. It can be seen that the values of the band gaps do not depend on the ground-state magnetization while the band widths are connected to the ground-state magnetization.

Chapter 4
Multi-material 2D magnonic crystals

Chapter 4 is devoted to the investigation of the static and dynamic magnetic properties in MCs composed of different ferromagnetic materials. In the following the term "bicomponent MCs" refers to a MCs composed of two different ferromagnetic materials. Several theoretical and experimental investigations have been carried out for characterizing collective modes and for determining the magnonic band structure in 1D and 2D MCs[87,88]. Among them, very recently, a 1D bicomponent MC consisting of arrays of nanostripes made by alternating Py and Co materials and exhibiting allowed minibands and frequency gaps was experimentally investigated[89]. Moreover, a micromagnetic study of magnonic band structures for exchange SWs propagating in 1D bicomponent MCs made by arrays of alternating Co and nickel stripes was carried out[90]. The recent works on 2D bicomponent ferromagnetic systems deal either with time-domain analysis of SW dynamics[91] or with modelling of dispersion and opening of band gaps at edges of Brillouin zones (*n*BZs with n =1,2,..) based on analytical approaches confirming BLS measurements[92]. More specifically, the experimental BLS dispersion was measured for a bicomponent MCs consisting of Co cylindrical dots partially embedded into a Py continuous film and was theoretically determined by using an analytical approach, called plane wave method (PWM)[10]. Another important feature of MCs with a complex base, i.e. where two dots or stripes of different shape or constituting materials form the basic unit cell, is that the magnetic order may not coincide with the geometrical one and, as a consequence, the dynamic response can be tuned in a reprogrammable way by varying the magnetic field strength[48,93,94,95]. With the aim of investigate this phenomena, very recently the dynamic properties of array of bicomponent structures consisting of closely-spaced Py/Co elliptical dots have been investigated by all-optical time-resolved magneto-optical Kerr effect microscopy[91]. Similar arrays of bicomponent Py/Nickel elliptical dots, with integrated coplanar wave guide, have been

studied by Ding et *al*[55,96] in both the parallel and anti-parallel ground state by using broadband FMR. Moreover, changes of dot or AD shape, their rotation with respect to the crystallographic axes, imperfections in their shape or at their edges can further modify SW spectra. In particular, no enough attention has been given to the study of collective dynamics in bicomponent MCs where a non-magnetic spacer separates the two magnetic materials.

In order to improve the basic knowledge of SWs in bicomponent MCs, in this Chapter three different analysis have been performed. These studies focuse on the important part of magnetism devoted to SW phenomena in composite structures, which is almost unexplored in the case of large scale 2D bicomponent nanopatterned systems. This investigation is also of interested for technological applications in the area of magnonics, magnetic memories and metamaterials. In particular in Section 4.1, four different MCs composed of Co circular dots embedded into a Py matrix are analysed with the aim of investigating the effect of the presence of the two ferromagnetic materials on the SWs modes propagating in the MCs. By the calculation of the band structures of the magnonic modes, it is possible to examine the effect of the position and of the volume of the Co circular dots inside the Py matrix. Moreover, by introducing the notion of effective surface magnetic charges, the dispersion curves and demagnetizing field can be explained from a physical point of view. Since the magnetization contrast between the two ferromagnetic materials plays a crucial role in the magnetic properties of the four systems, the corresponding systems with interchanged materials have been studied. In addition, the band structures of the Co/Py systems have been compared with the corresponding ones of the Py/Co systems. Finally, some analytical calculations are presented in order to give a quantitative behaviour of effective surface magnetic charges.

Section 4.2 is devoted to the study of the static and dynamic properties of the magnetization in bicomponent elliptical dots. The system is composed of Py and Co elliptical dots, interacting each other and placed into an array of non-interacting elements. It is interesting to note that this system shows a ferromagnetic and an antiferromagnetic phases. For both the magnetic configurations, the collective excitations have been analysed as a function of the external magnetic field. The theoretical results obtained by means of the DMM have been compared with the BLS experimental measurements performed at the Department of Physics and Geology of the University of Perugia. Finally, the effect of the gap between the two dots on the spin dynamics of the system have been investigated by varying the separation between the two ferromagnetic materials. In order to explain this effect, the dipolar dynamic coupling has been evaluated together with the amplitude distribution of the SWs modes for both the P and AP state, attained by sweeping the applied field along the major and minor hysteresis loop. This latter field sequence provides a simple method to identify the mode localization inside the dot of different magnetic materials.

Finally, in Section 4.3, study of the effect of a non-magnetic spacer in 2D MCs on the dispersions of the relevant SWs is theoretically studied. This is done to investigate the important spin dynamics effects due the significant spatial variations experienced by the total inhomogeneous magnetic field because of the non-magnetic material at the interface between two ferromagnetic materials. In this respect, it is studied the magnetization dynamics in square lattice 2D MCs with square ADs partially filled with different magnetic

materials; however the obtained results can be easily generalized to other geometries. In this study two types of separation between dots and Py matrix are considered: a) with the non-magnetic spacer located only below the dot, and b) with the spacer fully around the dot. In order to understand the effect of the non-magnetic spacer on the dispersion curves and on the spatial profiles of SWs modes of the investigated structures, the in-plane components of the total (effective) magnetic field has been calculated at different values of z. The group velocity and band width have been calculated in order to study additional effects of the presence of the non-magnetic spacer.

4.1 Band structure of bicomponent magnonic crystals

4.1.1 Bicomponent magnonic crystals

The systems studied here are bicomponent MCs composed of Py and Co. Using the DMM[51,31] extended to the case of multicomponent MCs composed of different ferromagnetic materials, the dynamical properties of four Py/Co systems have been studied. To refer to the MCs the first material (Py) indicates to the continuous film, while the second one (Co) to the cylindrical dot. In the calculations it is taken j=1,2 so that: $M_s(1) = M_{s,Py}$, $M_s(2) = M_{s,Co}$, $\gamma(1) = \gamma_{Py}$, $\gamma(2) = \gamma_{Co}$ and $A_{exch}(1) = A_{exch}^{Py}$ and $A_{exch}(2) = A_{exch}^{Co}$. The four systems are depicted in Fig. 4.1. The geometric parameters of these systems are the following: the lattice constant is a = 600 nm, the Co circular dot has a diameter d = 310 nm and the thickness of the continuous film is L_{Py} = 16 nm for every system. In system 1 (see Fig. 4.1(a)) the Co circular dot is totally embedded into the Py film. In system 2 it is partially embedded into Py film (L_{Co} = 8 nm) (Fig. 4.1(b)). In system 3 the thickness of the Co circular dot is L_{Co} = 16 nm, but it is etched only 8 nm into Py film, while in system 4 it is above the Py film (L_{Co} = 8 nm) (Fig. 4.1(c) and (d)). The bicomponent MCs studied are 2D periodic (in the x-y plane), but they can be regarded as 3D, since the magnetization is assumed non uniform not only in the x-y plane, but also along z. The non uniform magnetization along the thickness which is mainly due to the contrast between the two ferromagnetic materials is taken into account by subdividing in the simulations the systems into a stack of layers along z.

The top view of the four systems together with the directions of the external magnetic field **H** along the y-axis and of **K** along the x-axis are also shown in Fig. 4.1(e).

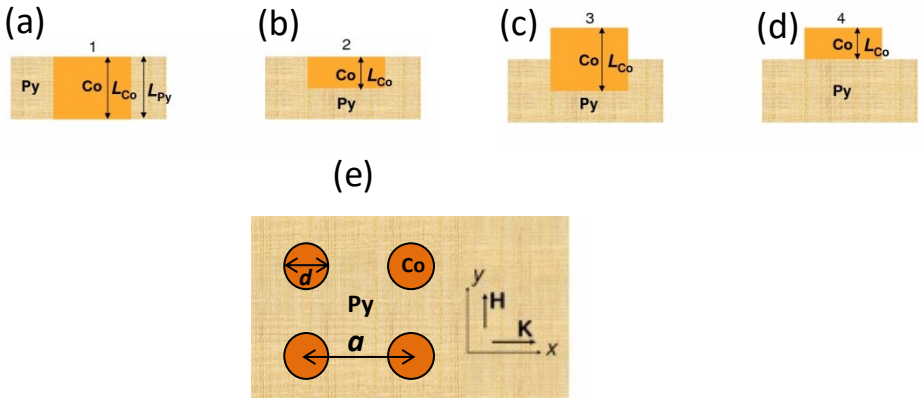

Fig. 4.1. (a) Pictorial sketch of system 1. (b) as in panel (a) but for system 2. (c) as in panel (a) but for system 3. . (d) as in panel (a) but for system 4. The thickness L_{Py} of the Py film and the thickness L_{Co} of the Co cylindrical dots are indicated . (d) The top view of the four Py/Co bicomponent MCs together with the reference frame and with the directions of **H** and of **K** are also shown.

The reference filling fraction *ff* is defined as the ratio between the Co volume V_{Co} and the primitive cell volume V_{Cell}, namely V_{Co}/V_{Cell}, when the Co cylindrical dots are completely embedded into the Py film, namely $ff = \pi \frac{R^2}{a^2}$ where *R* is the Co dot radius. In order to distinguish the spin dynamics in the four systems, each system has been characterized by means of the ratio $V_{Co}/V_{Cell.}$ in the form

$$\eta_1 = ff,\ \eta_2 = \frac{ff}{2},\ \eta_3 = \frac{2ff}{2+ff},\ \eta_4 = \frac{ff}{2+ff} \tag{4.1}$$

with η_i =1,2,3,4. The above ratios indicates the quantity of Co and the Co position within the primitive cell and are expressed in terms of the reference filling fraction *ff*. The numerical values are: $\eta_1 \approx 21$ %, $\eta_2 \approx 11$ %, $\eta_3 \approx 19$ % and $\eta_4 \approx 10$ %. The ground-state magnetization is determined by using OOMMF with PBCs[49] by dividing the systems in micromagnetic cells of 7.5 nm × 7.5 nm × 8 nm size. Since the position involves also the thickness, the systems can be regarded as 3D bicomponent MCs. The magnetic parameters used in the simulations are within the values used in the literature. For Py: $\gamma_{Py}/2\pi$ = 2.96 GHz/kOe, $M_{s,Py} = 740\,\text{emu/cm}^3$, $A^{Py}_{exch} = 1.3\times10^{-6}\,\text{erg/cm}$, while for Co: $\gamma_{Co}/2\pi$ = 3.02 GHz/kOe, $M_{s,Co} = 1000\,\text{emu/cm}^3$ and A^{Co}_{exch} = 1.5 × 10^{-6} erg/cm (this value is typical of polycrystalline Co). The size of the micromagnetic cell is comparable to the exchange lengths of Py and Co, according to $l^{Py}_{exch} = \sqrt{\frac{A^{Py}}{2\pi M^2_{s,Py}}} \simeq$ l $\sqrt{\frac{A^{Co}}{2\pi M_{s,Co}}} \simeq$ respectively. The exchange constant at the interface between the two ferromagnetic materials is considered equal to the average between the exchange stiffness constant of the two ferromagnetic materials, namely $\bar{A}^{Py\text{-}Co}_{exch} = \left(A^{Py}_{exch} + A^{Co}_{exch}\right)/2$. Simulations

are performed at a fixed **H** applied parallel to the *y*-axis of intensity H = 500 Oe sufficient to reach a quasi-collinear ground-state magnetization along the *y*-direction.

4.1.2 Dispersion behaviour

The effect of the Co volume V_{Co} and of the Co position within the primitive cell on mode dispersion is investigated calculating the band structures of the most relevant SWs modes of the systems. By giving a simple description of the underlying physics the notion of effective "surface magnetic charges" is introduced. Moreover, the band gaps at the boundaries of the *n*BZ of the most representative modes are calculated and the effect of the interchange between the two ferromagnetic materials on the modes dispersions is analyzed. Note that the obtained results can be considered of general validity for other lattice constants in the submicrometric range, for other dot diameters of nanometric size and for different couples of magnetic materials having an appreciable magnetic contrast.

Prior to starting the analysis of the band structures of the collective excitations it is important to discuss the distribution of "surface magnetic charges" across the interface between the two ferromagnetic materials and the corresponding demagnetizing fields in the Py film and inside the Co cylindrical dots. The effective "surface magnetic charge" picture is valid for systems 1, 2 and 3 where there are common lateral surface between Py and Co but it reduces to real "surface magnetic charges" for system 4. In Fig. 4.2 the effective "surface magnetic charges" distribution is shown.

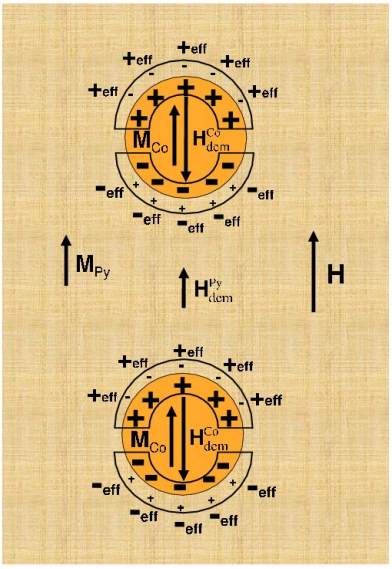

Fig. 4.2. Top of the view of the distribution of "surface magnetic charges" for the Py/Co systems 1, 2 and 3. The positive and negative effective "surface magnetic charges" are shown and labeled with the subscript "eff". The directions of $\mathbf{M}_{Py}$, $\mathbf{M}_{Co}$ and **H** together with those of the Co and Py static demagnetizing fields $\mathbf{H}_{dem}^{Co}$ and $\mathbf{H}_{dem}^{Py}$, respectively, are also displayed.

The external magnetic field is applied along the *y*-axis and induces the orientation along the same direction both $\mathbf{M}_{Py}$ and $\mathbf{M}_{Co}$, in the Py film and inside the Co dot, respectively. A small deviation from the collinear state of the $\mathbf{M}_{Py}$ and $\mathbf{M}_{Co}$ can be observed close to the dot surface. This leads to the formation of "surface magnetic charges" of opposite sign and of different magnitude at the interface between Py and Co. The net effect is the creation of effective "surface magnetic charges" that have the same signs of the ones resulting from $\mathbf{M}_{Co}$, because of the larger value of $M_{s,Co}$ with respect to $M_{s,Py}$. This effect is shown in Fig. 4.2 even if the effective "surface magnetic charge" picture is strictly valid for systems 1, 2 and 3. For system 4, where a common lateral surface between the two ferromagnetic materials is absent, the effective "surface magnetic charges" reduce to the real "surface magnetic charges" at the edge of the Co circular dots. As a result, the static demagnetizing field (*y*-component) is parallel to **H** in the Py horizontal channels, while it is anti-parallel to **H** in the Co cylindrical dots and in the horizontal rows comprised between them. Note that the static demagnetizing fields, denoted by $\mathbf{H}_{dem}^{Py}$ and $\mathbf{H}_{dem}^{Co}$, respectively are the demagnetizing fields placed in the horizontal channels and horizontal rows, respectively, but are not only due to either Py or Co. Indeed, both demagnetizing fields have a non local origin and are due to the combination of Py and Co effects.

The relevant magnonic modes of these systems have Damon-Eshbach-like (DE) character with nodal planes parallel to the local direction of the static magnetizations $\mathbf{M}_{Py}$ and $\mathbf{M}_{Co}$. The mode classification is similar to that for 2D AD lattices [71] introduced in Chapter 3. The two most relevant modes found in bicomponent magnetic systems are called DE_{nBZ} and DE_{nBZ}^{HR}, where *n* indicates the number of the Brillouin zone (*n*BZ) with *n*=1,2,... . The DE_{nBZ}^{HR} modes are mainly localized in the horizontal rows containing Co cylindrical dots with a lower amplitude inside the Co cylindrical dots, but their amplitude can be rather large also along the horizontal channels. Instead, the DE_{nBZ} modes have amplitudes spreading mainly in the Py film with maxima in the horizontal channels, but with appreciable amplitude also in the horizontal rows containing Co cylindrical dots especially towards the edges of *n*BZs with *n*=1,2,... . The Fig. 4.3 shows the spatial profiles of the DE_{1BZ} and the DE_{1BZ}^{HR} modes at the Γ point and at the X point calculated for the system 1 at $z = L_{Py} = 16$ nm (top surface of Py film). Indeed, according to the calculation their localization properties along the thickness do not essentially change. Moreover, spatial profiles of the DE_{nBZ} and DE_{nBZ}^{HR} collective modes for the systems 2, 3 and 4 (not shown) have features similar to those shown for system 1 and do not exhibit appreciable differences in their amplitude behavior along the *z* direction. This similar behaviour is in turn due to the fact that collective modes experience an effective field resulting from the combined contribution of the static demagnetizing fields of the two ferromagnetic materials also in the regions along the thickness where there is only one material.

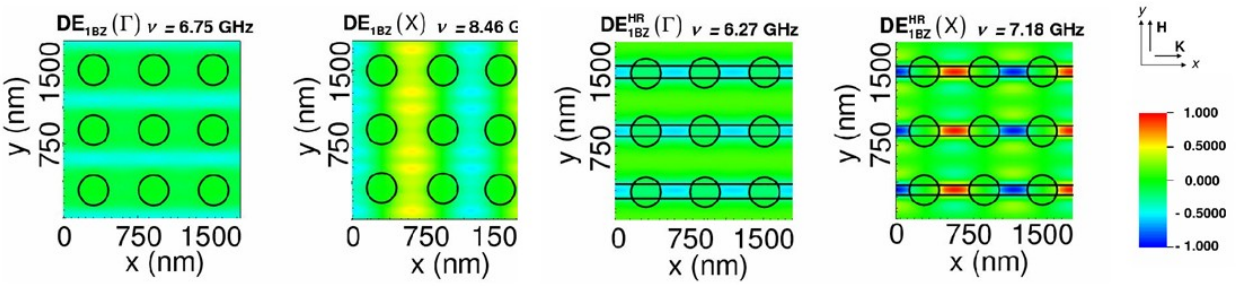

Fig. 4.3. Spatial profiles (Re[δm_z], real part of the z-component of the dynamic magnetization) of the DE_{1BZ} and DE^{HR}_{1BZ} modes in 3 × 3 primitive cells both at the center of the 1BZ (Γ point) and at the border of the 1BZ (X point) for the Py/Co system 1 plotted at $z = L_{Py}$. A reference frame is also shown together with the directions of **H** and **K**.

By comparing the band structure of the four different systems, it is possible to study: 1) the effect of V_{Co} within the primitive cell and 2) the effect of the position of Co inside the primitive cell on mode dispersion. In order to investigate the effect of V_{Co}, a comparison between the calculated dispersion for systems 1 and 2 and for systems 3 and 4, having the same value of V_{Co} respectively is needed (see Fig. 4.4(a) and (b), respectively). In particular, V_{Co} for systems 2 and 4 is half the corresponding values assumed in systems 1 and 3, respectively. For both cases, the DE^{HR}_{nBZ} dispersion is always downshifted with respect to that of DE_{nBZ}. This behaviour can be explained by taking into account that the DE^{HR}_{nBZ} modes frequencies experience a larger negative static demagnetizing field, because of their larger localization in the horizontal rows comprised between Co cylindrical dots where $\mathbf{H}^{Co}_{dem}$ is antiparallel to **H**.

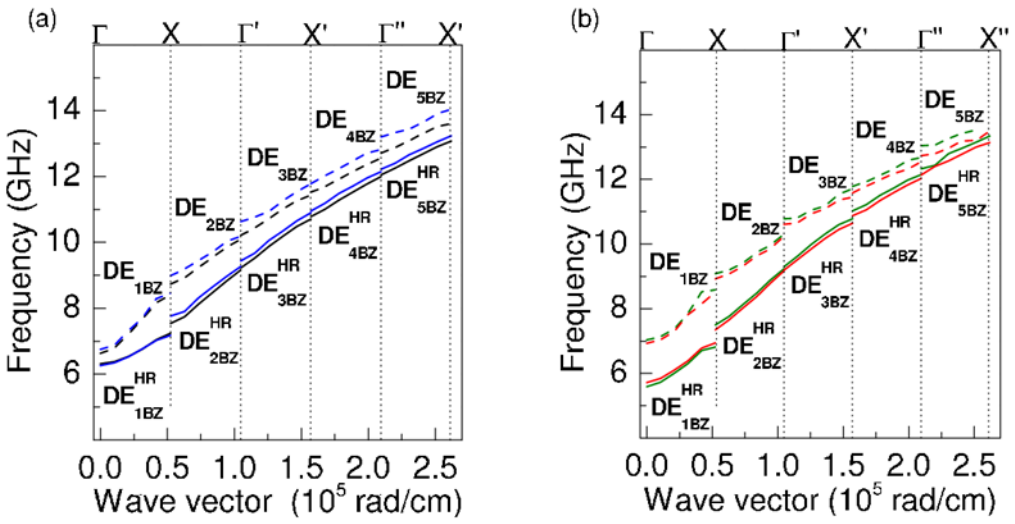

Fig. 4.4. Frequency dispersion of the two most relevant collective modes for the Py/Co bicomponent MCs. (a) Frequency dispersion for systems 1 and 2. Solid (dashed) blue lines: $\mathrm{DE}^{\mathrm{HR}}_{n\mathrm{BZ}}\left(\mathrm{DE}_{n\mathrm{BZ}}\right)$ for system 1. Solid (dashed) black lines: $\mathrm{DE}^{\mathrm{HR}}_{n\mathrm{BZ}}\left(\mathrm{DE}_{n\mathrm{BZ}}\right)$ for system 2. (b) As in panel (a) but for systems 3 and 4. Solid (dashed) green lines: $\mathrm{DE}^{\mathrm{HR}}_{n\mathrm{BZ}}\left(\mathrm{DE}_{n\mathrm{BZ}}\right)$ for system 3. Solid (dashed) red lines: $\mathrm{DE}^{\mathrm{HR}}_{n\mathrm{BZ}}\left(\mathrm{DE}_{n\mathrm{BZ}}\right)$ for system 4.

Fig. 4.4(a) shows that the frequencies of the $\mathrm{DE}^{\mathrm{HR}}_{n\mathrm{BZ}}$ and the $\mathrm{DE}_{n\mathrm{BZ}}$ modes for system 2 are slightly downshifted with respect to the corresponding ones for system 1. This phenomena can be attributed to the larger demagnetizing effects on mode frequencies. Albeit the magnitude of $\mathbf{H}^{\mathrm{Co}}_{\mathrm{dem}}$ which is antiparallel to **H** is smaller for system 2, there is also a strong reduction, passing from system 1 to system 2, of the magnitude of $\mathbf{H}^{\mathrm{Py}}_{\mathrm{dem}}$ which is antiparallel to $\mathbf{H}^{\mathrm{Co}}_{\mathrm{dem}}$ and thus parallel to **H** (see Fig. 4.2). As a consequence, the magnitude of the total static demagnetizing field antiparallel to **H** is small, but enough to lead to the slight downshift of frequencies in system 2 with respect to the corresponding ones in system 1. In Fig. 4.4(b) the calculated dispersions for systems 3 and 4 are shown. Interestingly, when the Co cylindrical dots are above the Py film (system 4), both dispersions (red lines) are slightly downshifted with respect to those of system 3 (green lines) with the only exception of the $\mathrm{DE}^{\mathrm{HR}}_{1\mathrm{BZ}}$ mode. This is due to the effect of the negative magnitude of the $\mathbf{H}^{\mathrm{Co}}_{\mathrm{dem}}$ in system 4 that is slightly larger (negatively) than the corresponding one in system 3. As a matter of fact, in system 3 the large magnitude of $\mathbf{H}^{\mathrm{Co}}_{\mathrm{dem}}$ is partially counterbalanced by the magnitude of $\mathbf{H}^{\mathrm{Py}}_{\mathrm{dem}}$ which has an opposite direction (see Fig. 4.2). Note that, due to the non local nature of $\mathbf{H}^{\mathrm{Co}}_{\mathrm{dem}}$, also in system 4 there is an effect on $\mathrm{DE}_{n\mathrm{BZ}}$ mode dispersion of the Co static demagnetizing field. Moreover, the band gap at the border of the 1BZ between the $\mathrm{DE}^{\mathrm{HR}}_{1\mathrm{BZ}}$ and the $\mathrm{DE}^{\mathrm{HR}}_{2\mathrm{BZ}}$ for systems 3 and 4 is very large due to the presence of Co above the Py surface that acts like a band gap amplifier.

Secondly, the effect of the position of Co for a fixed V_{Co} inside the primitive cell on the frequency dispersion of the most relevant magnonic modes is investigated. With this aim, the frequency dispersion of systems 1 and 3 and that of systems 2 and 4, are compared in Fig. 4.5(a) and (b), respectively. In systems 1 and 3 the V_{Co} is twice with respect to systems 2 and 4.

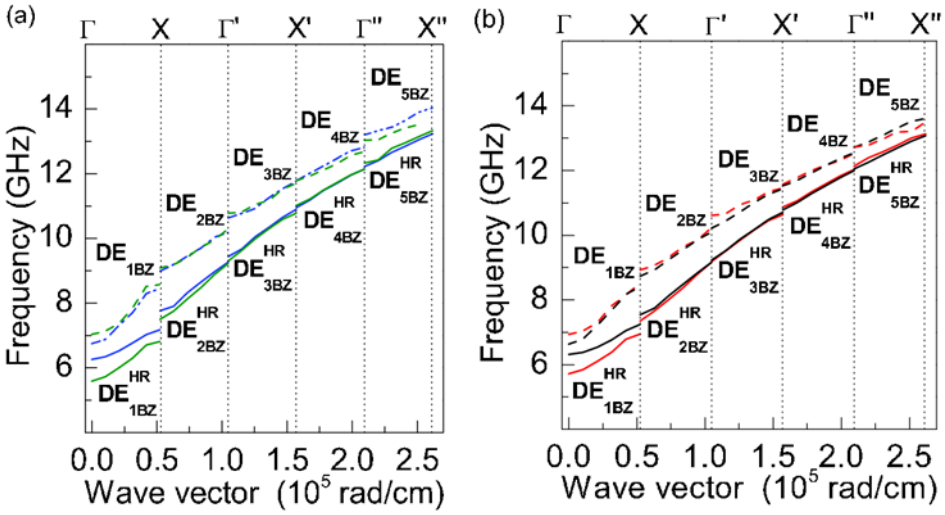

Fig. 4.5. Frequency dispersion of the two most relevant collective modes for the Py/Co bicomponent MCs. (a) Frequency dispersion for systems 1 and 3. Solid (dashed) blue lines: $\mathrm{DE}_{n\mathrm{BZ}}^{\mathrm{HR}}\left(\mathrm{DE}_{n\mathrm{BZ}}\right)$ for system 1. Solid (dashed) green lines: $\mathrm{DE}_{n\mathrm{BZ}}^{\mathrm{HR}}\left(\mathrm{DE}_{n\mathrm{BZ}}\right)$ for system 3. (b) Frequency dispersion for systems 2 and 4. Solid (dashed) black lines: $\mathrm{DE}_{n\mathrm{BZ}}^{\mathrm{HR}}\left(\mathrm{DE}_{n\mathrm{BZ}}\right)$ for system 2. Solid (dashed) red lines: $\mathrm{DE}_{n\mathrm{BZ}}^{\mathrm{HR}}\left(\mathrm{DE}_{n\mathrm{BZ}}\right)$ for system 4.

By looking at the $\mathrm{DE}_{n\mathrm{BZ}}^{\mathrm{HR}}$ dispersion in Fig. 4.5(a), it is possible to note that the collective mode frequencies in system 3 (green lines) are slightly downshifted with respect to the ones in system 1, especially in the 1BZ and 2BZ, while for *n*BZs with n = 3, 4,… they merge asymptotically. This behaviour can be understood by taking into account that in system 3 the Co cylindrical dots are only partially embedded into the Py film resulting in a higher and more negative magnitude of the total static demagnetizing field experienced by the collective modes. The higher total static demagnetizing field is not related to the $\mathbf{H}_{\mathrm{dem}}^{\mathrm{Co}}$ itself that is approximately the same in the two systems, but is due to the decrease of the magnitude of $\mathbf{H}_{\mathrm{dem}}^{\mathrm{Py}}$ in system 3 with respect to that of $\mathbf{H}_{\mathrm{dem}}^{\mathrm{Py}}$ in system 1. For increasing Bloch wave vector the static effective field effect is masked by the increase of the dynamic dipolar and exchange effects which become predominant. The $\mathrm{DE}_{n\mathrm{BZ}}$ dispersion is essentially at the same frequencies independently of the Co position. Indeed, the $\mathrm{DE}_{n\mathrm{BZ}}$ collective modes are mainly confined in the Py film and experience slightly the variation of the static demagnetizing field due to the change of position of the Co cylindrical dot passing from system 1 to system 3. Similar conclusions can be drawn by discussing the dispersion in systems 2 and 4, respectively shown in Fig. 4.5(b).

Moreover, each dispersion exhibits BGs at *n*BZ boundaries caused by the Bragg diffraction of collective modes, with no exceptions [70,92]. Hence, the behaviour of BGs and bandwidths (BWs) found according to DMM simulations for the four systems studied is briefly discussed. The amplitudes of BGs of $\mathrm{DE}_{n\mathrm{BZ}}$ collective modes decrease with increasing the *n*BZ order for the range of Bloch wave vectors investigated (up to the 4BZ) exhibiting a similar behaviour to that shown by BGs of extended modes in AD lattices [70]. For example, for system 1, the BG amplitude reduces to about 0.39 GHz at the border of 4BZ. A similar trend, but with different BG amplitudes, is exhibited for the other systems investigated. On the other hand, the amplitudes of BGs for system 1 of the $\mathrm{DE}^{\mathrm{HR}}_{n\mathrm{BZ}}$ collective modes have the same trend as that of the $\mathrm{DE}_{n\mathrm{BZ}}$ ones by reducing to about 0.10 at the border of 4BZ. Instead, for systems 2, 3 and 4 the amplitudes of BGs of $\mathrm{DE}^{\mathrm{HR}}_{n\mathrm{BZ}}$ decrease up to the 2BZ, but they have an oscillating trend for n >2. Concerning amplitude of BGs, note that it is larger at each *n*BZ boundary for systems 1 and 3 characterized by larger η_1 and η_3. Hence, the perturbation which produces the BGs is proportional to the quantity of Co. Also the presence of Co above the Py surface plays a role in increasing the BG amplitude, which is larger for system 4 with respect to system 2, although $\eta_4 \approx \eta_2$. Instead, BWs of $\mathrm{DE}_{n\mathrm{BZ}}$ collective modes have a weak dependence on the system studied, reducing approximately on average from about 1.6 GHz (first band) to about 1 GHz (fifth band) for all systems studied. A different behaviour is exhibited by BWs of $\mathrm{DE}^{\mathrm{HR}}_{n\mathrm{BZ}}$, which tend to slightly increase with increasing n passing, for every system, from approximately 1 GHz (first band) to about 1.2 GHz (fifth band). This trend may be attributed to the exchange effect due to Co which could become important for intermediate and large Bloch wave vectors.

4.1.3 Effective surface magnetic charge

At the border of Co cylindrical dots, an effective "surface magnetic charge" density can be defined for Py/Co systems, as the linear combination of the "surface magnetic charge" densities of the two ferromagnetic materials, viz. $\sigma_{\mathrm{eff}} = \mathbf{M}_{\mathrm{Py}} \cdot \hat{n} + \mathbf{M}_{\mathrm{Co}} \cdot \hat{n}'$. Here $\hat{n}$ is the unit vector associated to $\mathbf{M}_{\mathrm{Py}}$ external to Py film, but internal to Co cylindrical dot, while $\hat{n}'$ is the corresponding unit vector associated to $\mathbf{M}_{\mathrm{Co}}$ external to Co cylindrical dot, but internal to Py film. In Fig. 4.6 both unit vectors are depicted along the direction of the static magnetizations. It is important to note that this scheme is valid for systems 1, 2 and 3 where the lateral surface of the cylinder (or part of it) is in common between Co and Py.

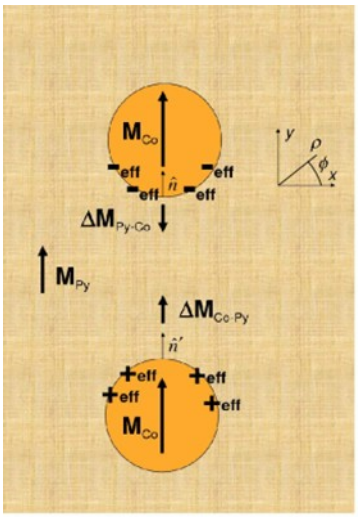

Fig. 4.6. Pictorial sketch of the orientation of the unit vectors normal to the Py/Co interface in the plane of the system. The direction of the vector $\Delta\mathbf{M}_{\text{Co-Py}}$ together with the effective "surface magnetic charges" for systems 1, 2 and 3 are also depicted. An in-plane reference frame together with the cylindrical coordinates (ρ, ϕ) is also illustrated.

Moreover it is possible to express the quantity σ_{eff} in the form

$$\sigma_{\text{eff}} = \Delta\mathbf{M}_{\text{Co-Py}} \cdot \hat{n}', \tag{4.2}$$

with $\hat{n} = -\hat{n}'$ and the vector $\Delta\mathbf{M}_{\text{Co-Py}} = \mathbf{M}_{\text{Co}} - \mathbf{M}_{\text{Py}}$. The effective "surface magnetic charge" density is thus proportional to the difference between the magnetizations of the two ferromagnetic materials. In particular, for system 1, Eq. (4.2) holds for $0 \le z \le L_{\text{Py}}$, where $z = 0$ indicates the bottom surface of the primitive cell, while for system 2 it holds for $L_{\text{Py}}/2 \le z \le L_{\text{Py}}$. In system 3 a part of the Co cylindrical dot is above the Py film so that the effective "surface magnetic charge" density takes different expressions depending on the z coordinate,

$$\sigma_{\text{eff}} = \begin{cases} \Delta\mathbf{M}_{\text{Co-Py}} \cdot \hat{n}' & \text{if } L_{\text{Py}}/2 \le z \le L_{\text{Py}} \\ \mathbf{M}_{\text{Co}} \cdot \hat{n}' & \text{if } L_{\text{Py}} < z \le L_{\text{Py}} + L_{\text{Co}} \end{cases}. \tag{4.3}$$

Finally, for system 4 σ_{eff} becomes $\sigma_{\text{Co}} = \mathbf{M}_{\text{Co}} \cdot \hat{n}'$, because the "surface magnetic charges" are solely due to the Co dot above the Py film.

In the general case, the ground-state magnetization is not collinear and has a three-dimensional spatial dependence on $\mathbf{r} = (x,y,z)$, so that it is possible to define an effective magnetic potential expressed in terms of both the "volume magnetic charges" and the effective "surface magnetic charges" for Py/Co system, viz.

$$\Phi_{\text{M}}^{\text{Py/Co}}(\mathbf{r}) = -\int_{V_{\text{cell}}-V_{\text{dot}}} \frac{\nabla\cdot\mathbf{M}_{\text{Py}}}{|\mathbf{r}-\mathbf{r}''|}\,d\mathbf{r}'' - \int_{V_{\text{dot}}} \frac{\nabla\cdot\mathbf{M}_{\text{Co}}}{|\mathbf{r}-\mathbf{r}''|}\,d\mathbf{r}'' + \int_{S} \frac{\sigma_{\text{eff}}}{|\mathbf{r}-\mathbf{r}''|}\,d\mathbf{S}'', \tag{4.4}$$

where $\mathbf{r} = (x,y,z)$ and S is the common lateral surface between the two ferromagnetic materials. Note that, while the volume contribution to the magnetic potential comes from the terms that refers separately to the two ferromagnetic materials, this is not true for the surface contribution where the effective "surface magnetic charge" density is related to the contrast between the magnetizations of the two ferromagnetic materials expressed by Eq. (4.2). From Eq. (4.4) it is straightforward to obtain, for the Py/Co systems, the static demagnetizing field $\mathbf{H}_{\text{dem}}(\mathbf{r}) = -\nabla\Phi_{\text{M}}^{\text{Py/Co}}(\mathbf{r})$ that has a spatial dependence and which includes contributions from both materials. From micromagnetic simulations applied to the most representative system 1 it was found that $\mathbf{H}_{\text{dem}}(\mathbf{r})$ has an appreciable y-component (along the direction of $\mathbf{H}$) and is uniform along z so that $\mathbf{H}_{\text{dem}}(\mathbf{r}) = \mathbf{H}_{\text{dem}}(\boldsymbol{\rho})$ and $\mathbf{H}_{\text{dem}}(\boldsymbol{\rho}) \simeq H^{y} \quad \boldsymbol{\rho})\hat{\mathbf{j}}$ with $\boldsymbol{\rho} = (x,y)$. As underlined previously, the demagnetizing field for investigating the MM propagating mode frequency has been determined via micromagnetic simulations that have confirmed that the demagnetizing field has contributions from both materials according to Eq. (4.4)).

4.1.4 Interchange between Co and Py: Co/Py systems

The Co/Py systems consist in a bicomponent MCs where the first material (Co) corresponds to the continuous film, while the second one (Py) to the cylindrical dot. Some interesting properties related to the study of the invariance of the effective magnetic potential of Eq. (4.4) under the interchange of the two ferromagnetic materials have been found. The effective magnetic potential of Eq.(4.7) is not invariant, that is $\Phi_{\text{M}}^{\text{Co/Py}} \neq \Phi_{\text{M}}^{\text{Py/Co}}$, due to the two volume contributions appearing in the first and second integral on the second member. However, by assuming that, for a quasi-collinear magnetization state like the one considered here, volume contributions are small and negligible, the effective magnetic potential of the Py/Co systems takes the simple form

$$\Phi_{\text{M}}^{\text{Py/Co}}(\mathbf{r}) = \int_{\text{S}} \frac{\sigma_{\text{eff}}}{|\mathbf{r}-\mathbf{r}''|} d\mathbf{S}''. \tag{4.5}$$

By introducing the cylindrical coordinates (ρ,ϕ,z) so that the surface integral of Eq. (4.5) for systems 1 and 2 reads

$$\Phi_{\text{M}}^{\text{Py/Co}}(\mathbf{r}) = R\,|\Delta M_{\text{s}}| \int_{0}^{2\pi} \int_{z_{\min}}^{z_{\max}} \frac{\sin\phi''}{\sqrt{(x-x'')^2 + (y-y'')^2 + (z-z'')^2}} d\phi'' dz'', \tag{4.6}$$

with $x = R\cos\phi$ and $y = R\sin\phi$, R the radius of the cylinder and $|\Delta M_{\text{s}}| = |M_{\text{s,Co}} - M_{\text{s,Py}}|$ the difference in modulus of the two saturation magnetizations. In Py/Co systems it is $|M_{\text{s,Co}} - M_{\text{s,Py}}| = M_{\text{s,Co}} - M_{\text{s,Py}}$, because $M_{\text{s,Co}} > M_{\text{s,Py}}$. In particular, for system 1, $z_{\min}$=0 and $z_{\max} = L_{\text{Py}}$, while for system 2 $z_{\min} = L_{\text{Py}}/2$ and

$z_{max} = L_{Py.}$ Unlike Eq. (4.3), the magnetic potential of Eq. (4.4) expressed only in terms of surface contributions is invariant with respect to the interchange of the two ferromagnetic materials, viz. $\Phi_{\mathrm{M}}^{\mathrm{Py/Co}} = \Phi_{\mathrm{M}}^{\mathrm{Co/Py}}$, because it depends on $|\Delta M_{\mathrm{s}}|$. Instead, for system 3

$$\Phi_{\mathrm{M}}^{\mathrm{Py/Co}}(\mathbf{r}) = R|\Delta M_{\mathrm{s}}|\int_0^{2\pi}\int_{L_{\mathrm{Py}}/2}^{L_{\mathrm{Py}}}\frac{\sin\phi''}{\sqrt{(x-x'')^2+(y-y'')^2+(z-z'')^2}}d\phi''dz'' + R\,M_{\mathrm{s,Co}}\int_0^{2\pi}\int_{L_{\mathrm{Py}}}^{L_{\mathrm{Py}}+L_{\mathrm{Co}}}\frac{\sin\phi''}{\sqrt{(x-x'')^2+(y-y'')^2+(z-z'')^2}}d\phi''dz'', \tag{4.7}$$

by accounting for the region where the Co dot is above the Py film.

For system 3 the invariance of the magnetic potential is broken, because of the presence of the second integral on the right member which would be proportional to $M_{\mathrm{s,Py}}$ upon interchange of the two ferromagnetic materials. This is in turn related to the fact that the second integral on the right member is expressed in terms of the "surface magnetic charge" density depending on one ferromagnetic material only.

Finally, for system 4, where the Co cylindrical dot is above the Py film, the magnetic potential becomes that of a Co cylindrical dot, namely $\Phi_{\mathrm{M}}^{\mathrm{Co}}(\mathbf{r})$ (second integral on the right member of Eq. (4.7)). As a result, since the Py contribution to the magnetic potential vanishes, the static demagnetizing field given in Eq. (4.7) reduces to the Co static demagnetizing field $\mathbf{H}_{\mathrm{dem}}^{\mathrm{Co}}(\mathbf{r})$ with $\mathbf{H}_{\mathrm{dem}}^{\mathrm{Co}}(\mathbf{r}) = -\nabla\Phi_{\mathrm{M}}^{\mathrm{Co}}(\mathbf{r})$. By applying the thin film limit the static demagnetizing field of a thin cylindrical dot is obtained[97].

Further interesting properties arise from the interchange between the two ferromagnetic materials. In the Co/Py systems the investigation of the propagation of collective modes in an array of Py cylindrical dots embedded into a Co film can be performed. In order to understand the dispersion behaviour that will be discussed later, it is useful to illustrate the corresponding distribution of effective "surface magnetic charges" shown in Fig. 4.7(a) for Co/Py systems 1 and 2 and in Fig. 4.7(b) for Co/Py system 3. Interestingly, for systems 1 and 2, the distribution of effective "surface magnetic charges" is opposite to that of Py/Co systems 1 and 2, while for systems 3 and 4 the charge distribution is the same as that of Py/Co system 3 and 4. First, the discussion is focused to the Co/Py systems 1 and 2. The effective "surface magnetic charges" at the interface between Py and Co take the sign of those of Co, because the "surface magnetic charge" density due to Co at the interface is higher with respect to that of Py. As a result, the interchange of the two ferromagnetic materials leads to a reversal of the orientations of $\mathbf{H}_{\mathrm{dem}}^{\mathrm{Py}}$ and $\mathbf{H}_{\mathrm{dem}}^{\mathrm{Co}}$ static demagnetizing fields with respect to the corresponding $\mathbf{H}_{\mathrm{dem}}^{\mathrm{Co}}$ and $\mathbf{H}_{\mathrm{dem}}^{\mathrm{Py}}$ ones of Py/Co systems 1 and 2, respectively. Note that, also for Co/Py systems, $\mathbf{H}_{\mathrm{dem}}^{\mathrm{Py}}$ ($\mathbf{H}_{\mathrm{dem}}^{\mathrm{Co}}$) is not only due to Py (Co), but to their combined effect. Now, systems 3 and 4 are discussed. For system 3, despite the interchange of the two ferromagnetic materials, the orientations of $\mathbf{H}_{\mathrm{dem}}^{\mathrm{Co}}$ and of $\mathbf{H}_{\mathrm{dem}}^{\mathrm{Py}}$ do not reverse with respect to the corresponding $\mathbf{H}_{\mathrm{dem}}^{\mathrm{Py}}$ and $\mathbf{H}_{\mathrm{dem}}^{\mathrm{Co}}$ of Py/Co system 3.

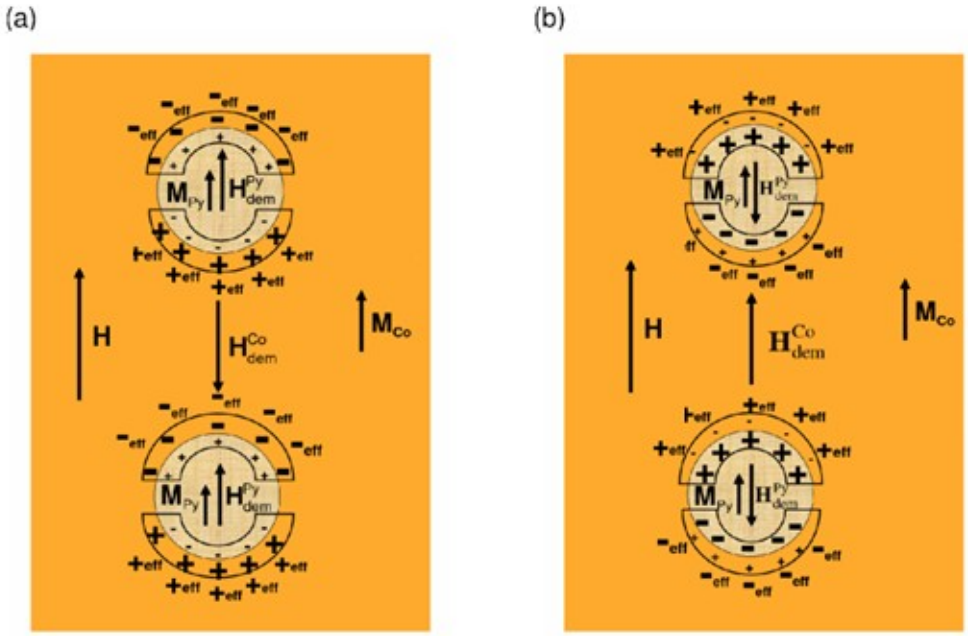

Fig. 4.7. (a) Distribution of "surface magnetic charges" for Co/Py systems 1 and 2: top view. (b) The same, but for Co/Py system 3. The meaning of the other symbols and of the vectors is the same as in Fig. 4.2.

This, in turn is due to the fact that the effective "surface magnetic charges" do not change sign with respect to the corresponding ones in the Py/Co systems 3 and 4. In particular, for system 3 there is a prevalence of the effect due to the Py "surface magnetic charges" corresponding to the portion of the Py dot above the Co film, while for system 4, where Py dots are completely above the Co film, the effective "surface magnetic charges" reduce to the ones created by $\mathbf{M}_{\mathrm{Py}}$.

Interestingly, the effect of the interchange of the two ferromagnetic materials reflects also on the frequency dispersion. The localization features of the two relevant families of collective modes in Co/Py systems change with respect to those of the corresponding modes in Py/Co systems and become more soft especially in system 1. However, it is still possible to distinguish the main differences. By looking at the spatial profiles of $\mathrm{DE}_{1\mathrm{BZ}}^{\mathrm{HR}}$ and $\mathrm{DE}_{1\mathrm{BZ}}$ modes in Co/Py system 1 shown in Fig. 4.8 and plotted at $z = L_{\mathrm{Co}}$, (top surface of the Co film), the $\mathrm{DE}_{n\mathrm{BZ}}^{\mathrm{HR}}$ modes are mainly localized inside Py cylindrical dots with a less accentuated localization in the portion of the horizontal rows comprised between Py dots, but spread also in the Co film.

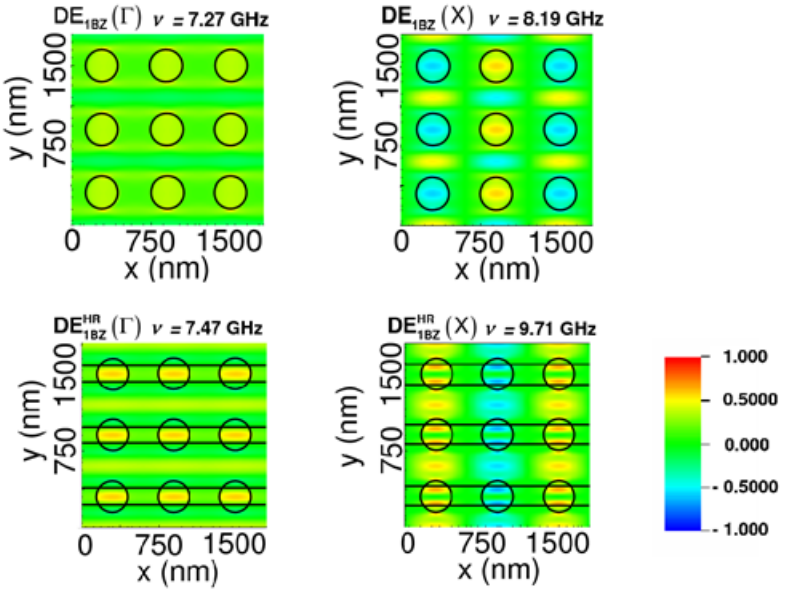

Fig. 4.8. Spatial profiles (Re[δm_z], real part of the z-component of the dynamic magnetization) of the $\mathrm{DE}_{1\mathrm{BZ}}$ and $\mathrm{DE}^{\mathrm{HR}}_{1\mathrm{BZ}}$ modes in 3 × 3 primitive cells at the centre (Γ point) and at the border of the 1BZ (X point) for Co/Py system 1 at $z = L_{\mathrm{Co}}$. The reference frame (not shown) is the same as in Fig. 3.

On the other hand, $\mathrm{DE}_{n\mathrm{BZ}}$ modes have a large amplitude in the Co film, but extend also in the horizontal rows, especially inside the Py dots where they eventually have the largest amplitude. It has been found that in every Co/Py system spatial profiles are essentially uniform along the z-direction. In Fig. 4.9(a) the dispersion of the two most relevant collective modes in Co/Py system 1 is shown. The interchange of the two ferromagnetic materials does lead in Co/Py system 1 also to the interchange of the two frequency dispersion. As a matter of fact, the $\mathrm{DE}^{\mathrm{HR}}_{n\mathrm{BZ}}$ modes have frequencies higher than those of $\mathrm{DE}_{n\mathrm{BZ}}$ modes. This different behaviour can be understood by studying the distribution of effective "surface magnetic charges" and the corresponding static demagnetizing fields illustrated in Fig. 4.7(a). The $\mathrm{DE}^{\mathrm{HR}}_{n\mathrm{BZ}}$ modes mainly experience the $\mathbf{H}^{\mathrm{Py}}_{\mathrm{dem}}$ that is parallel to $\mathbf{H}$ which causes an increase of the frequencies. Instead, the $\mathrm{DE}_{n\mathrm{BZ}}$ modes mainly experience the $\mathbf{H}^{\mathrm{Co}}_{\mathrm{dem}}$ which is antiparallel to $\mathbf{H}$ leading to a lowering of the corresponding frequencies. More generally, the frequency dispersion of each collective mode is upshifted with respect to the corresponding interchanged one in Py/Co system 1. The frequency dispersion of collective modes are interchanged also in Co/Py system 2 (not shown) with respect to the corresponding ones in Py/Co system 2, because of the similar distribution of "surface magnetic charges" (see Fig. 4.7(b)). Frequency dispersion in Co/Py system 3 are illustrated in Fig. 4.9(b) and can be considered representative qualitatively also of those in Co/Py system 4 (not shown). Dispersion curves of the two relevant families of modes having localization features very similar to the ones in Co/Py system 1 are not interchanged. Again, this can be understood by looking at the

distribution of effective "surface magnetic charges" (see Fig. 4.7(b)) that is qualitatively analogous to the one of Py/Co corresponding system 3 leading to $\mathbf{H}_{\mathrm{dem}}^{\mathrm{Co}}$ parallel to **H** and to $\mathbf{H}_{\mathrm{dem}}^{\mathrm{Py}}$ antiparallel to **H**. However, the dispersion curves in Co/Py systems 3 and 4 are up shifted with respect to the corresponding ones in Py/Co systems 3 and 4.

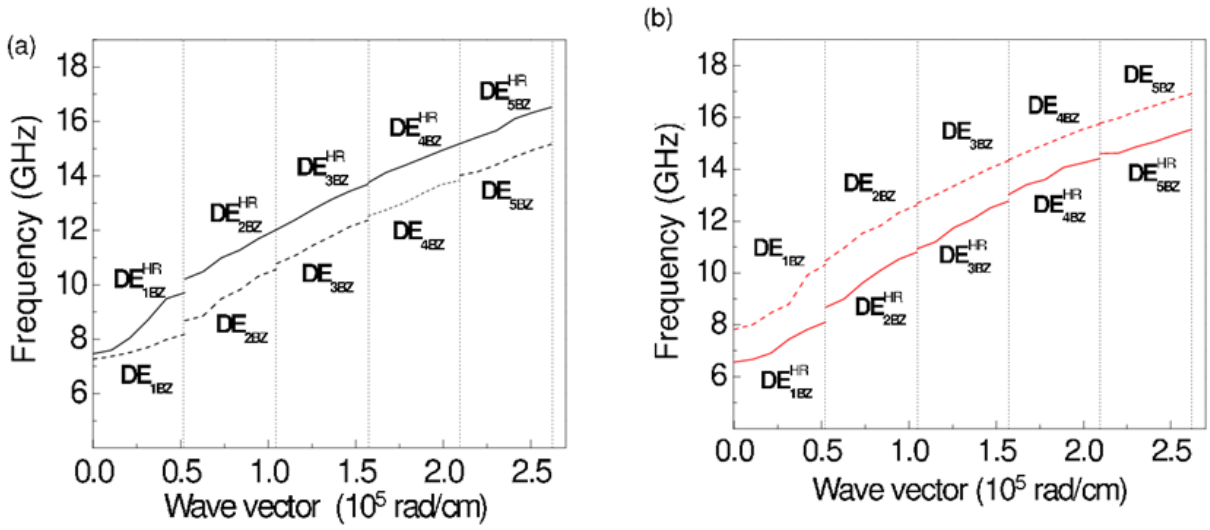

Fig. 4.9. (a) Frequency dispersion of the two main representative modes for the Co/Py system 1. Solid black line: $\mathrm{DE}_{n\mathrm{BZ}}^{\mathrm{HR}}$ modes. Dashed black line: $\mathrm{DE}_{n\mathrm{BZ}}$ modes. (b) As in panel (a), but for system 3. Solid red line: $\mathrm{DE}_{n\mathrm{BZ}}^{\mathrm{HR}}$ modes. Dashed red line: $\mathrm{DE}_{n\mathrm{BZ}}$ modes.

Finally, it is discussed the influence of the interchange between the two ferromagnetic materials on amplitudes of BGs and BWs. The general trend of both $\mathrm{DE}_{n\mathrm{BZ}}^{\mathrm{HR}}$ and $\mathrm{DE}_{n\mathrm{BZ}}$ modes for the Co/Py system 1 is the decrease of amplitudes of BGs with increasing the *n*BZ order for the range of Bloch wave vectors investigated showing a similarity with the dispersion in the corresponding Py/Co system 1. Also magnitudes of BG amplitudes are of the same order as those in Py/Co system 1. On the other hand, the behaviour of BWs for the two representative families of modes is opposite with respect to that in Py/Co system 1. As a matter of fact, in Co/Py system 1 BWs of $\mathrm{DE}_{n\mathrm{BZ}}$ increase with increasing *n*BZ, at least for n = 1,2, while BWs of $\mathrm{DE}_{n\mathrm{BZ}}^{\mathrm{HR}}$ decrease with increasing *n*BZ. The increasing trend of BWs of $\mathrm{DE}_{n\mathrm{BZ}}$ with increasing *n*BZ may be attributed to the large exchange Co effects due to the mode confinement at intermediate Bloch wave vectors. However, for both families of modes in Co/Py system 1, BWs have approximately on average the same magnitude as that in Py/Co system 1. Similar conclusions can be drawn for BGs and BWs of frequency dispersion in Co/Py system 3 shown in Fig. 4.9(b) and in Co/Py systems 2 and 4 (not shown).

4.2 Collective excitations in bicomponent magnonic crystals in the presence of a non-magnetic spacer

4.2.1 Systems and method

In order to investigate from a theoretical point of view the dynamical properties of 2D MCs in the presence of a non-magnetic spacers between ferromagnetic materials, the dispersion curves of the most relevant SWs modes for five different MCs have been calculated. The magnetic systems considered here are composed of Py, Co and non-magnetic material and are supposed to be infinite in plane (along x and y directions). All the systems have a square lattice structure with a lattice constant a = 400 nm and the magnetic dots have square shape. In Fig. 4.10 are shown the five systems analyzed: (a) **System 1** (**S1**): bicomponent MC composed of 30 nm thick Py film with an array of 20 nm deep square grooves of 200 nm size. In the bottom of grooves there is 10 nm thick non-magnetic material and then Co dots (20 nm thick) partially immersed into the grooves. The Co dots are in direct contact with Py only at lateral edges of the dot that is along the x and y directions. (b) **System 2-Co** (**S2^{Co}**): bicomponent MC similar to S1 but with 10 nm width spacer around the Co dots (200 nm wide). In S2^{Co}, Co dots and Py matrix are totally separated by a non-magnetic spacer. (c) **System 2-Py (S2^{Py}):** one component MC with the same geometry of S2^{Co} but with Py dots. (d) MC composed of square Py dots (10 nm thick and 200 nm wide) surrounded by non-magnetic spacer and fully immersed in the Py matrix. This is **system 3** (**S3**). (e) An array of squared Co dots (20 nm thick and 200 nm wide) constitutes the **system 4** (**S4**). The magnetic parameters used in the simulations are the typical parameters for Py and Co materials[31,92] : saturation magnetization for Py $M_{S,Py}$ = 750 emu/cm^3 and for Co $M_{S,Co}$ = 1200 emu/cm^3, exchange constants A_{Py} = 1.3 × 10^{-6} erg/cm and A_{Co} = 2.0 × 10^{-6} erg/cm, gyromagnetic ratios $\gamma_{Py}/2\pi$ = 2.96 GHz/kOe and $\gamma_{Co}/2\pi$ = 3.02 GHz/kOe. The static and dynamic properties of these magnetic systems have been investigated from a theoretical point of view by means of two micromagnetic codes: OOMMF code[49] and DMM program[28,31]. In particular, the ground-state magnetization is calculated by using OOMMF with 2D periodic boundary conditions and the obtained magnetic configuration is used as input to DMM. The DMM with implemented boundary conditions is applied to study the spin dynamic properties. Since the systems considered are composed of different materials, in the DMM two indexes have to be used: 1) an index k to label micromagnetic cells, with k = 1,2,… N, where N is the total number of micromagnetic cells in the primitive cell; 2) an index j = Py, Co indicates the ferromagnetic material. The number of micromagnetic cells assigned to the j-th ferromagnetic material is N_j such that $N_{Py} + N_{Co} = N$. Further details concerning the methods, OOMMF and DMM, were presented in Chapter 2. The size of the micromagnetic cells used in the static and dynamic simulations is 5 × 5 × 10 nm along x, y and z, respectively.

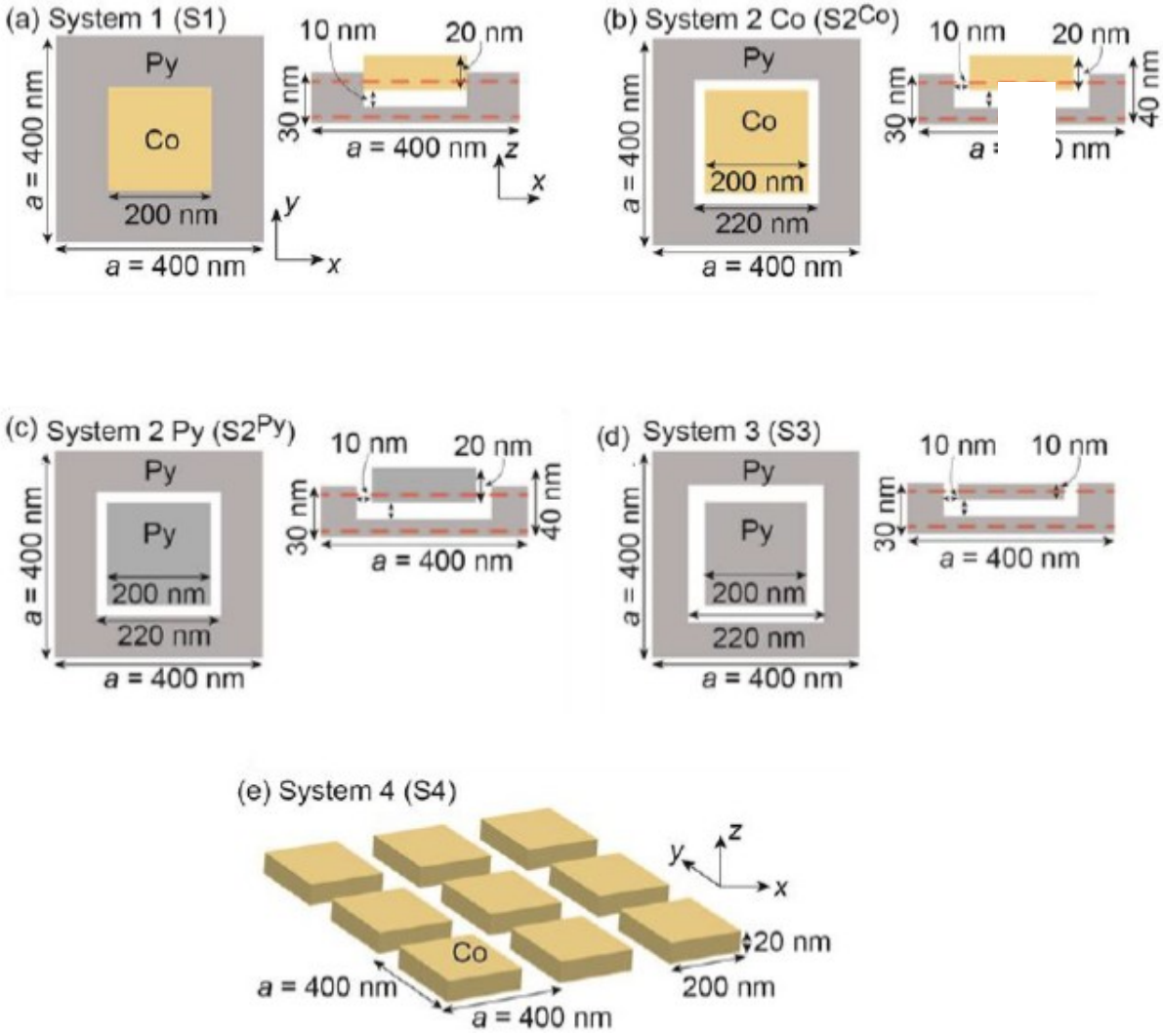

Fig. 4.10. (a) System 1: Top view of the primitive cell together with its perpendicular cross-section in a bicomponent MC consisting of square Co dots partially embedded in Py matrix. Non-magnetic spacer (white area) of 10 nm thick separates the bottom of Co dots from Py. (b) System 2-Co: similar to S1 but with total separation of Co dots from Py by means of 10 nm of non-magnetic spacer from the bottom and lateral sides of Co. (c) System S2-Py: one component MC with geometry equals to $S2^{Co}$ but with Py dot. (d) System 3: MC created by square array of square grooves in Py film partially filled with Py dots. Dots are separated from the matrix by 10 nm thick non-magnetic spacer. (e) System 4: square array of square Co dots. Red-dashed lines in the perpendicular cross-sections point at the planes (z = 5 and 25 nm) used in Figs. 4.21(a), (b), (c), (d) and (e) to show the spatial profiles of SW modes.

The systems have been studied in the DE so-called geometry i.e. by applying an external magnetic field (**H**) of magnitude fixed at 2000 Oe parallel to the y-axis and with the Bloch wave vector (**k**) parallel to the x-axis.

4.2.2 Spin wave excitations

In 2D AD lattices and bicomponent MCs a full magnonic spectra calculated by means of the DMM is very rich with plenty of SW excitations[98]. As an example, the differential scattering cross-section computed at the

center of the BZ is displayed in Fig. 4.11 for S1. It can be seen that a large number of SW modes results from the calculation. However, for the purposes of this study focused on the dispersion behavior in the first BZ only three modes belonging to the lowest frequency part of the spectrum, namely the ones exhibiting an appreciable differential scattering cross-section, have been selected in S1. The same conclusions on the differential scatting cross-section can be drawn also for the other systems.

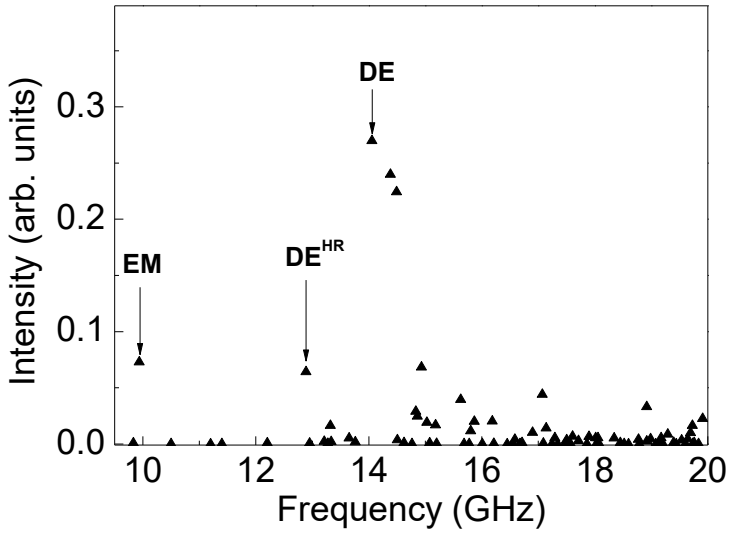

Fig. 4.11. Differential scattering cross-section calculated for S1 at the center of the BZ. The arrows label the modes with the highest intensity of the scattering cross section in the center of the first BZ investigated in this paper.

In Fig. 4.12 are collected the dispersion relations calculated for all the five systems studied for the SW modes exhibiting the largest differential scattering cross-section. The dispersion relations calculated for S1 are shown in Fig. 4.12(a). The collective modes have been classified by taking into account the region inside the primitive cell where they have the maximum amplitude, finding: 1) end mode of the dot (EM_d) (where the subscript "d" labels dot) that is a mode strongly localized at the borders of the square dots, 2) Damon-Eshbach-like mode is concentrated in the horizontal rows (DE^{HR}) and 3) Damon-Eshbach-like (DE) mode. The corresponding frequencies are 9.94, 12.89 and 14.06 GHz, respectively. The modes 2) and 3) are called Damon-Eshbach-like because they have nodal planes parallel to the local static magnetization in the higher BZs and no nodal planes in the center of the BZ (Fig. 4.13(a)). This agree with the classification of collective modes given for bicomponent MCs described in Sect. 4.1. The DE^{HR} mode is localized in the horizontal rows containing the square dots (with amplitude concentrated mainly in Py), while the DE mode has the maximum amplitude in Co dots and non-negligible amplitude in the Py film. It is interesting to note that the end mode detected here has been previously found only in one component MCs[29,30] but not in the bicomponent MCs[31,92] . The appearance of the end mode and the different SW amplitude distribution between Py and Co of DE and DE^{HR} modes underlines the difference between the S1 and the Co/Py bicomponent MC investigated in Sect. 4.1. These differences with respect to previous by studied systems are mainly due to: a) the presence of 10

nm thick non-magnetic spacer between Co dots and Py matrix placed at the bottom of the dots, and b) the dot shape (these effects will be discussed in the next paragraph). The next step is to investigate the effect of a full separation of Co dots from Py matrix on magnonic spectra. In Fig. 4.12(b), the calculated dispersion curves for $S2^{Co}$ are presented. By looking at Fig. 4.12(b) it is possible to observe the appearance of two new modes: the end mode of Py film (EM_f) with a frequency of 11.9 GHz (where the subscript "f" labels film) that is strongly localized at the border of Py film and the backward-like mode (BA^{HR}) with frequency of 13.86 GHz that is mainly concentrated in the horizontal rows. BA^{HR} mode exhibits nodal planes perpendicular to the local static magnetization (see Fig. 4.13(b) for the profiles of these modes). The frequency of the BA^{HR} in $S2^{Co}$ is higher than that of DE^{HR} and this is due to the strong localization of the BA^{HR} in the region filled by Co dots having magnetic parameters with values higher than that of Py. By comparing the frequency at the center of the BZ of S1 and $S2^{Co}$ systems, it is possible to observe a significant decrease of the EM_d frequency from 9.94 GHz in S1 to 4.217 GHz in $S2^{Co}$ and a slight increase of the DE (DE^{HR}) frequencies from 14.06 GHz in S1 (12.89 GHz) to 14.67 GHz (13.48 GHz) in $S2^{Co}$. The presence of five dispersion curves in $S2^{Co}$ is attributed to the fact that the differential scattering cross-section is comparable for the five SW excitations at the BZ center.

In order to understand the effect of the Py matrix on the SW excitation in Co dots, the dispersion curves of S4 (see Fig. 4.10 (e)), array composed of square Co dots, have been calculated. By inspection of Fig. 4.12(e) it is possible to see that the frequency of the EM_d in S4 (3.5 GHz) is about 6 GHz lower than in S1 and 2.5 GHz lower as compared to the corresponding one in $S2^{Co}$. Instead, the frequency of the DE mode (18.4 GHz) is 4 GHz higher than that in S1 and 3.5 GHz higher than that in $S2^{Co}$. Therefore, the effect of Py matrix is to lower the frequencies of the DE mode and to raise the frequencies of the EM_d. This behavior can be understood by taking into account the variation of the magnitude of the interdot dipolar dynamic coupling and of the static demagnetizing field passing from an array of dots (S4) to a MCs (S1 and $S2^{Co}$) composed by two ferromagnetic materials.

To study the effect of dot material and thickness in a Py matrix, the SW spectra of 2D MCs composed of Py dots in a Py matrix have been calculated. It is important to underline that $S2^{Py}$ and S3 are neither bicomponent MC, nor AD lattices, but these structures preserve properties of both with the use of a single ferromagnetic material. The kind of modes present in $S2^{Py}$ and S3 is similar to the one found in $S2^{Co}$. In $S2^{Py}$, the EM_d has a frequency of 8.92 GHz and is the lowest frequency mode as in $S2^{Co}$. The EM_f (10.46 GHz) in $S2^{Py}$ has a dispersion curve similar to that of EM_d. After these two modes it is present the DE mode with a frequency of 12.8 GHz at the center of the BZ. The frequencies of BA^{HR} mode (13.8 GHz) are lower than the ones of the DE^{HR} mode (14.12 GHz). By looking at Figs. 4.12(a) and (b) it is possible to observe that in $S2^{Py}$ the frequency sequence of DE, DE^{HR} and BA^{HR} modes is different from that in S1 and $S2^{Co}$. In particular, the DE mode frequencies are lower than the DE^{HR} mode ones as in the case of 2D one component AD lattices[29,70]. This can be explained by investigating the total field experienced by the modes, further details can be found in Sect. 4.2.3. The effect of the thickness of Py dots can be investigated by calculating the dispersion curves for S3. Fig. 4.20(d) shows the dispersion curves of the SW modes in S3. The EM_f (8.92

GHz) is the lowest frequency mode of the spectrum in S3. The EM_d frequency at the center of the BZ (12.84 GHz) is larger than that of the DE mode (12.36 GHz), however the corresponding dispersion curves have a similar trend. This frequency inversion as compared to $S2^{Py}$ is not surprising because the total magnetic field experienced by the EM_d is higher with respect to the field felt by the DE mode. The DE^{HR} and BA^{HR} modes have frequencies 14.68 and 14.12 GHz at the center of the BZ, respectively. Comparing the dispersion curves in $S2^{Co}$ and S3, it is possible to observe that the order of DE and DE^{HR} frequency mode in S3 is interchanged with respect to those in $S2^{Co}$. Moreover, also the frequency order of the EM_f and the EM_d is interchanged with respect to that in $S2^{Py}$ and $S2^{Co}$. This interchange can be attributed to the effect of the reduction of the dot thickness that induces a lowering of the total magnetic field in the Py film where the EM_f is localized. The intensities of the differential scattering cross-section of the DE, EM_d, EM_f and BA^{HR} modes are comparable but are 40% lower than that of DE^{HR}.

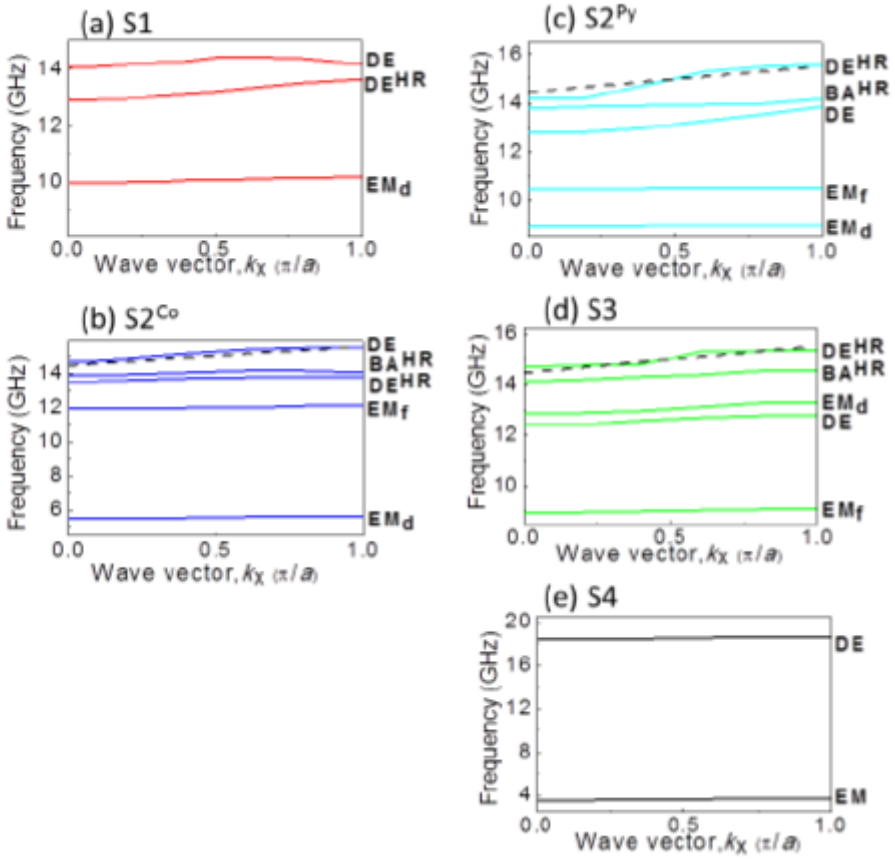

Fig. 4.12. Dispersion relation in the first BZ along the direction perpendicular to the external magnetic field. (a) Dispersion relation of the EM_d, DE and DE^{HR} modes in S1are shown. (b) Dispersion relation in $S2^{Co}$. The additional dispersion relation of the EM_f and BA^{HR} are shown. (c) Dispersion relation of the most relevant modes in $S2^{Py}$. (d) Dispersion relation in S3. (e) Dispersion relation in the array of Co dots (S4). The black dashed lines in Figs. 4.20(b), (c) and (d) mark dispersion relation of DE mode in homogeneous Py film of 10 nm thickness calculated according to Ref. [6,99].

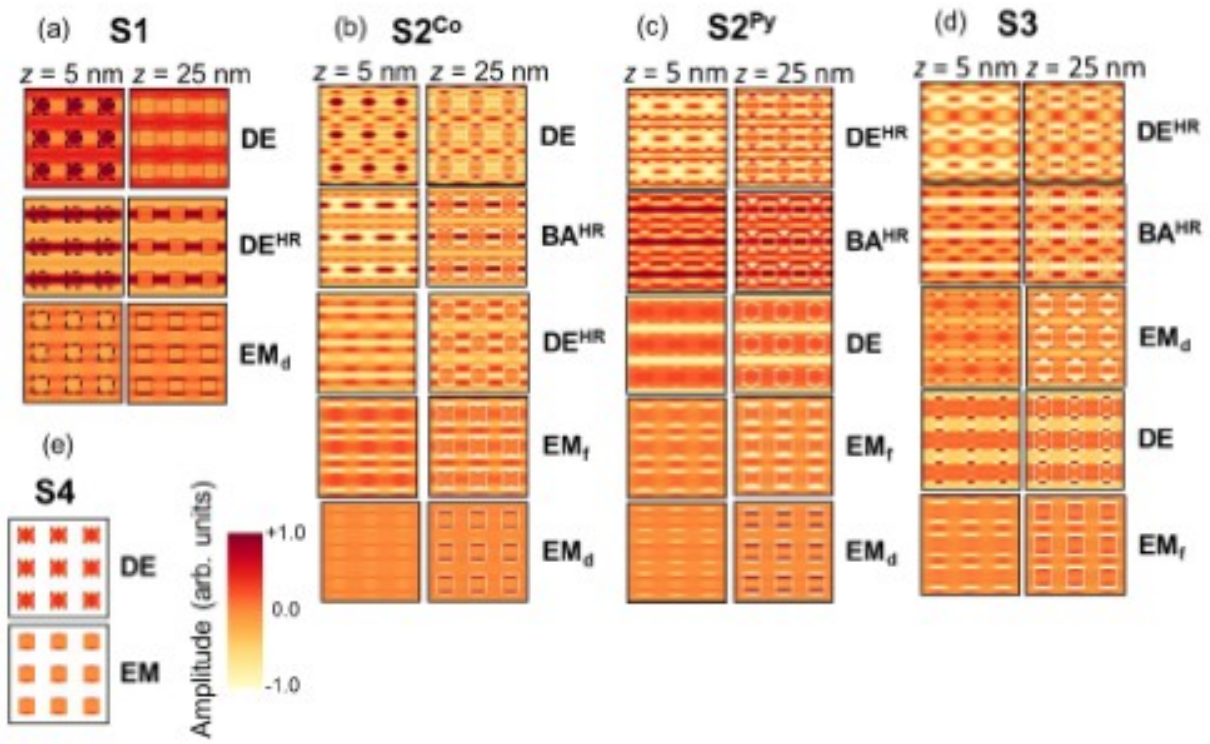

Fig. 4.13. Spatial profiles (real part of the out-of-plane component of the dynamic magnetization vector) for SWs with large differential scattering cross-section calculated in the center of the BZ. The spatial profiles of SW modes from the bottom part of the Py film (in the plane z = 5 nm in left column) and in the plane crossing dots (for z = 25 nm in right column) are shown in 3×3 primitive cells, i.e., on the planes marked in Fig. 4.18 with red dashed lines. (a) Spatial profiles of EM, DE^{HR} and DE modes in S1. (b) Spatial profiles of EM_d, EM_f, DE^{HR}, BA^{HR} and DE modes in $S2^{Co}$. (c) Spatial profiles of EM_d, EM_f, DE, BA^{HR} and DE^{HR} modes in $S2^{Py}$. (d) Spatial profiles of EM_f, DE, EM_d, $BA^{HR}$and DE^{HR} modes in S3. (e) Spatial profiles of EM and DE modes in S4.

Fig. 4.13 displays the spatial profiles of the real part of the out-of-plane component of the dynamic magnetization for the main modes at the center of the BZ of the systems studied. The spatial profiles are presented at planes z = 5 nm and z = 25 nm, left and right column of each panels respectively, along the cross-sections indicated in Fig. 4.18 with red dashed lines. Looking at Fig. 4.13(a), it can be seen that the EM_d is strongly localized at the borders of Co dots and its amplitude decreases at z = 5 nm where only Py is present with respect to z = 25 nm. The presence of the Co dots in S1 induces a strong DE^{HR} amplitude decrease inside the region containing the Co dots: indeed, for z < 10 nm the amplitude of the DE^{HR} mode is uniform in the whole rows, while for 20 nm < z < 30 nm its amplitude decreases in the Co dots region. In contrast, for the EM_d the square Co dots induce an opposite behavior. The amplitude distribution of the DE mode takes contribution from both Co dots and Py matrix through its whole thickness. The DE is also the mode with largest differential scattering cross-section. Its intensity at $k_x = 0$ is three times larger than that of the EM_d or the DE^{HR} mode (see Fig. 4.11). Fig. 4.13(b) displays the spatial profiles of the characteristic SW modes of $S2^{Co}$. The presence of the non-magnetic spacer around the Co dots induces the appearance of the EM_f that is strongly localized at the border of the Py matrix close to the non-magnetic spacer. The amplitude

of this mode is almost uniform along the thickness, while that of the EM_d decreases by decreasing z. The DE^{HR}, BA^{HR} and DE modes have uniform amplitude in the region of Py matrix along the thickness. On the other hand, in the region filled by Co dots their amplitude strongly decreases for $z > 20$ nm.

In Fig. 4.13(c) the spatial profiles of the collective excitations in $S2^{Py}$ are shown. The amplitude variation of the EM_d, DE, BA^{HR} and DE^{HR} modes as a function of z is the same as that in $S2^{Co}$. Moreover, in $S2^{Py}$ the amplitude of EM_f decreases by decreasing z following a trend similar to that of the EM_d. The amplitude of SW modes of S3 are illustrated in Fig. 4.13 (d). Similarly to what occurs in $S2^{Co}$ and $S2^{Py}$, the SW amplitude of the DE mode is almost homogeneous across the thickness of the whole structure and larger in the rows between dots. The DE^{HR} and BA^{HR} modes amplitude is almost uniform along z in the Py matrix but decreases for $z > 20$ nm in the region filled by Py dots. In Fig. 4.13(e) are depicted the spatial profiles of collective modes in S4. In this system there is only Co along z and the amplitudes of EM and DE mode are uniform along the thickness.

4.2.3 Total magnetic field

In order to completely understand the dispersion curves and the spatial profiles of SWs modes of the investigated structures, it is useful to evaluate the in-plane components of the total (effective) magnetic field at different values of z. The total static magnetic field is the sum of the exchange field, the demagnetizing field and the Zeeman field, calculated for each micromagnetic cell by the OOMMF code, and averaged along the x direction for different values of z and y. The behavior of the total magnetic field is strictly related to the orientation of the static magnetization in the magnetic system. In Fig. 4.22 four regions along the thickness are considered: a) 0 nm $\leq z \leq$ 10 nm where only Py is present; b) 10 nm $< z \leq$ 20 nm where there are Py and non-magnetic spacer; c) 20 nm $< z \leq$ 30 nm where in S1 there are Py and Co, in $S2^{Co}$ there are Py, non-magnetic spacer and Co and in $S2^{Py}$ and S3 are present Py and non-magnetic spacer; d) 30 nm $< z \leq$ 40 nm where in S1 and $S2^{Co}$ there is Co, in $S2^{Py}$ is present Py. Looking at Fig. 4.14 it is possible to note the presence of wells or walls in the total magnetic field that are due to the saturation magnetization contrast present at interfaces between two different materials. Moreover, in MCs showing magnetization in-homogeneities across the thickness, the total magnetic field at interfaces between two materials, present for 10 nm $< z <$ 30 nm, influences also collective excitations in the homogeneous part of the structure (for 0 nm $< z <$ 10 nm).

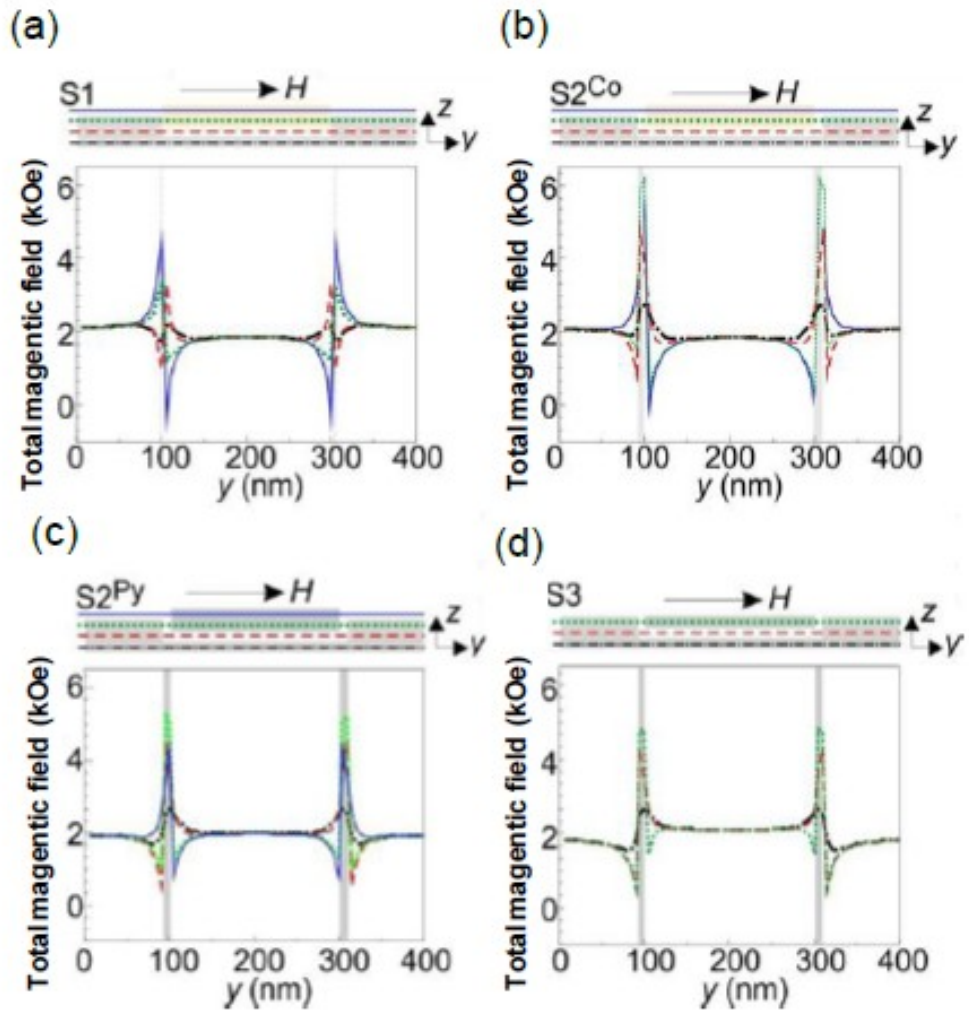

Fig. 4.14. The *y* component of the total magnetic field calculated for (a) S1, (b) $S2^{Co}$, (c) $S2^{Py}$ and (d) S3 along the *y*-axis and averaged along *x*, for four different values of *z*: *z* = 5 nm (in full Py film, black dot-dashed line), *z* = 15 nm (crossing Py and spacer below the dots, red dashed line), *z* = 25 nm (crossing Py matrix and middle of dots, green dotted line) and *z* = 35 nm crossing Co dots (only in S1 and $S2^{Co}$, blue solid line). The gray vertical rectangles mark the non-magnetic spacer which separate the dot from the matrix. The insets on the top show a sketch of MCs with lines along which the total magnetic field is calculated.

The appearance of end modes in MCs is related to the presence of a strong inhomogeneity of the total field resulting in deep wells close to the border of the dots and the matrix. This feature of the total magnetic field in 2D bicomponent MCs depends on two main factors: the shape of the dot and the contrast between the saturation magnetization of the different materials. In particular, the magnetization saturation contrast enhanced by the presence of the non-magnetic spacer leads to the formation of an inhomogeneous demagnetizing field and, as a consequence, to strong in-homogeneities of the total magnetic field at the border between two materials (Co/Py, Co/non-magnetic spacer and Py/non-magnetic spacer). Therefore, the presence of a thin non-magnetic spacer between two ferromagnetic materials not only influences

significantly the SW spectra but can also be an end mode's creating factor. It is important to underline that this important feature, namely the appearance of end modes, either as EM_f or EM_d, does not depend on the dot shape or on the ferromagnetic material for MCs having geometric parameters in the range of the ones typical of the recently studied bicomponent systems. Hence, this picture is different from the one occurring in bicomponent systems[31] where a crucial rule to determine the appearance of end modes was played by a specific combination of the magnetization saturation contrast and the dot shape. As an example, in a bicomponent MC composed of circular Co (Py) dots in direct contact with a Py (Co) matrix, the end mode is present when $|\Delta M_S| = |M_{S,Co} - M_{S,Py}| > 250$ emu/cm^3, but disappears when $|\Delta M_S| = 200$ emu/cm^3. Instead, if the bicomponent system is composed of square Co (Py) dots in direct contact with Py (Co) matrix, an end mode is present when $|\Delta M_S| > 200$ emu/cm^3. In the following, the shape of the total magnetic field in 2D bicomponent MCs introduced by non-magnetic spacers around dots and its relation to the end modes is discussed. Fig. 4.14(a) shows the total magnetic field calculated for S1 vs. y for different values of z. Two deep wells are present inside the region of the Co dot above the Py matrix corresponding to $z > 30$ nm. The two wells are still present for 20 nm $< z <$ 30 nm, although with decreasing depth. The two wells disappear for $z < 20$ nm, however the walls appear in this range. For this reason the EM_d is strongly localized in the well of the total magnetic field at the border of Co dot for $z > 20$ nm and disappears in the homogeneous part of the system where there is the Py matrix ($z < 20$ nm) (see Fig. 4.13(a)).

The Fig. 4.14 (b) shows the calculated total magnetic field for $S2^{Co}$ as a function of y at different values of z. It can be seen that the positions of the minima of the total magnetic field depend on the value of z. In particular, the total magnetic field has its minimum value in the Py region for $z < 20$ nm while in the Co region for $z > 20$ nm. These two wells close to the border between Py and the non-magnetic spacer and the non-magnetic spacer and Co give rise to the two localized modes EM_f and EM_d, respectively. Thus, the presence of these two end modes is strictly related to the non-magnetic material that surrounds the Co dots responsible for the appearance of the two minima in the total magnetic field.

Comparing the profiles of the total field at z =15 nm and z = 25 nm (red dashed and green dotted line in Figs. 4.14(a) and (b)), an increase of the depth of the magnetic wells can be noted in $S2^{Co}$ with respect to the one in S1. This explains the decrease of the frequency of the EM_d in $S2^{Co}$ as compared to the one in S1. Moreover, the wells of the total field corresponding to the region filled by the Py matrix close to the non-magnetic spacer at z =15 nm, although less deep than the ones in the Co dot, are deep enough to permit localization of the EM_f.

By looking at Fig. 4.14(a) it is also possible to understand that the variation of the total magnetic field due to the non-magnetic spacer induces a change of DE^{HR} and DE mode profiles as a function of z. It is possible to observe that the uniform amplitude of DE^{HR} in the horizontal rows (see Fig. 4.13(a)) is due to the trend of the total magnetic field. Indeed, by looking at Fig. 4.14(a) (black dot-dashed line), one can note that the total magnetic field does not present significant in-homogeneities along the y direction at z = 5 nm. Instead, at z = 25 nm the DE^{HR} mode is localized only in the Py region (see Fig. 4.13(a)) and its amplitude vanishes inside

the Co dot. On closer inspection of the corresponding total magnetic field [Fig. 4.14(a) green dotted line] it can be observed the presence of a high wall at the border between Py and Co that prevents the spreading of DE^{HR} inside the Co dot. The DE mode has higher frequency than DE^{HR} and its amplitude spreads also in Co dot for $z > 20$ nm. In $S2^{Co}$, there is an increase of the total magnetic field in-homogeneity as compared to S1 for each value of z, apart from $z > 30$ nm where there is a small reduction (see Figs. 4.14(a) and (b)). This results in an increase of the frequencies of the DE and DE^{HR} modes.

In order to investigate the effect of the change of the material filling the dots the total magnetic field for $S2^{Py}$ has been computed and shown in Fig. 4.14(c). There are two minima of the total magnetic field: the absolute minimum is located in the Py matrix for 10 nm $< z <$ 20 nm and the other minimum is placed in the Py dot for 30 nm $< z <$ 40 nm. In correspondence of the above mentioned minima, also in $S2^{Py}$ there is the appearance of the EM_d and of the EM_f, respectively. By looking at Figs. 4.14(b), (c) and (d), a qualitative similarity of the behavior of the total magnetic field as a function of y in $S2^{Co}$, $S2^{Py}$ and S3, respectively, can be noted. In Fig. 4.14(d), where the Py dot thickness is 10 nm, the magnetic field well in the dot is less deep than the one in $S2^{Py}$, while in the Py matrix it has a significant minimum (green dotted line, $z = 25$ nm). This explains the interchange of the frequencies of the EM_f and EM_d modes found in S3 with respect to the ones in $S2^{Co}$ and $S2^{Py}$. Detailed inspection of the total magnetic field profiles shown in Fig. 4.14 (b), (c) and (d) allows to notice also the relative change of the magnetic field values among $S2^{Co}$, $S2^{Py}$ and S3 in the channels parallel to the x-axis containing dots [i.e., area of the DE^{HR} mode, for 100 nm $< y <$ 300 nm in Fig. 4.14] and lying between the dots [i.e., area of the DE mode for 0 nm $< y <$ 90 nm and 310 nm $< y <$ 400 nm]. In the middle part of these areas the average value of the total magnetic field is almost constant across the full thickness. In $S2^{Co}$ the values of the field are 2.06 and 1.85 kOe in center of the areas of DE and DE^{HR} mode, respectively, while in S3 the respective values are 1.82 and 2.1 kOe. This behavior of the field can explain the frequency exchange of the DE and DE^{HR} modes between $S2^{Co}$, $S2^{Py}$ and S3 in Fig. 4.12 (b), (c) and (d), respectively.

4.2.4 Properties of the dispersion relation

The different position and size of the non-magnetic spacer modify also important features of the propagation of SWs. In order to investigate this effect, the group velocity and the band width for the most relevant modes have been calculated The group velocity is important e.g. in the transmission measurements with the use of coplanar waveguide transducers, where SW with low wave number are usually excited[100]. A wide band width is important in order to accommodate incoming and transmitted signal; moreover, it can be used as an indicator of the interaction strength in the MC. The group velocity (v_g) has been calculated in the DE geometry for selected modes close to the center of the BZ, as:

$$v_g = 2\pi \frac{\Delta \nu}{\Delta k_x}, \tag{4. 8}$$

where $\Delta\nu$ indicates the variation of the SW frequency due to the change of the wave vector along the x-axis and Δk_x is the change of the wave vector. In calculations $\Delta k_x = 0.05\ \pi/a$ because the group velocity is calculated close to the center of the BZ. The band width for selected mode has been calculated as a change of its frequency between BZ center and BZ border

$$\Delta\nu_{bw} = |\nu(k_x = \pi/a) - \nu(k_x = 0)| \tag{4. 9}$$

The group velocity and the band width of the investigated SW excitations (EM_d, EM_f, DE and DE^{HR}) are calculated and collected in Tab. 4.1.

	S1		**S2^{Co}**		**S2^{Py}**		**S3**		**S4**	
	v_g [m/s]	Band width [GHz]	v_g [m/s]	Band width [GHz]	v_g [m/s]	Band width [GHz]	v_g [m/s]	Band width [GHz]	v_g [m/s]	Band width [GHz]
EM_d	64	0.162	48	0.154	0	0.21	48	0.446	40	0.154
DE^{HR}	144	0.750	368	0.272	160	1.378	160	0.668	-	-
DE	256	0.355	522	0.810	256	1.097	152	0.410	68	0.203
EM_f	-	-	80	0.226	48	0.49	48	0.173	-	-

Tab. 4.1. Group velocity v_g in the BZ center and band width for EM_d, EM_f, DE and DE^{HR} modes in the MCs investigated here.

It is possible to see from Tab. 1 that for vanishing wave vector, the DE and DE^{HR} modes in $S2^{Co}$ exhibit the largest group velocities. This is an interesting result since $S2^{Co}$ can be regarded as the most disruptive structure with respect to a homogeneous thin film. This effect can be attributed to a combination of higher contrast between Co and non-magnetic spacer and Py and non-magnetic spacer and to a higher Co gyromagnetic ratio. Moreover, by looking at Tab. 4.1 it is found that the DE^{HR} modes in S1, $S2^{Py}$ and S3 have similar group velocities, while the DE mode of S3 has a group velocity smaller than the ones of the DE modes in S1 and $S2^{Py}$. The decrease of the group velocity in S3 can be due to the thickness reduction of the Py dots. It is interesting to compare these group velocities to that of the DE magnetostatic SW in homogeneous Py film of 10 nm thickness calculated according to Eq. (4.8). In this special case the latter turns out to be 880 m/s, a value larger than the ones of the systems studied as expected. The dispersion relation of the DE magnetostatic SW is superimposed in Figs. 4.12(b), (c) and (d) with black dashed line. It

is possible to observe that it matches very well with the DE mode in $S2^{Co}$ and the DE^{HR} modes in $S2^{Py}$ and S3. This shows that the DE and DE^{HR} modes, in $S2^{Co}$, $S2^{Py}$ and S3 respectively, propagate in a way similar to that of the DE magnetostatic SW in homogeneous Py film and they travel mainly in the lower part of the structure where the dots influence on the internal field is smallest, nevertheless it changes the group velocity and band width.

Comparing the group velocities of DE and DE^{HR} modes of S1, $S2^{Co}$, $S2^{Py}$, S3 and S4 with the one of the DE magnetostatic SW mode in homogeneous Py film, it can be noted that the presence of two different magnetic materials and a non-magnetic spacer reduces the speed of propagation in the BZ center. This is probably due to the presence of different magnetic material and non-magnetic spacer that induce the SW confinement in particular regions of the primitive cell. The DE and DE^{HR} mode of $S2^{Py}$ have the largest band width. It is interesting to note that also the end modes with higher frequency, EM_f and EM_d in $S2^{Co}$ and S3 have a band width comparable to that of the propagative DE^{HR} and DE modes. This means that also the localized modes can propagate in this kind of MCs and their properties can be exploited for transmitting signal.

4.3 Spin wave modes in bicomponent Py/Co structures in the parallel and antiparallel state

4.3.1. Bicomponent elliptical dots

The system is composed of two close elliptical dots of Py and Co with a small gap of 35 nm that separates them. The Scanning Electron Microscopy (SEM) image of the sample, provided by the group of the Professor Adeyeye at the National University of Singapore, is shown in Fig. 4.15. Each elliptical dot has a width of 225 nm, a length of 1000 nm and a thickness of 25 nm. To reproduce the exact shape of the dots, a bitmap image of the basic unit of the bicomponent dots was created from the SEM image of Fig. 4.15, and used as input for the simulations. Periodic boundary conditions have been applied to account for the chain arrangement of the Py/Co dots in the investigated sample. The micromagnetic cells have been chosen to be 5 nm × 5 nm × 25 nm. The magnetization ground-states as well as the hysteresis loops were determined by using the OOMMF[49] software. The magnetic parameters used in the calculations have been theoretically determined on the basis of the BLS data of the frequency dependence of the magnetic modes on the applied magnetic field, furnished by at the Department of Physics and Geology of the University of Perugia. For Py: M_s (Py)= 740 emu/cm^3, A (Py) =1.3×10^{-6} erg/cm, γ(Py)= 1.86×10^7 (Hz/Oe) while for Co: M_s (Co)= 1300 emu/cm^3, A (Co) =3.0×10^{-6} erg/cm, γ(Co) = 1.90×10^7 (Hz/Oe).

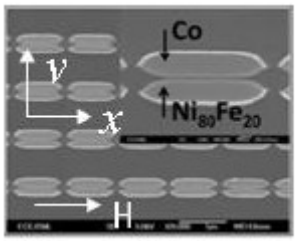

Fig. 4.15. SEM image of the Py/Co elliptical dots obtained by the group of Professor Adeyeye at the National University of Singapore. A reference frame together with the direction of the external magnetic field is also shown.

The dynamical properties of the Py/Co systems have been calculated according to the DMM developed and extended for periodic and multicomponent system by Professor Giovannini at the Ferrara University[28] (see Chapter 2 for further details). The dynamics is studied in the purely conservative regime, hence no damping terms are included in the equations of motion.

The SWs modes are classified by taking into account their spatial profiles. Generally for the Py/Co system it is used the following labels[101]: (a) EM denotes the end modes, i.e. modes localized near the particle edges in the direction of the applied magnetic field, (b) *m*-BA indicates the modes with nodal lines perpendicular to *H* (backward-like modes), and (c) *n*-DE stands for modes with nodal lines parallel to the direction of *H* (Damon–Eshbach-like modes). The fundamental (F) mode without nodal lines corresponds to the Kittel resonant mode in the long wavelength limit. In addition, in this analysis it is found that the eigenmodes exhibit a preferential localization into either the Co or the Py dot. Therefore each mode has been identified with a label containing the localization region (either Py or Co) and the spatial symmetry (EM, F, DE, etc). In spite of the aforementioned preferential localization of each mode in a particular sub-unit, however, the inter-dot dynamic dipolar interaction causes the coupling between the relative phase of the precessional motion in Py and Co dots. For this dot geometry, the coupling via the in-plane dynamic magnetization component δm_y is by far more relevant than that of the out-of-plane component δm_z. Therefore it is possible to observe either an in-phase (acoustic) or an out-of-phase (optical) character of the modes, with respect to the precession of the in-plane magnetization components in adjacent Py and Co dots[54].

4.3.2 Field dependent calculations

The magnetic properties of the Py/Co elliptical dots have been investigated as a function of the external magnetic field. First of all, the hysteresis loop (*M-H* loop) has been calculated by means of OOMMF software and it is shown in Fig. 4.16. The corresponding hysteresis loop measured experimentally with the use of the magneto-optical Kerr effect at the Department of Physics and Geology of the University of

Perugia (not shown in Fig. 4.16) totally confirms the shape and the feature of the simulated one.

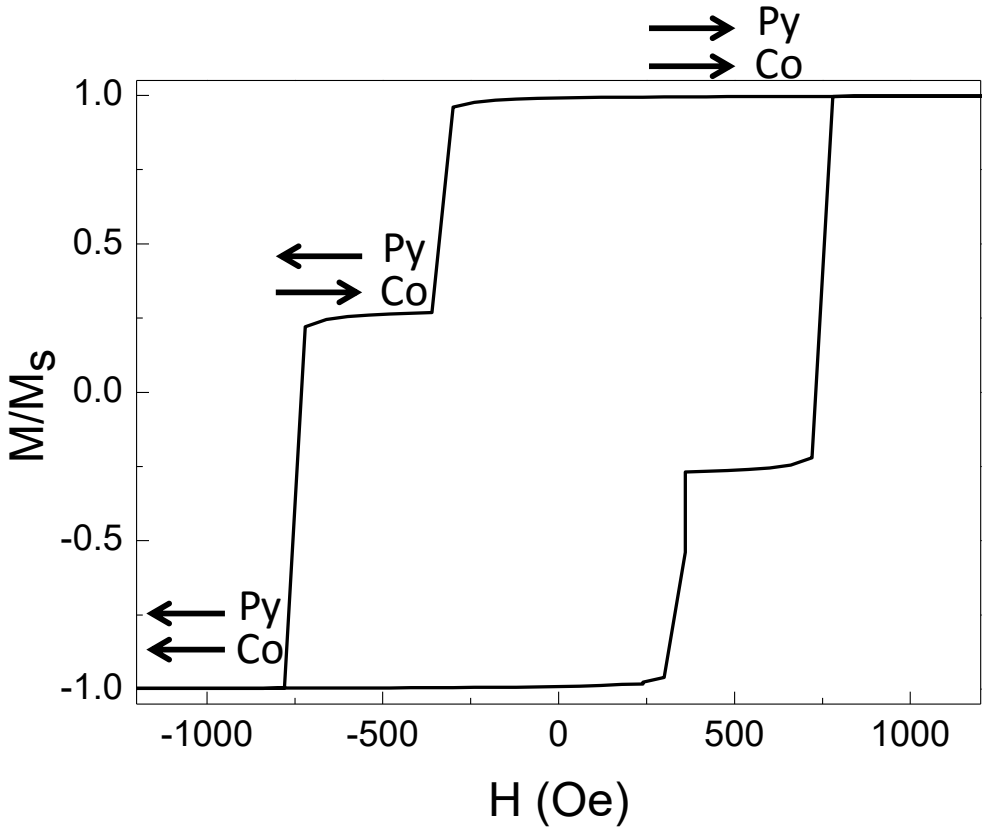

Fig. 4.16. Calculated normalized major hysteresis loop plotted to show the transition fields occurring during the reversal process of the dots. Arrows mark the direction of the magnetization in the Py and Co elliptical dots.

The hysteresis loop displays a two-step switching process due to the distinct magnetization reversal of the Py and Co sub-elements, characterized by a different coercivity. Starting from high external magnetic field, the magnetization of both Py and Co elements have the same direction, indeed in this case the system is in the parallel state. On reversing the applied field, one observes a drop of the magnetization proportional to the Py magnetization fraction within each bicomponent unit associated with the magnetization reversal of the (softer) Py sub-elements. Then a plateau is observed for -370 < H < -730 Oe where the Py and Co magnetizations point in opposite directions, thus realizing the antiparallel ground state of the system. A second jump is seen which corresponds to the reversal of Co sub-elements until about -730 Oe, when the systems is completely saturated in the negative field direction.

Then, the dynamic magnetic properties of the Py/Co elliptical dots have been studied as a function of the external magnetic field[32]. In Fig. 4.17 are shown the frequencies obtained by means of the DMM simulations plotted as a function of the applied field magnitude starting from positive values (dashed lines) together with the BLS data (filled dots) measured at the Department of Physics and Geology of the University of Perugia. The detected modes are identified and labeled on the basis of their calculated spatial profiles, shown in Fig. 4.18 for H= 500 and -500 Oe. They exhibit marked localization into either the Co or the Py dots, as stated at

the end of the previous Section, were it was introduced the labeling notation containing the dominant localization region (either Py or Co) and the spatial symmetry (EM, F, DE, etc).

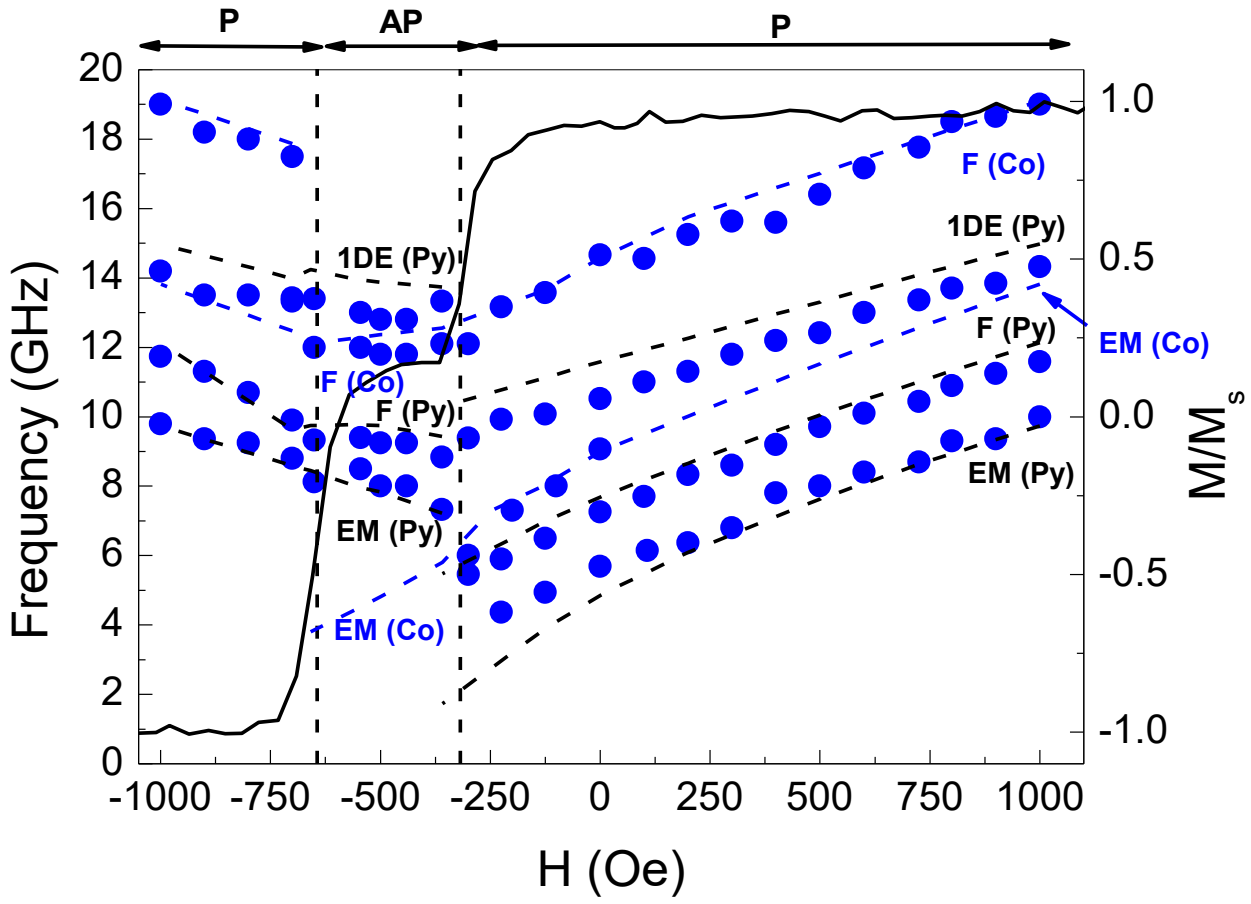

Fig. 4.17. Dependence of the magnetic SWs mode frequency on the applied field strength. Dashed curves indicate the calculated mode frequencies obtained by DMM and the labels indicate the modes nomenclature based on their spatial profiles. Black (blues) curves represent the calculated modes localized into Py (Co) dots. Filled dots are experimental frequencies measured by BLS apparatus at the Department of Physics and Geology of the University of Perugia on sweeping the applied magnetic field from positive to negative saturation (i.e. following the upper branch of the hysteresis loop). The normalized major hysteresis loop is also plotted for showing the transition fields (vertical dashes lines) occurring during the reversal process of the dots. Arrows mark the field regions of the different relative alignment of the magnetization for the Py and Co dots: parallel (P) or anti-parallel (AP).

According to the DMM simulations, when the dots are in the P state, up to five modes exists. On the basis of the calculated spatial profiles (right panel of Fig. 4.18), in the P state the two modes at lowest frequencies as the EM(Py) and the F(Py), with a very small spin precession amplitude into the Co dot are indentified. This is because their frequency is lower than the frequency threshold for this material for the existence of SWs. A similar effect has been observed in periodic array of alternating Py and Co nanostripes[102] and nanodots[103].

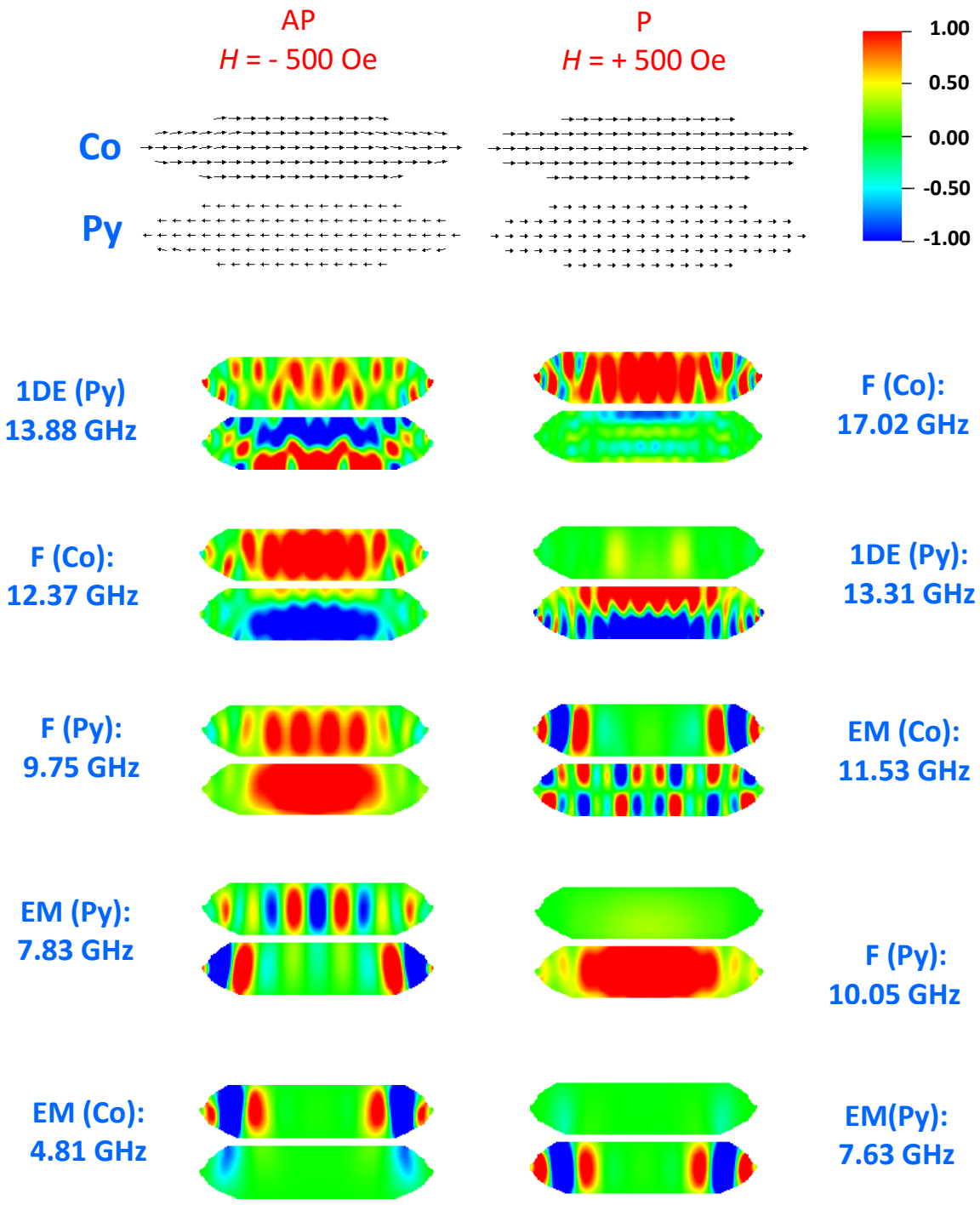

Fig. 4.18. Calculated spatial distribution of the in-plane dynamic magnetization (Im[δm_y], imaginary part) for different modes at the field values indicated on the top of the figure. In the top two lines the magnetization distribution in the top (Co) and bottom (Py) dots, as calculated by the micromagnetic simulations, is also shown, for both the AP and P states.

The F(Py) mode has a spatial profile rather uniform, while the EM(Py) mode exhibits some oscillations with nodal planes perpendicular to the field direction. This particular feature of the EM depends on the arrow-shaped and sharp profile of the edges of our dots and is different from what previously observed in circular, elliptical, or rectangular dots, where the most intense EM has no nodes. At higher frequencies, two modes

with preferential localization into the Co dot are identified, namely the EM(Co) and F(Co) modes. Both of them show an appreciable amplitude also in the adjacent Py dot. Between these two modes, it is present the 1DE(Py) mode which is characterized by one nodal surface parallel to the local magnetization direction. Note that the nodal lines present in the spatial profile of the F(Co) mode perpendicular to the long axis of the ellipse do not correspond to a real change of sign of the dynamic magnetization and are due to the partial hybridization of the F mode with higher-order modes having frequencies close to the one of the F mode. Interestingly, the frequency slope of modes localized into the Co dots is larger than that of Py modes, due to larger values of the Co magnetization and gyromagnetic ratio[104]. An overall good agreement between the calculated (dotted curves) and measured frequency (full points) has been achieved (see Fig. 4.17) even if some discrepancies are observed for the frequency of the EM and 1DE (Py) modes.

A very interesting point is to examine what happens when the external field is reduced and reversed to around H= -300 Oe, where the Py dots reverse and the AP ground state occurs. In correspondence of the AP state, it is possible to observe a discontinuous jump in the frequencies of all the modes localized into the Py dot while the F(Co) mode continues its monotonic evolution. This discontinuity of the Py modes frequency is confirmed by the experimental measurements and the jump marks the P to AP ground state transition. It is noteworthy, in the AP field region, that the Py mode frequencies are characterized by an almost field-independent slope vs H. The corresponding spatial profiles of the modes are shown in the left panels of Fig. 4.18. Here it is possible to see that the only mode which is purely localized in one dot is the EM of Co, because now it is sub-threshold for Py. A further reduction of H, which is sufficient to cause the Co magnetization reversal, produces a P state at negative fields and the frequency starts to increase again as a function of the applied field. In this field range the frequencies of modes in the Py dots monotonously increase in a way similar to that measured in the P state for positive field values while an abrupt change in the frequency of Co modes occurs.

Another interesting analysis is to study the magnetization dynamics at the remanence when the system is in the AP state. In order to reach this configuration it is necessary to stop increasing the negative field to about -300 Oe and come back towards positive applied fields. The DMM calculations can be performed following the minor hysteresis loop. In Fig. 4.19 the mode frequency is shown calculated along the minor loop and compared with values calculated along the major M-H loop (open points).

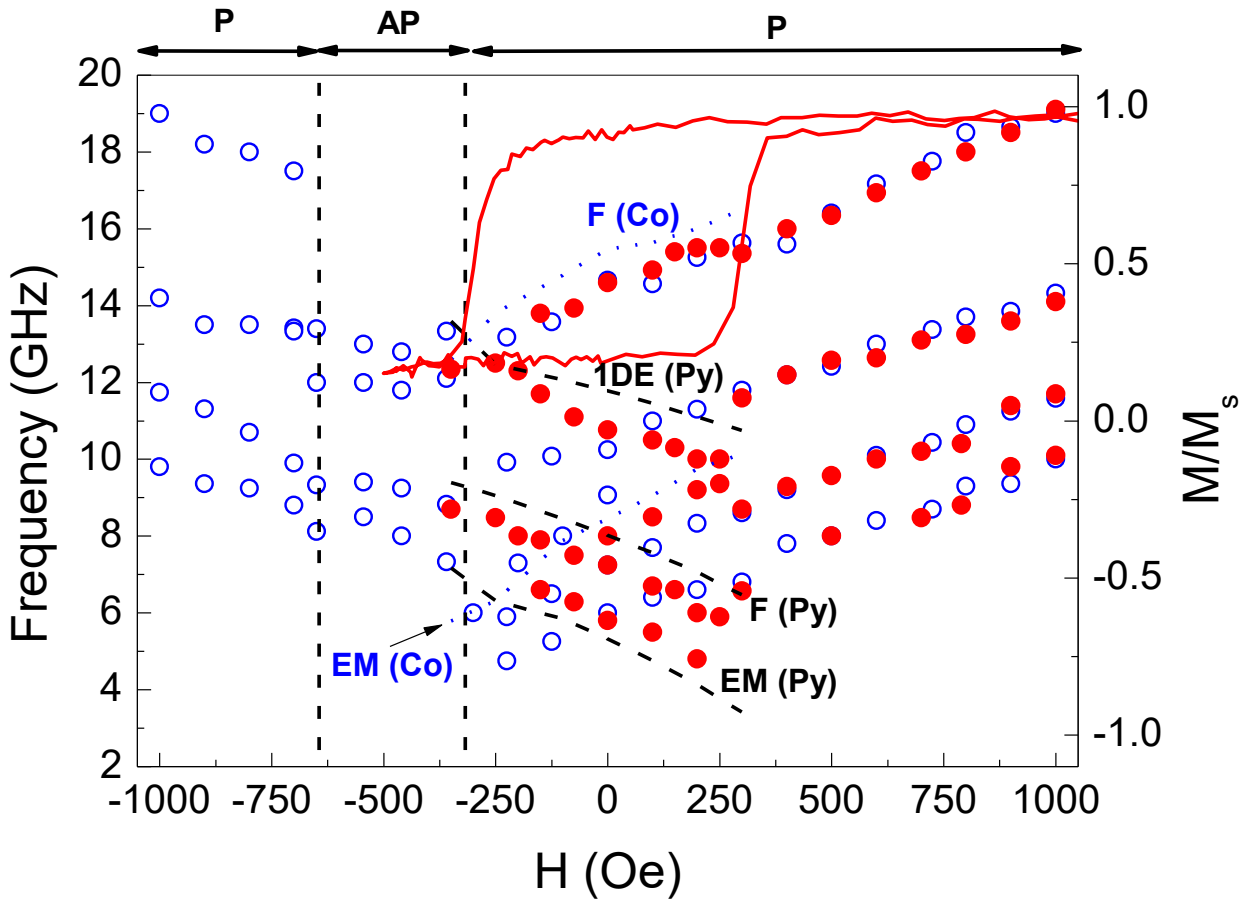

Fig. 4.19. Dashed black and blue curves are frequencies calculated by means of the DMM along the minor hysteresis. Full point are the frequencies measured by BLS apparatus at the Department of Physics and Geology of the University of Perugia along the minor hysteresis (also shown in the figure). The frequencies measured along the major hysteresis loop of Fig. 4.16 are also plotted as open points, for the sake of comparison.

By inspection of the frequency slope of the modes, it is possible to understand the localization of modes into dots of different materials looking at their slope[105]. In particular, three (two) modes have a negative (positive) frequency slope with an almost linear dependence on *H*. It is evident that modes with negative frequency slope are modes localized into the Py dot (EM, F and 1DE) while the two with positive slope are the F(Co) and the EM(Co) modes. This can be easily explained in terms of differences of the internal magnetic field (sum of the Zeeman and magnetostatic fields) inside the dots. Indeed, for the modes localized in the Co dots the applied field is parallel to the magnetization direction, so it is present a positive slope as in the upper branch of the *M-H* loop. In contrast, along the minor *M-H* loop, the applied field (directed in the positive direction) and the Py magnetization are anti-parallel and therefore, it is possible to observe a negative slope for those modes localized into the Py dot, because an increase of the external field corresponds to a decrease of the total internal field. Obviously, when the external field exceeds about +300 Oe, a reversal jump in the minor loops is observed in correspondence with the alignment of the Py dot magnetization with *H*. At this

field an abrupt variation of Py mode frequencies also takes places and the frequencies resume the same values measured along the major *M-H* loop.

4.3.3 Analysis of the dynamic coupling as a function of the gap size

An interesting point which emerges from analysis of Figs. 4.19 and 4.20 is that the frequencies of the eigenmodes are not the same at +500 Oe and at -500 Oe. This is expected for modes localized into the Co element, since the external field is either parallel or antiparallel to their magnetization. However, for those mode localized into the Py sub-element, one could have predicted to find the same frequencies at ±500 Oe, unless the dipolar coupling arising from the adjacent Co dot plays a significant role. In fact, as seen in Figs. 4.19 and 4.20, reversing the field from +500 to – 500 Oe, the frequencies of EM(Py) and 1DE(Py) modes increase by about 0.2 GHz and 0.6 GHz, respectively, while that of F(Py) decreases by 0.25 GHz. The reason of this complex behavior will be addressed in the following, analyzing the interplay of both static and dynamic dipolar coupling between the adjacent Py and Co dots. In Fig. 4.20 the calculated frequencies of the most representative eigenmodes at +500 Oe (FM state) and – 500 Oe (AP state) are plotted as a function of the gap size *d* between the Py and Co sub units (please remind that in the real sample studied here, *d*=35 nm). As a general comment, it can be seen that the frequencies for the system in the AP state are more sensitive to *d* than those of the P state. In particular, the lowest three frequency modes of the AP state (EM(Co), EM(Py) and F(Py)) are downshifted with respect to the case of isolated elements (dotted lines) and show a marked decrease with reducing *d,* while the two modes at higher frequencies (F(Co) and 1DE(Py)) have an opposite behavior even though they exhibit a reduced amplitude. In the P state (right panel), the modes concentrated into the Py dots exhibit a moderate decrease with reducing *d*, while an opposite but less pronounced behavior is exhibited by the F(Co) mode.

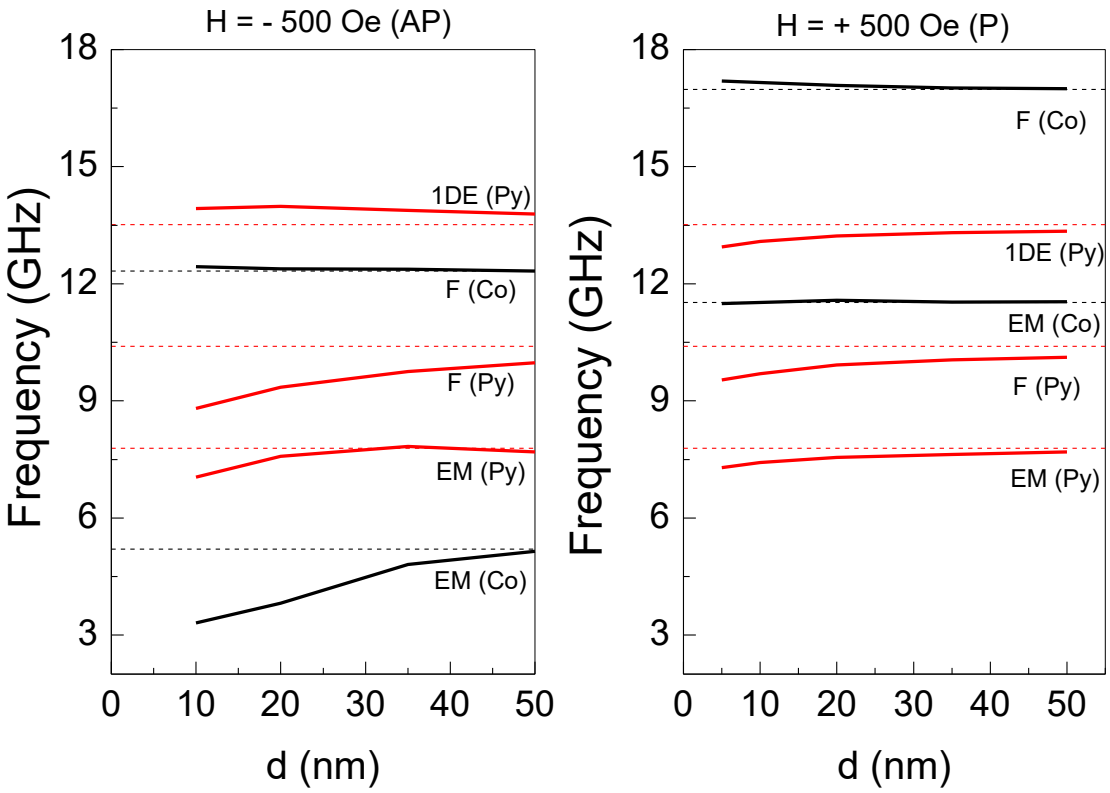

Fig. 4.20. Calculated frequency evolution of modes vs the gap size *d* for two different values of applied magnetic field: (left panel) *H*= - 500 Oe (AP state) and (right panel) *H*= +500 Oe (P state). Red (black) curves represent the calculated frequencies for modes localized into the Py (Co) dots. Horizontal dotted lines shown in the right panel represent the calculated frequency values for non-interacting (isolated) Py and Co dots.

In order to explain the mode frequency behavior both the internal field profiles within the Py and Co dots and the spatial profile of the specific modes should be taken into account. In Fig. 4.21 (a) and (d) are reported the calculated profiles of the inhomogeneous internal fields $H_{\text{int Py}}^{\text{FM}}(x)$ and $H_{\text{int Py}}^{\text{AFM}}(x)$ for Py dot in the P and AP states, respectively, obtained by averaging $H_{\text{int Py}}^{\text{FM}}(x,y)$ and $H_{\text{int Py}}^{\text{AFM}}(x,y)$ over the 45 micromagnetic cells along *y* (all the dots width is considered), for two values of *d*, namely 10 nm and 50 nm. Looking at Fig. 4.21 (a) and (d), one notes that the spatial profile of the internal field does not vary appreciably with *d*. However, due to the static dipolar interaction among the Py and Co dots, for small values of *d* the intensity of the internal field in the central portion of the Py dot is slightly lower (larger) than for isolated dots in the case of the P (AP) configuration. (Instead, the internal field within the Co dot, Fig. 4.21 (g), is almost independent of *d*, given the relatively larger magnetic moment of Co with respect to Py). It is clear that the above modification of the static internal field cannot explain the evolution of mode frequencies reported in Fig. 4.17, neither qualitatively, nor quantitatively. Instead, it has been found that a useful hint about the physical mechanism which is responsible for the frequency evolution shown in Fig. 4.20 comes from a detailed analysis of the spatial profile of the modes.

Moreover, it is possible to see in Fig. 4.20 that the frequency of the F(Py) mode decreases with decreasing *d,* for both the P (*H* = + 500 Oe) and AP (H= -500 Oe) states. First, this behavior can be due to the "acoustic" character of this mode, being in-phase the oscillation of the in-plane components of the dynamic magnetization in the Py and Co dots. Secondly, by comparing the spatial profiles shown in Fig. 4.21 (b)-(c) and (e)-(f), it is possible to note that the spin precession amplitude reduces its localization region with increasing *d*. Indeed, for *d* = 50 nm the F(Py) mode amplitude is concentrated in the center of the Py dot and experiences the maximum value of the internal magnetic field leading to a higher frequency. On the other hand, for *d* = 10 nm the mode amplitude extends in a larger portion of the Py dot and experiences the average of the internal field causing a frequency downshift.

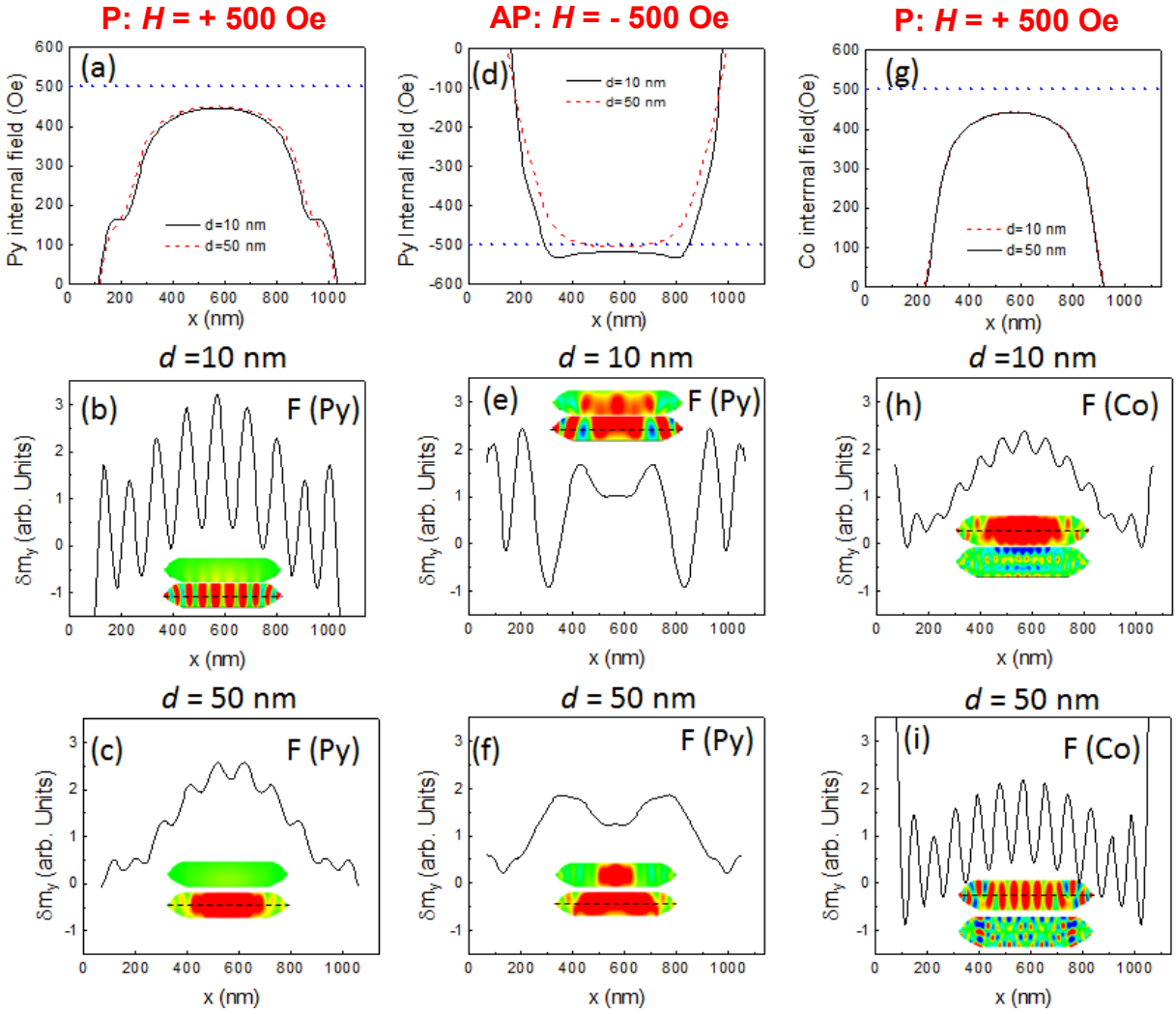

Fig. 4.21. Panels (a) and (d) show the profile of the averaged internal field in the Py dot in the P (*H*= + 500 Oe) and AP (*H*= - 500 Oe) states, respectively at *d* =10 nm (black lines) and *d* = 50 nm (red dashed lines). Panel (g): as in panels (a) and (d), but in the Co dot in the P state. Blue dashed lines in panels (a), (d) and (g) give the magnitude of the external magnetic field. Panels (b) and (e): spatial profiles (Im[δm_y]) of the F(Py) mode in the P and AP ground states, respectively at *d* =10 nm. Panels (c) and (f): corresponding spatial profiles (Im[δm_y]) at *d* =50 nm. Panel (h): spatial profile (Im[δm_y]) of the F(Co) mode in the P state at *d* = 10 nm. Panel (i): as in panel (h), but at *d* = 50 nm. In panels

(b), (c), (e), (f), (h) and (i) are depicted also the spatial profiles in the micromagnetic cells placed in the central line either of Py or Co dot.

Similar considerations can be applied to the case of the frequency trend of the 1DE(Py) mode in the P state, even if the calculated profiles are not shown here. Instead, for the AP state, it can be seen that the 1DE(Py) mode increases its frequency with reducing *d*, because in this case one can recognize an appreciable "optical" character of this mode, with an out-of-phase oscillation of the in-plane dynamic magnetization components (see Fig. 4.18). Concerning the F(Co) mode, it is found that, for both P and AP ground states, the profile of the internal field does not vary appreciably versus *d* (see Fig. 4.21 (g)). Therefore the variation of the spatial profile of this mode (panels (h) and (i) of Fig. 4.21) can be related to the influence of the inter-dot dynamic dipolar coupling. This term gives rise to a perturbation potential affecting the spin precession and inducing a modulation of the spatial profiles in both P and AP states.

4.4 Conclusions

Concluding, in this Chapter the magnetic properties of bicomponent MCs have been investigated. As a general comment, it is important to highlight that the presence of two different ferromagnetic materials strongly modify the spin dynamics in MCs leading to some new magnetic properties with respect to the mono-material MCs investigated in Chapter 3. In particular, the analysis reported in Sect. 4.1 focuses on the band structure of Py/Co MCs. The presence of two different ferromagnetic materials along the thickness of the periodic system allowed us to treat Py/Co MCs as 3D systems albeit with 2D periodicity. It was studied the dependence of band structure on the volume and on the position of Co with respect to the Py film by introducing the notion of effective "surface magnetic charges" resulting from the superposition of the "surface magnetic charges" arising from the static magnetizations of Py and Co. The effective "surface magnetic charges" explain the different orientations of the demagnetizing fields of the two ferromagnetic materials. It was also shown that, when the Co dot is above the Py film, the Co has the physical effect of widening the BGs. A magnetic effective potential was expressed as a function of effective "surface magnetic charges" and the effects of the related demagnetizing field on collective mode dispersion were evaluated by means of micromagnetic simulations. The effect of the interchange of the two ferromagnetic materials on the distribution of the effective "surface magnetic charges" and on the dispersion was also investigated. In addition, in Sect. 4.2 a detailed theoretical investigations of the SWs spectra in 2D bicomponent MCs with the DMM have been performed in order to investigate the influence of a non-magnetic spacer on the magnonic band structure. Five square arrays of square grooves in thin Py film filled (or partially filled) with Co or Py square dots have been studied. The conclusions drawn for these kind of MCs can be generalized to other kind of 2D lattices and of different dot shapes in the nanometric range. The non-magnetic spacer breaks exchange interactions between the magnetic materials of the matrix and the dot. However, most importantly, this non-magnetic spacer strongly modifies the total magnetic field, especially also at the dot edges. Due to these changes of the magnetic field, two types of end modes appear in the same structure.

These are the end mode localized in the dot and that localized in the matrix. Their frequencies strongly depend on the magnetization of the matrix and of the dot material. Moreover, it has been shown that by employing a single material (Py in our case), it is possible to design a MC preserving the main properties of bicomponent MCs and magnonic AD lattices. In addition it has been demonstrated that the introduction of a non-magnetic spacer and the change of the magnetic dot material allow to tailor in different ways the SW spectra in MCs. This includes even the interchange of the SW frequency order. This property can be further exploited for modeling the magnonic band structure and magnonic band gaps towards the properties desired for practical applications. Moreover, the non-magnetic spacer breaks the exchange interaction at the border between the two ferromagnetic materials and allows the fabrication of structures where magnetization reversal of the dots can take place at magnetic field values different from those causing magnetization reversal in the matrix (due to different shape or crystalline magnetic anisotropy). Here, there are more possibilities than in 1D re-programmable structures[94,106] , because the anisotropy axis (and the magnetization) of the dots can be in an oblique direction with respect to the magnetization of the matrix. The results of this study are interesting also for the investigation of the dynamical properties of bicomponent MCs composed of hard and soft ferromagnetic materials, where stray magnetic field originating from the dots (made of hard ferromagnetic material) influences formation of the domain pattern[107] but SW dynamics has not been investigated so far in such structures. Finally, in Sect. 4.3 is presented the theoretical study of the spin eigenmodes in dipolarly coupled bicomponent Co and Py elliptical nanodots. Several eigenmodes have been identified and their frequency evolution as a function of the intensity of the applied magnetic field has been calculated by means of the DMM, encompassing the ground states where the Co and Py dots magnetizations are parallel or anti-parallel, respectively. In correspondence to the transition between the two different ground states, the mode frequency undergoes an abrupt variation and more than that, in the anti-parallel state, the frequency is insensitive to the applied field strength. A detailed micromagnetic investigation of the properties of the eigenmodes as a function of the gap distance between Co and Py elliptical dots has been performed and the consequent variation of the internal field has been calculated. It has been shown that the inter-dot dynamic dipolar coupling plays a crucial by affecting the spin-wave mode frequencies as a function of the gap size and induces a modulation of the corresponding spatial profiles both in Co and Py dots.

Chapter 5

Magnonic crystals: a new class of metamaterials

The research on metamaterials is rapidly grown in the last decade both for their challenging and unusual properties and for their strong impact on the technological field. Several classes of materials have been classified as metamaterials including electromagnetic materials, artificial dielectrics, artificial magnetics, chiral materials, anisotropy and bi-anisotropy materials, etc[108]. The description of metamaterial properties in terms of effective quantities has been topical in most of the above mentioned classes. Recently, a new class of metamaterial belonging to periodic magnetic structures with modulated periodicity called MCs has been introduced by describing their dynamical properties in terms of effective quantities. The effective medium description is used to study both mono-material[31,109] and bicomponent[110] MCs. Even though there are recent works investigating the dynamical properties of 2D AD lattices[30] and of bicomponent MCs, it is not given enough attention to investigate the effective properties of the SW excitations. This Chapter treats the metamaterial properties of mono-material and multi-material MCs. In this way it is possible to include MCs in the field of metamaterials and these magnetic systems can be regarded as a new class of metamaterials.

In Sect. 5.1, the metamaterials properties of a mono-material MCs are discussed. The system studied consists in a 2D AD lattice constituted by a periodic arrangement of circular holes embedded into a ferromagnetic matrix. Other interesting properties of this kind of system has been described in Chapter 3, Sect. 3.2. In analogy with what occurs for the spin dynamics in the in-plane magnetized 2D MCs[110,111], by means of the DMM simulations and analytical calculations, it is possible to give an effective medium description by defining a characteristic wavelength for the relevant mode of the spectrum. This wavelength has the role of an effective wavelength commensurable with the periodicity of the system and linked to the Bloch wavelength and fulfils the condition $d/\lambda_{eff} << 1$ with d the hole diameter. Moreover, also a corresponding

(small) effective wave vector can be defined for each collective mode together with its relation with the corresponding Bloch wave vector. Finally, it is proved that the effective dynamical properties do not depend on the orientation of the external magnetic field, but only on the collective character of the modes and on their scattering process with the holes which act as point defects[111].

The new effective quantities introduced for the case of AD lattices are also extended in order to characterize the SWs modes propagating in the bicomponent MCs presented in the Chapter 4, Sect. 4.1. The recent studies on bicomponent systems deal with modeling of dispersion and opening of band gaps at edges of Brillouin zones (*n*BZs with n =1,2,..) based on micromagnetic or analytical methods, but they do not focus the analysis on effective properties[93]. By contrast, in Section 5.2 some interesting effective properties of a bicomponent ferromagnetic systems composed by cylindrical Co dots etched into a Py film are investigated. The investigation is carried out: a) by using DMM in the case of periodic magnetic systems b) by performing an effective medium approximation in the propagative regime (far from edges of *n*BZs). The effective medium approximation is made by introducing some effective magnetic parameters for describing the spin dynamics within bicomponent systems. In addition, the notions of effective quantities defined in the case of mono-material Mc are extended to 2D periodic bicomponent magnetic systems This is done by defining the effective wavelength and the effective wave vector for all collective modes of the 2D bicomponent magnetic systems having frequencies of a few GHz in the microwave range typical of MCs on the nanometric scale. Interestingly, as found in 2D AD lattices[112], also in 2D periodic bicomponent magnetic systems the effective wavelength and the small effective wave vector, that can be defined for each collective mode in both ferromagnetic materials, are not necessarily equal to the corresponding Bloch wavelength and Bloch wave vector. This means that the presence of a second ferromagnetic material does not alter the effective dynamic description and the found rules characterizing the effective quantities remain valid.

5.1 Two dimensional antidot lattice as a magnonic metamaterial

5.1.1. Antidot lattice: structure

The system considered here is a mono-material MC composed of circular holes embedded into a CoFeB matrix. The geometric and magnetic parameters used in the calculations are the same reported in Sect 3.2 in Chapter 3, viz.: the periodicity is a = 610 nm, thickness of CoFeB film L_{CoFeB} = 41nm, hole diameter d =200 nm, $\gamma/2\pi$ = 2.8 GHz/kOe with γ the gyromagnetic ratio of the electron, $4\pi M_s$ = 16.70kG, M_s the saturation magnetization and exchange stiffness constant $A = 2.75\times10^{-6}$ erg/cm. The value of M_s corresponds to an effective magnetization which includes the effect of the surface anisotropy typical of this ferromagnetic alloy. In the geometry considered here **H** is placed either perpendicularly to the sample plane along the z-axis inducing an out-of-plane rotation of the static magnetization **M,** a parallel to the y directions in order to obtain an in-plane magnetized system, while the in-plane Bloch wave vector ***K*** is kept parallel to the x-axis.

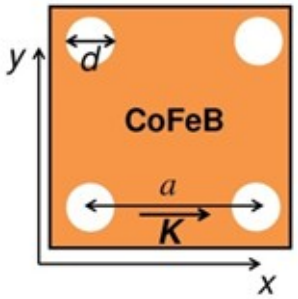

Fig. 5.1. Top view of the sample including the unit cell and the direction of the Bloch wave vector.

The ground-state magnetization is determined by using the OOMMF code[49] with periodic boundary conditions and by subdividing the primitive cell into prismatic cells of 5 nm × 5 nm × 41 nm. Indeed, it is assumed that the most representative collective modes are uniform along z. The ground-state magnetization bends close to the holes due to the magnetization discontinuity between the ferromagnetic material and the holes. The band structures of the RM for the case of the out-plane magnetized system and of the DE mode for the case of the in-plane magnetization, is calculated according to the DMM. The RM and the DE modes have the largest scattering cross-section and become the Fundamental mode for vanishing $\boldsymbol{K}$, that are the resonant modes of the spectrum as for the case out-of-plane and in-plane magnetized MCs.

5.1.2 Effective rules

The spatial profiles of the RM and DE mode calculated at the border of the 3BZ and 4 BZ in the case of out-of-plane and in-plane magnetized system, are shown in Fig. 5.2. By inspection of Fig. 5.2, it is possible to define the effective wavelength λ_{eff} expressed as the distance between two maxima (or two minima) of the wave.

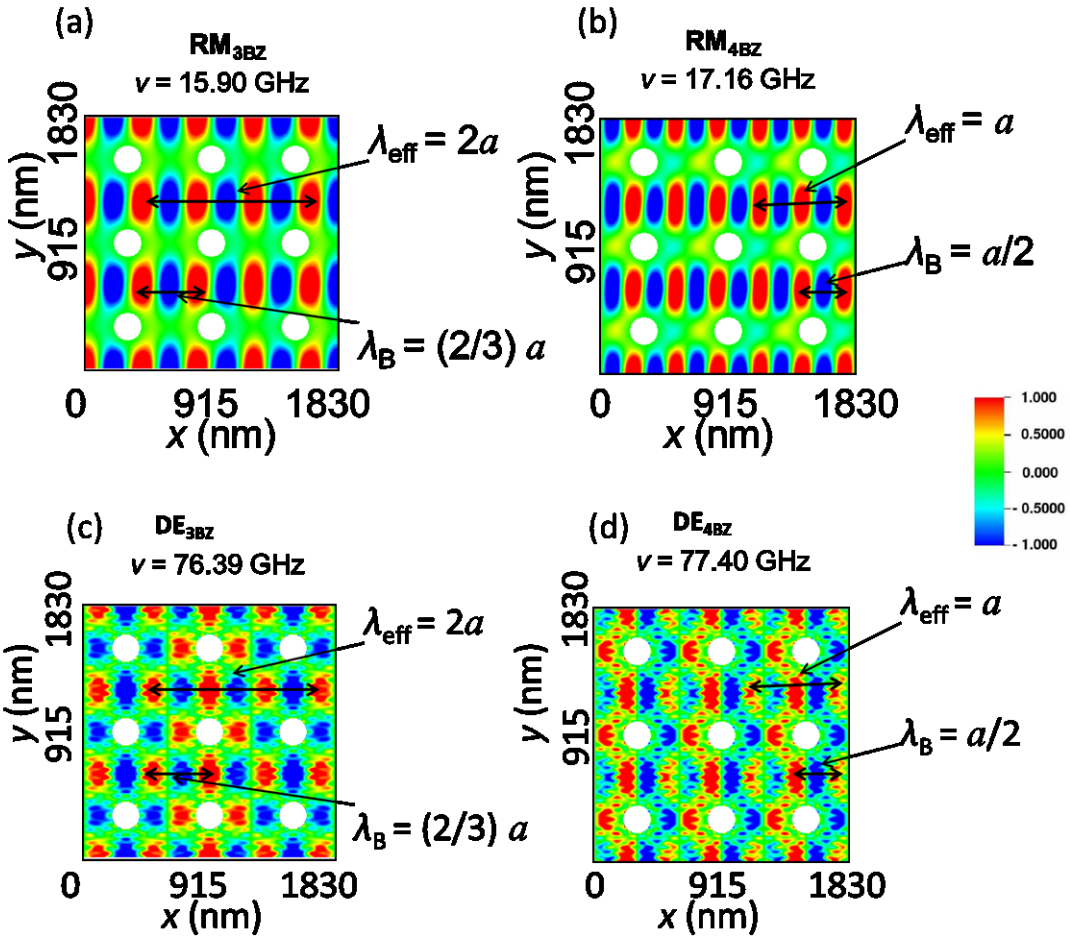

Fig. 5.2. Calculated spatial profiles of SWs modes. (a) Spatial profiles of RM_{3BZ} at the X′ point for the out-of-plane magnetized system. (b) Calculated spatial profiles of the RM_{4BZ} at the Γ″ point . (c) Spatial profiles of DE_{3BZ} at the X′ point for the in-plane magnetized system. (d) Spatial profiles of DE_{4BZ} at the XΓ″ point for the in-plane magnetized system. For all the collective modes the effective wavelength λ_{eff} and the Bloch wavelength λ_B are indicated.

For both the geometries studied, out-of-plane and in-plane magnetized AD lattice, the λ_{eff} is commensurable with the AD lattices periodicity (see Fig. 5.2 (a) and (b) for the case of out-of-plane AD lattice, (c) and (d) in-plane magnetized AD lattice). In particular, for the RM and the DE mode λ_{eff} fulfil the following rule:

$$\lambda_{\text{eff}}^{n\text{BZ}} = \begin{cases} 2a & \text{if } n \text{ is odd} \\ a & \text{if } n \text{ is even} \end{cases} \tag{5.1}$$

In addition it is possible to link λ_{eff} with the Bloch wavelength defined as $\lambda_B = 2\pi/\boldsymbol{K}$ where $\boldsymbol{K}$ is the modulus of the Bloch wave vector:

$$\lambda_{\text{eff}}^{n\text{BZ}} = \begin{cases} n\lambda_{\text{B}}^{n\text{BZ}} \text{ if } n \text{ is odd} \\ \frac{n}{2}\lambda_{\text{B}}^{n\text{BZ}} \text{ if } n \text{ is even} \end{cases} \tag{5.2}$$

The corresponding relation between the (small) effective wave vector $\boldsymbol{k}$ and the Bloch wave vector $\boldsymbol{K}$ is expressed as:

$$\begin{aligned} \boldsymbol{k}^{(2l+1)\text{BZ}} &= \boldsymbol{K}^{(2l+1)\text{BZ}} - \boldsymbol{G} \\ \boldsymbol{k}^{(2l+2)\text{BZ}} &= \boldsymbol{K}^{(2l+2)\text{BZ}} - \boldsymbol{G} \end{aligned} \tag{5.3}$$

where $\boldsymbol{G} = (l\, b^x, 0)$ is a reciprocal lattice vector with $l = 0,1,2,....$ and $b^x = 2\pi/a$. The effective description of collective modes remain valid also in the propagative regime, viz. far from nBZ boundaries.

5.2 Metamaterial properties of bicomponent MCs

5.2.1 Description of the systems and micromagnetic framework

In this Section metamaterial properties of the bicomponent MCs previously introduced in Sect. 4.1 are investigated. The four systems are sketched in Fig. 5.3. The magnetic and geometric parameters used in the calculation are the same defined in Sect. 4.1. The ground-state magnetization is determined by using the OOMMF code with periodic boundary conditions and by subdividing the primitive cell into micromagnetic cells of 7.5 nm × 7.5 nm × 8 nm. The frequencies of the collective modes are determined according to the DMM with implemented two-dimensional boundary conditions[31] . The magnetic systems are studied in the Damon-Eshbach geometry, that is the external magnetic field **H** is applied along the y-direction, while the Bloch wave vector **K** is parallel to the x-direction (see Fig. 5.3, inset of panel (e)). The analysis of collective mode frequency dispersion is carried out along the x-direction at a fixed external magnetic field of intensity $H = 500$ Oe. The ground-state magnetization **M** is almost collinear with **H**.

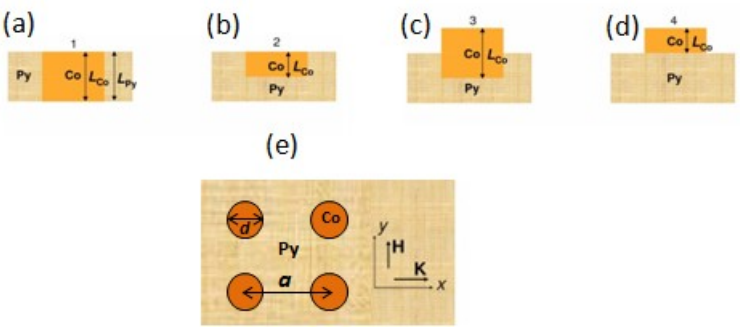

Fig. 5.3. (a) Pictorial sketch of system 1. (b) as in panel (a) but for system 2. (c) as in panel (a) but for system 3. . (d) as in panel (a) but for system 4. The thickness L_{Py} of the Py film and the thickness L_{Co} of the Co cylindrical dots are

indicated . (d) The top view of the four Py/Co bicomponent MCs together with the reference frame and with the directions of **H** and of **K** are also shown.

5.2.2 Effective medium approximation

A very interesting point discuss are the effective properties of the Py/Co bicomponent systems in the propagative regime by means of the effective medium approximation. With this aim, it is useful to define an effective magnetization[113] by means of the η_i ratios expressed above in Eq. 4.1, namely

$$M_{\text{eff}}^{i} = M_{\text{s,Py}}\left(1-\eta_i\right) + M_{\text{s,Co}}\eta_i \tag{5.4}$$

with i = 1,2,3,4. The effective magnetization takes into account the presence of both Py and Co materials and their volumes inside the primitive cell. Moreover, also the effective magnetic field playing the rule of an internal field experienced by the metamaterial (MM) wave and depending on both materials can be expressed according to the effective medium approximation in the form

$$H_{\text{eff}}^{i} = H + < H_{\text{dem}\,i}^{y} >_{\text{Cell}} \tag{5.5}$$

where $< H_{\text{dem}\,i}^{y} >_{\text{Cell}}$ indicates the average of the y-component of the static demagnetizing field over the 80 micromagnetic cells of the primitive cell along both x and y directions calculated by means of OOMMF. Indeed, the results of the calculations shows that the static demagnetizing field is uniform along the thickness for every system. Since the calculated contribution of the exchange field gives a minor contribution to the effective field, this terms is not considered. In principle, it can be useful to define also an effective gyromagnetic ratio γ_{eff} and an effective stiffness constant A_{eff} following the same definition given in Eq. (5.4) for the effective magnetization. By performing a numerical check of these quantities it results $\gamma_{\text{eff}} \approx \gamma_{\text{Py}}$ and $A_{\text{eff}} \approx A_{\text{exch}}^{\text{Py}}$. By means of these approximations it is possible to write the frequency of the MM wave in the propagative regime for the different systems. To describe the dynamics of the MM mode in the propagative regime it is possible to follow the dispersion of the frequency of the Damon-Eshbach surface mode of the thin continuous film in the dipole-exchange regime and in the absence of losses[66]. For this MM the dispersion can be written in the approximated form as follows

$$\nu_{\text{MM}}^{i} = \frac{\gamma_{\text{Py}}}{2\pi}\left[\left(H_{\text{eff}}^{i} + \frac{2A_{\text{exch}}^{\text{Py}}}{M_{\text{eff}}^{i}}q^2 + 4\pi M_{\text{eff}}^{i}\right)\times\left(H_{\text{eff}}^{i} + \frac{2A_{\text{exch}}^{\text{Py}}}{M_{\text{eff}}^{i}}q^2\right) + \left(2\pi M_{\text{eff}}^{i}\right)^2\left(1-e^{-2qL}\right)\right]^{\frac{1}{2}} \tag{5.5}$$

where q indicates the Bloch wave vector and L is the thickness of the system studied. The DE mode of the MM corresponds to the effective medium description of the $\mathrm{DE}_{n\mathrm{BZ}}$ collective modes in the bicomponent MCs, because 1) $\mathrm{DE}_{n\mathrm{BZ}}$ propagating modes have an appreciable amplitude in the whole primitive cell and spread also in the horizontal rows comprised between Co circular dots experiencing an internal field which is very close to the calculated effective field; 2) for the ratios η_i studied, the effective magnetization is close to that of Py which fills the region of the magnetic film in the bicomponent MCs. In Fig. 5.4 (a), (b), (c) and (d) the MM wave dispersions are compared to the $\mathrm{DE}_{n\mathrm{BZ}}$ ones for system 1, 2, 3 and 4, respectively. The $\mathrm{DE}_{n\mathrm{BZ}}$ modes are mainly localized in the Py film, but spread also into the horizontal rows containing Co dots and have nodal planes parallel to the local direction of **M**. Note that, at lower frequency, also collective modes, whose amplitudes are mainly concentrated in the horizontal rows containing Co dots, are found in the calculations. However, these modes are less appealing for giving a full description of metamaterial properties and are not shown in the following.

The frequencies of the MM mode have been calculated according to Eq. (5.5) where the numerical values obtained from micromagnetic simulations are: $H_{\mathrm{eff}}^{1} = 476$ Oe, $M_{\mathrm{eff}}^{1} = 794$ emu/cm^3 for systems 1, $H_{\mathrm{eff}}^{2} = 477$ Oe, $M_{\mathrm{eff}}^{2} = 767$ emu/cm^3 for system 2, $H_{\mathrm{eff}}^{3} = 474$ Oe, $M_{\mathrm{eff}}^{3} = 788$ emu/cm^3 for system 3 and $H_{\mathrm{eff}}^{4} = 475$ Oe, $M_{\mathrm{eff}}^{4} = 763$ emu/cm^3 for system 4. In Fig. 5.4 the magnonic mode frequencies of the $\mathrm{DE}_{n\mathrm{BZ}}$ extended modes with n =1,2,.. the band index calculated as a function of the Bloch wave vector up to the 5BZ are shown for the four systems studied. The effective magnetization values are close to the magnetization saturation of Py because the systems are mainly composed of Py.

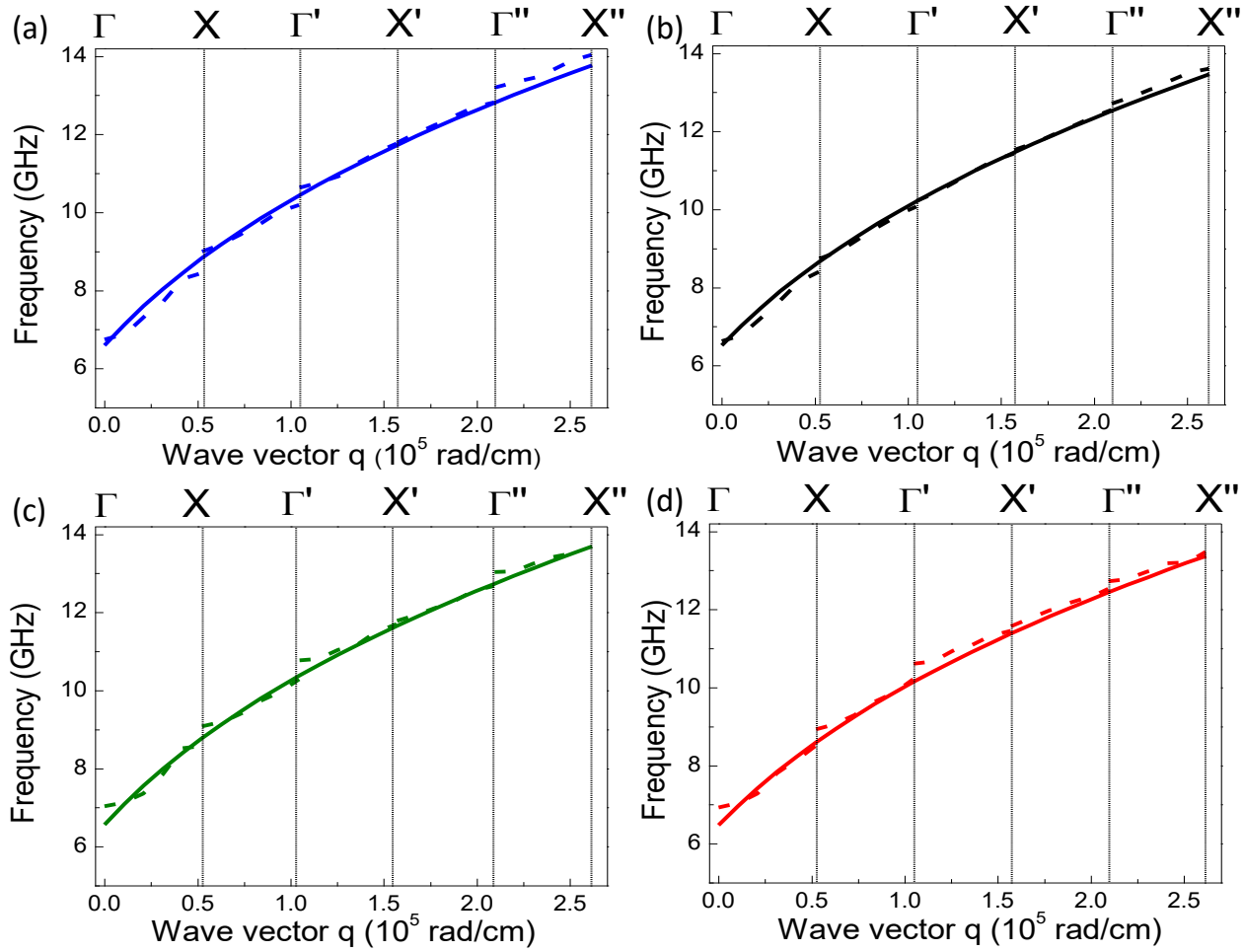

Fig. 5.4. (a) Calculated DMM frequency dispersion of the DE_{nBZ} modes (dashed blue lines) compared to the Damon-Eshbach dispersion of the MM mode (solid blue line) calculated by means of Eq. (5.5) for Py/Co system 1. (b) As in panel (a) but for system 2. (c) As in panel (a) but for system 3. (d) As in panel (a) but for system 4.

For all the systems investigated it is possible to note a very good agreement between the calculated MM waves frequencies and the DMM frequencies of the DE_{nBZ} modes. In particular, the calculated frequencies intersect, at the *n*BZ borders, the middle frequencies of the corresponding BGs determined by means of DMM. In principle, also the MM wave corresponding to the DE_{nBZ}^{HR} dispersion could be determined. However, in this case the calculation of the effective field experienced by the mode would be more complicated, because in performing the average it should be taken into account also the variability of the region of largest amplitude as a function of the Bloch wave vector of the mode itself inside the primitive cell.

Moreover, it is possible to note that at edges of *n*BZs there is the opening of band gaps due to Bragg diffraction, because of the magnetic contrast between Py and Co due to their different saturation magnetizations. Band gap amplitude at the edge of the BZs reduces with increasing band index. Band gap

behavior is similar to the one found for extended modes in a 2D AD lattice[71]. Also band widths follow a similar trend showing a decrease of their amplitudes by increasing band index.

5.2.3 Effective rules

By looking at the spatial profiles of the magnonic modes propagating in this bicomponent MC, it is possible to define an effective wavelength λ_{eff} for each collective mode that corresponds to the distance between two maxima (or two minima) of the wave similar to the case of the 2D AD lattices. In the 2D periodic bicomponent magnetic system the collective excitations are supposed to fulfil the Bloch rule, $\delta\boldsymbol{m}(\boldsymbol{r}+\boldsymbol{R}) = \delta\boldsymbol{m}(\boldsymbol{r})e^{i\boldsymbol{KR}}$ where $\delta\boldsymbol{m}(\boldsymbol{r})$ is the dynamic magnetization, $\boldsymbol{R}$ is the in-plane lattice vector and $\boldsymbol{K}$ is the Bloch wave vector. The effective wavelength is the characteristic wavelength of the collective mode and is directly related to the scattering of collective modes at the interface between the two ferromagnetic materials due to the contrast between the two saturation magnetizations. Instead, the Bloch wavelength λ_B is related to the 2D system periodicity and can be expressed for each collective mode as $\lambda_B = 2\pi/K$ with K the modulus of the Bloch wave vector. In order to show that the value of λ_{eff} is independent of the ferromagnetic materials, in Fig. 5.5 are depicted, as an example, the spatial profiles of two modes at the border of the 3BZ not only for Py/Co system, but also for Co/Py system, namely for the same periodic bicomponent system with interchanged ferromagnetic materials. For both magnetic systems it is possible to give the same definition of λ_{eff}.

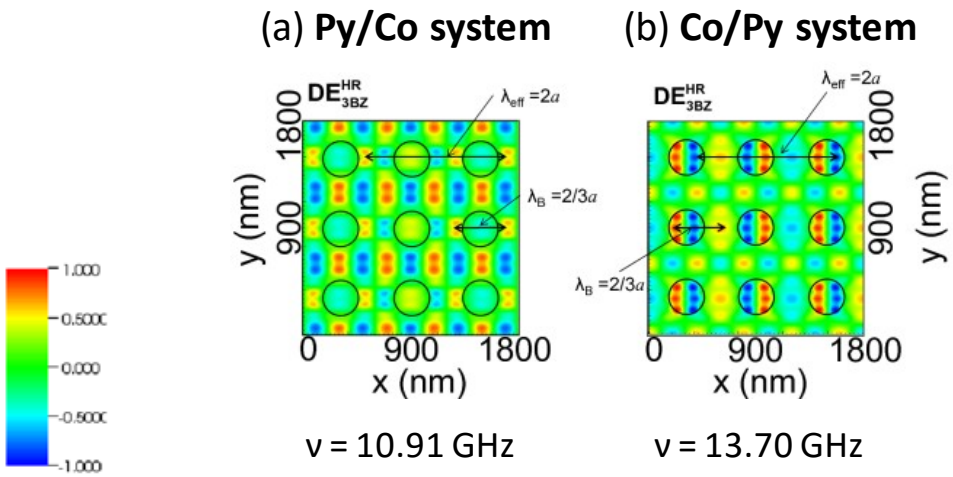

Fig. 5.5. (a) Calculated spatial profiles ($Re[\delta m_z]$, real part of the out-of-plane component of the dynamic magnetization) in 3 × 3 primitive cells of the DE^{HR}_{3BZ} collective mode at the X' point for the Py/Co system . (b) As in panel (a), but for the Co/Py system.

Collective modes shown in Fig. 5.5 (DE^{HR}_{3BZ}) belong to the family of DE^{HR}_{nBZ} localized modes with n =3 and the superscript "HR" refers to their strong localization in the horizontal rows containing the cylindrical dots. For

the DE_{3BZ}^{HR} collective modes shown it is $\lambda_{eff}=2a$ and $\lambda_B=2/3\ a$ as indicated. This means that at the border of the 3BZ the effective wavelength is three times the Bloch wavelength. At a given nBZ border the same value of the effective wavelength characterizes also the other family of collective modes, the extended modes DE_{nBZ} whose amplitudes spread mainly in the horizontal channels comprised between the cylindrical dots. It is also possible to define a corresponding effective wave vector $\boldsymbol{k}_{eff}$ and to establish the following general rules between the effective and the corresponding Bloch quantities:

1) The effective wavelength is a function of the Bloch wavelength, viz.

$$\lambda_{eff}^{nBZ}=\begin{cases} n\lambda_B^{nBZ} \text{ if } n \text{ is odd} \\ \frac{n}{2}\lambda_B^{nBZ} \text{ if } n \text{ is even} \end{cases} \tag{5.6}$$

The effective wavelength is commensurable with the periodicity and assumes either the value $2a$ or a depending on n with n =1,2,...

2) The small effective wave vector can be written in terms of the Bloch wave vector, viz.

$$\boldsymbol{k}_{eff}^{(2l+1)BZ}=\boldsymbol{K}^{(2l+1)BZ}-\boldsymbol{G} \tag{5.7}$$

$$\boldsymbol{k}_{eff}^{(2l+2)BZ}=\boldsymbol{K}^{(2l+2)BZ}-\boldsymbol{G} \tag{5.8}$$

where $\boldsymbol{G}=(l\ b^x,\ 0)$, l= 0,1,2,.... and $b^x=2\pi/a$. The small effective wave vector can be interpreted as a Bloch wave vector shifted by a reciprocal lattice vector $\boldsymbol{G}$, but not necessarily shifted into the 1BZ and assumes either the value $\boldsymbol{k}_{eff}=(\pi/a,0)$ for n odd with n =1,3, …or the value $\boldsymbol{k}_{eff}=(2\pi/a,0)$ for n even with n=2,4,... Hence, this scheme does not correspond to the well-known shift from the extended to the reduced zone scheme where the meaning of the wave vector is always that of a Bloch wave vector differing by a vector $\boldsymbol{G}$ multiple integer of $\boldsymbol{b}$, the primitive reciprocal wave vector. It is interesting to note that, as $d\rightarrow 0$, the effective wavelength becomes equal to the Bloch wavelength and the description of the spin dynamics in terms of effective properties breaks down[8].

5.3 Conclusions

In summary, in Chapter 5 are discussed the metamaterials properties of both mono-materials and multi-materials MCs leading to the introduction of MCs in the field of metamaterials. In particular in Sect. 5.1 it is shown that both perpendicularly magnetized and the in-plane magnetized 2D AD lattices exhibit effective properties. Most importantly, it has been proved that the effective medium description of collective mode dynamics in terms of effective quantities remain valid both for out-of-plane magnetized and the in-plane magnetized 2D MCs. It is thus possible to classify also this type of MCs as magnonic metamaterials

exploiting the higher symmetry related to the perpendicular and in-plane magnetization for technological applications based on propagation of spin-wave modes in AD lattices.

Metamaterial properties of four different bicomponent MCs consisting of Co cylindrical dots etched into a Py film have been investigated in Section 5.2. Here, it was found that the most relevant collective modes dispersions exhibit band gaps at the edges of *n*BZs. Interestingly, in the propagative regime, thanks to the definition of some effective magnetic parameters, a quantitative description of the metamaterial wave dispersions for all the systems analyzed is given. Because of the dependence on the effective field, the calculated dispersions of the metamaterial waves could be useful for measuring the internal field experienced by magnonic modes in order to control spin-wave propagation in bicomponent periodic systems. In addition the metamaterial properties of bicomponent MCs have been investigated by defining effective quantities that characterize collective modes. Simple relations between the effective wavelength and the effective wave vector and the corresponding Bloch quantities for each collective mode have been obtained. These properties are valid not only for the Py/Co system, but also for the Co/Py system and can be extended also to bicomponent MCs composed by other ferromagnetic materials.

Conclusions

In this Thesis the magnetic properties of periodic magnetic nanostructures have been studied in order to propose these systems as prototypes of new technologies and to increase the basic physics knowledge in the field of the nanomagnetism and magnonics. Results of different investigations are carefully commented and, in the case of available experimental data, critically compared with them.

The study of collective excitations in four different arrays of ADs performed as a function of the external magnetic field have demonstrated the presence of soft modes in two-dimensional periodic magnetic nanostructures. Moreover, thanks to this analysis, it has been possible to completely understand the physical mechanism at the basis of the softening: this phenomena is strictly related to the re-orientational phase transition of the static magnetization from the hard to the easy axis caused by the decrease of the external magnetic field. Another interesting point highlighted in this study consisted in the dependence of the critical field on the system geometry. In addition, the frequency of the SW modes is also examined as a function of the aspect ratio for all the systems. The micromagnetic results are totally confirmed by the BLS experimental measurements.

In order to investigate the effect of the ground-state magnetization on the collective excitations, the magnetic properties of an array of ADs, first with in-plane magnetization and, secondly, with out-of-plane magnetization, have been analyzed. The calculations showed the presence of different types of SWs modes in the two different static configuration. It has been also found the presence of band gaps at the border of the Brillouin zone for both the static configuration and, interestingly, the band gap amplitude does not depend on the ground-state magnetization.

Moreover, the magnetic properties have been studied in multi-material MCs. Four different MCs composed of Co circular dots embedded into a Py matrix have been investigated to understand the effect of the position and of the volume of the Co dots in the primitive cell. Frequency band structures have been calculated and thanks to the introduction of the effective “surface magnetic charges” the feature of the dispersion curves and the different orientations of the demagnetizing fields in the two ferromagnetic materials were explained. In

addition, the effect of the interchange of the two ferromagnetic materials on the distribution of the effective "surface magnetic charges" and on the dispersion has been investigated.

An exhaustive theoretical investigation of the SWs spectra in two-dimensional bicomponent magnonic has been performed in order to study the influence of a non-magnetic spacer on the magnonic band structure. Five square arrays of square grooves in thin Py film filled (or partially filled) with Co or Py square dots were analyzed. The non-magnetic spacer strongly modifies the total magnetic field, especially at the dot edges, leading to the generation of up to two types of end modes in the same structure. These are the end mode localized in the dot and that localized in the matrix. In addition, it has been demonstrated that the introduction of a non-magnetic spacer and the change of the magnetic dot material allow to tailor in different ways the SW spectra in MCs.

Furthermore, an array of bicomponent structures consisting of closely-spaced Py/Co elliptical dots has been analyzed in both the parallel and anti-parallel ground state. Several eigenmodes were identified and their frequency evolution has been calculated as a function of the intensity of the applied magnetic field encompassing the ground states where the Co and Py dots magnetizations are parallel or anti-parallel, respectively. In addition, a detailed micromagnetic investigation of the properties of the eigenmodes as a function of the gap distance between Co and Py elliptical dots has been performed and the consequent variation of the internal field has been evaluated.

Finally, the metamaterials properties of two-dimensional MCs were investigated. By means of the introduction of some effective quantities, the effective properties of the MCs have been studied. In this way it is possible to treat magnonic crystals as a new class of metamaterials.

References

[1] *Nanomagnetism : ultrathin films, multilayers and patterned media*, I. Mills, D.L. II. Bland, J.A.C. (J. Antony C.) (1958).

[2] M. N. Baibich, J.M. Broto, A. Fert, F.N. Vandau, F. Petroff, P. Eitenne, G. Creuzet, A. Friederich and J. Chazelas, Phys. Rev. Lett. **61,** 2472 (1988).

[3] G. Binasch, P. Grunberg, F. Saurenbach and W. Zinn, Phys. Rev. B **39,** 4828 (1989).

[4] P. F. Carcia, A.D. Meinhaldt and A. Suna, Appl. Phys. Lett.**47,** 178 (1985).

[5] P. F. Carcia, J. Appl. Phys. **63,** 5066 (1988).

[6] *Spin Waves: Theory and Applications*, Daniel D. Stancil, Anil Prabhakar Springer Science & Business Media, (2009).

[7] J. H. E. Griffiths, *Nature* **158,** 670 (1946).

[8] P. A. Fleury, S.P.S. Porto, L. E. Cheesman and H.J. Guggenheim, Phys. Rev. Lett. **17,** 84 (1966).

[9] M. Krawczyk and H. Puszkarski, Acta Phys. Polon. A **93**, 805(1998).

[10] M. Krawczyk and H. Puszkarski, Phys. Rev. B **77**, 054437(2008).

[11] S. A. Nikitov, P. Tailhades, and C. S. Tsai, J. Magn. Magn.Mater. **236**, 320 (2001).

[12] *SpinDynamics in Confined Structures I–III* (Berlin: Springer) B. Hillebrands and A. Thiaville (ed. 2001–2006).

[13] G. Gubbiotti, S. Tacchi, G. Carlotti, N. Singh, S. Goolaup, A. O. Adeyeye and M. Kostylev, Appl. Phys. Lett. **90,** 092503 (2007).

[14] C. Elachi, IEEE Trans. Magn. **MAG-11,** 36 (1975).

[15] M. Mruczkiewicz, M. Krawczyk, R. V. Mikhaylovskiy, and V. V. Kruglyak, Phys. Rev. B **86**, 024425 (2012).

[16] D. Kumar, J. W. Kłos, M. Krawczyk, and A. Barman, J. Appl.Phys. **115**, 043917 (2014).

[17] Y. Au, E. Ahmad, O. Dmytriiev, M. Dvornik, T. Davison,and V. V. Kruglyak, Appl. Phys. Lett. **100**, 182404(2012).

[18] H. Yu, G. Duerr, R. Huber, M. Bahr, T. Schwarze, F. Brandl,and D. Grundler, Nat. Commun. **4**, 2702 (2013).

[19] K. S. Lee, D. S. Han, and S. K. Kim, Phys. Rev. Lett. **102**,127202 (2009).

[20] A. Chumak, A. A. Serga, and B. Hillebrands, Nat. Commun. **5**,4700 (2014).

[21] M. Krawczyk and D. Grundler, J. Phys.: Condens. Matter **26**,123202 (2014).

[22] B. Lenk, H. Ulrichs, F. Garbs, and M. M¨unzenberg, Phys. Rep.**507**, 107 (2011).

[23] A. Khitun, M. Bao, and K. L.Wang, J. Phys. D: Appl. Phys. **43**,264005 (2010).

[24] F. Montoncello and L. Giovannini, Appl. Phys. Lett. **100**, 182406 (2012).

[25] R. Mandal, P. Laha, K. Das, S. Saha, S. Barman, A. K. Raychaudhuri, and A. Barman, Appl. Phys. Lett. **103**, 262410 (2013).

[26] A. Vogel, M. Hänze, A. Drews, and G. Meier, Phys. Rev. B **89**, 104403 (2014).

[27] B. K. Mahato, B. Rana, R. Mandal, D. Kumar, S. Barman, Y. Fukuma, Y. Otani, and A. Barman, Appl. Phys. Lett. **102**, 192402 (2013).

[28] L. Giovannini, F. Montoncello, and F. Nizzoli, Phys. Rev. B **75**, 024416 (2007).

[29] R. Zivieri, P. Malagò, L. Giovannini, S. Tacchi,G. Gubbiotti and A. O. Adeyeye, J. Phys.: Condens. Matter **25,** 336002 (2013).

[30] R. Zivieri, Solid State Phys. **63**, 151 (2012).

[31] R. Zivieri, P. Malagò, and L. Giovannini, Photon. Nanostruct.: Fundam. Appl. **12**, 398 (2014).

[32] G. Gubbiotti, P. Malagò, S. Fin, S. Tacchi, L. Giovannini, D. Bisero, M. Madami, G. Carlotti, J. Ding, A. O. Adeyeye, and R. Zivieri, Phys. Rev. B **90**, 024419 (2014).

[33] P. Malagò, L. Giovannini, R. Zivieri, P. Gruszecki, and M. Krawczyk, Phys. Rev. B **92**, 064416 (2015).

[34] P. Malagò, L. Giovannini and R. Zivieri, "Perpendicularly Magnetized Antidot Lattice as a Two-Dimensional Magnonic Metamaterial", in Proceedings of the 9th International Congress on Advanced Electromagnetic Materials in Microwaves and Optics pp. 535-537 – Metamaterials 2015, Oxford, United Kingdom, 7-12 September (2015).

[35] P. Malagò, L. Giovannini and R. Zivieri, "Effective properties of a binary magnonic crystal", in Proceedings of the 8th International Congress on Advanced Electromagnetic Materials in Microwaves and Optics pp. 316-318– Metamaterials 2014, Copenaghen, Denmark, 25-30 August (2014).

[36] A.P. Guimares, *Principles of nanomagnetism*, XII, 224p., Springer, (2009).

[37] M. N. Baibich, J. M. Broto, A. Fert, F. Nguyen Van Dau, F. Petroff, P. Etienne, G. Creuzet, A. Friederich, J. Chazelas, Phys. Rev. Lett. **61**, 2472 (1988).

[38] S. S. P. Parkin, N. More, K. P. Roche, Phys. Rev. Lett. **64**, 2304 (1990).

[39] J. G. Gay, R. Richter, Phys. Rev. Lett. **56**, 2728 (1986).

[40] B. T. Jonker, K-HWalker, E. Kisker, G. A. Prinz, C. Carbone, Phys. Rev. Lett. **57**, 142 (1986).

[41] I. Mills, D.L. II. Bland, J.A.C. (J. Antony C.), *Nanomagnetism : ultrathin films, multilayers and patterned media*, 538.3 (1958).

[42] U. Gradmann, Appl. Phys. **3**, 161 (1974).

[43] E.R. Moog, C. Liu, S.D. Bader and J. Zak, Phys. Rev. B **39**, 6949 (1989).

[44] J. Zak, E.R. Moog, C. Liu and S.D. Bader, Phys. Rev. B **43**, 6423 (1991).

[45] C. Kittel, Phys. Rev. **73**, 155 (1948).

[46] C. Kittel, *Introduction to Solid State Physics* (John Wiley & Sons, Inc., New York), p.488., 7th Edition, (1996).

[47] J. Jorzick, S. O. Demokritov, C. Mathieu, B. Hillebrands, B. Bartenlian, C. Chappert, F. Rousseaux, and A. N. Slavin, Phys. Rev. B **60**, 15194 (1999).

[48] G. Duerr, M. Madami, S. Neusser, S. Tacchi, G. Gubbiotti, G. Carlotti, and D. Grundler, Appl. Phys. Lett. **99**, 202502 (2011).

[49] OOMMF User's Guide, Version 1.0, edited by M. Donahue and D. Porter; interagency report NISTIR 6376, National Institute of Standards and Technology, Gaithersburg, MD, http://math.nist.gov/oommf.

[50] D.V. Berkov, K.Ramstöck, A.Hubert, Phys. Stat. Sol (a) **137**, pp.207-225 (1993).

[51] S. Neusser and D. Grundler , Adv. Mater. **21**, 2927-2932 (2009).

[52]A.V. Chumak, P. Pirro, A.A. Serga, M.P. Kostylev, R.L. Stamps, H. Schultheiss, K. Vogt, S.J. Hermsdoerfer, B. Laegel, P.A. Beck, and B. Hillebrands, Appl. Phys. Lett. **95**, 262508 (2009).

[53] S. Tacchi, F. Montoncello, M. Madami, G. Gubbiotti, G. Carlotti, L. Giovannini, R. Zivieri, F. Nizzoli, S. Jain, A. O. Adeyeye and N. Singh, Phys. Rev. Lett. **107**, 127204 (2011).

[54] V. V. Kruglyak, P. S. Keatley, A. Neudert, R. J. Hicken, J. R. Childress, and J. A. Katine, Phys. Rev. Lett. **104**, 027201 (2010).

[55] W. E. Kock, Bell. Sys. Tech. Jour.**34**, 828 (1946).

[56] W. E. Kock, Bell. Sys. Tech. Jour. **27**, 58 (1948).

[57] V. G. Veselago, Soviet Physics Uspekhi **10**, 509 (1968).

[58] D. R. Smith, W.J. Padilla, D.C. Vier, S.C. Nemat-Nasser, S. Schultz, Phys. Rev. Lett. **84**, 4184 (2000).

[59] E. Yablonovich, Phys. Rev. Lett. **58**, 2059 (1987).

[60] W. L. Barnes, A. Dereux, and T.W. Ebbesen, Nature **424**, 824 (2003).

[61] L. M. Brekhovskikh and O.A. Godin, *Acoustics of Layered Media I: Plane and Quasi-Plane waves* (Springer-Verlag, Berlin), (1990).

[62] S. A. Nikitov, P. Tailhades, and C.S. Tsai, J. Magn. Magn. Mater. **236**, 320, (2001).

[63] G. Carlotti and G. Gubbiotti, La Rivista del Nuovo Cimento **22**, 1 (1999).

[64] Jacques E. Miltat, Michael J. Donahue "*Numerical Micromagnetics: Finite Difference Methods*", (2007)

[65] R.W. Damon, J.R. Eshbach, J. Phys. Chem. Solids **19,** 308–320 (1961).

[66] V. V. Kruglyak, S. O. Demokritov, and D. Grundler, J. Phys. D: Appl. Phys. **43,** 264001 (2010).

[67] R. Zivieri, F. Montoncello, L. Giovannini, F. Nizzoli, S. Tacchi, M. Madami, G. Gubbiotti, G. Carlotti, and A. O. Adeyeye, Phys. Rev. B **83**, 054431 (2011).

[68] J. Jorzick, S. O. Demokritov, B. Hillebrands,M. Bailleul, C. Fermon, K.Y. Guslienko, A. N. Slavin, D.V. Berkov and N. L. Gorn, Phys. Rev. Lett. **88**, 047204 (2002).

[69] S. L. Vysotskiĭ, S.A. Nikitov, and Yu. A. Filimonov, J. Exp. Theor. Phys. **101**, 547 (2005).

[70] R. Zivieri, S. Tacchi, F. Montoncello, L. Giovannini, F. Nizzoli, M. Madami, G. Gubbiotti, G. Carlotti, S. Neusser, G. Duerr, and D. Grundler, Phys. Rev. B **85**, 012403 (2012).

[71] S. Neusser, G. Duerr, H. G. Bauer, S. Tacchi, M. Madami, G. Woltersdorf, G. Gubbiotti, C. H. Back, and D. Grundler, Phys. Rev. Lett. **105**, 067208 (2010).

[72] H. Ulrichs, B. Lenk, and M. M¨unzenberg, Appl. Phys. Lett. **97**, 092506 (2010).

[73] W. Wang, J. Sun and S. Li, Appl. Phys. Lett. **99,** 082504 (2011).

[74] D. A. Tenne, M. A. Clark, A. R. James, K. Chen and X. X. Xi, Appl. Phys. Lett. **79,** 3836 (2001).

[75] F. Weber, S. Rosenkranz, J-P. Castellan, R. Osborn, G. Karapetrov, R. Hott, R. Heid, K-P. Bohnen and A. Alatas, Phys. Rev. Lett. **107,** 266401 (2011).

[76] R. W. Wang and D. L. Mills, Phys. Rev. B **50,** 3931 (1994).

[77] R. Zivieri, L. Giovannini and F. Nizzoli, Phys. Rev. B **62,** 14950 (2000).

[78] F. Montoncello, L. Giovannini, F. Nizzoli, P. Vavassori, M. Grimsditch, T. Ono, G. Gubbiotti, S. Tacchi and G. Carlotti, Phys. Rev. B **76,** 024426 (2007).

[79] S. Neusser, G. Duerr, S. Tacchi, M. Madami, M.L. Sokolovskyy, G. Gubbiotti, M. Krawczyk and D. Grundler, Phys. Rev. B **84,** 094454 (2011).

[80] J. Ding, D. Tripathy and A.O. Adeyeye, J. Appl. Phys. **109,** 07D304 (2011).

[81] S. Tacchi, M. Madami, G. Gubbiotti, G. Carlotti , A.O. Adeyeye, S. Neusser, B. Botters and D. Grundler, IEEE Trans. on Magnetics **46,** 172 (2010).

[82] T. Schwarze, R. Huber, G. Duerr, and D. Grundler, Phys. Rev. B **85**, 134448 (2012).

[83] F. Montoncello, L. Giovannini, F. Nizzoli, H. Tanigawa, T. Ono, G. Gubbiotti, M. Madami , S. Tacchi and G. Carlotti, Phys. Rev. B **78,** 104421 (2008).

[84] C.C. Wang, A.O. Adeyeye and N. Singh, Nanotechnology **17,** 1629 (2006).

[85] R. D. McMichael and B. B. Maranville, Phys. Rev. B **74**, 024424 (2006).

[86] J.R. Dutcher, B. Heinrich, J.F. Cochran, D.A. Steigerwald and W.F. Egelhoff, J. Appl. Phys. **63,** 3464 (1988).

[87] J. O. Vasseur, L. Dobrzynski, B. Djafari-Rouhani, H. Puszkarski, Phys. Rev. B **54,** 1043-1049 (1996).

[88] A.V. Chumak, T. Neumann, A.A. Serga, B. Hillebrands, M.P. Kostylev, J. Phys. D: Appl. **42,** 205005 (2009).

[89] Z. K. Wang, V.L. Zhang, H.S. Lim, S.C. Ng, M.H. Kuok, S. Jain, A.O. Adeyeye, ACS Nano **4,** 643-648 (2010).

[90] F. S. Ma, H.S. Lim, V.L. Zhang, Z.K. Wang, S.N. Piramanayagam , S.C. Ng, M.H. Kuok, J. Appl. Phys **111,** 064326(2012).

[91] S. Saha, S.J. Barman Ding, A.O. Adeyeye, A. Barman, Appl. Phys. Lett. **102,** 242409 (2013).

[92] S. Tacchi, G. Duerr, J.W. Klos, M. Madami, S. Neusser, G. Gubbiotti, G. Carlotti, M. Krawczyk, D. Grundler, Phys. Rev. Lett. **109,** 137202(2012).

[93] S. Tacchi, M. Madami, G. Gubbiotti, G. Carlotti, S. Goolaup, A. O. Adeyeye, N. Singh, and M. P. Kostylev, Phys. Rev. B **82**, 184408 (2010).

[94] J. Topp, D. Heitmann, M. P. Kostylev, and D. Grundler, Phys. Rev. Lett. **104**, 207205 (2010).

[95] J. Topp, S. Mendach, D. Heitmann, M. Kostylev and D. Grundler, Phys. Rev. B **84**, 214413 (2011).

[96] J. Ding and A. O. Adeyeye, Adv. Funct. Mater. **23**, 1684 (2013).

[97] R. Zivieri, R.L. Stamps, Phys. Rev. B **73,** 14422 (2006).

[98] S. Tacchi, B. Botters, M. Madami, J. W. Kłos, M. L.Sokolovskyy, M. Krawczyk, G. Gubbiotti, G. Carlotti, A. O. Adeyeye, S. Neusser, and D. Grundler, Phys. Rev. B **86**, 014417 (2012).

[99] K. Yosida, *"Theory of magnetism"*, (Springer, 1996).

[100] H. Yu, G. Duerr, R. Huber, M. Bahr, T. Schwarze, F. Brandl, and D. Grundler, Nat. Commun. **4**, 2702 (2013).

[101] L. Giovannini, F. Montoncello, F. Nizzoli, G. Gubbiotti, G. Carlotti, T. Okuno, T. Shinjo, and M. Grimsditch, Phys. Rev. B **70**, 172404 (2004).

[102] M. L. Sokolovskyy and M. Krawczyk, J. Nanopart. Res. **13**, 6085 (2011).

[103] G. Gubbiotti, S. Tacchi, M. Madami, G. Carlotti, S. Jain, A .O. Adeyeye, and M.P. Kostylev, App. Phys. Lett. **100**, 162407 (2012).

[105] M. Grimsditch, L. Giovannini, F. Montoncello, F. Nizzoli, Gary K. Leaf, and Hans G. Kaper, Phys. Rev. B **70**, 054409 (2004).

[105] G. Gubbiotti, M. Madami, S. Tacchi, G. Carlotti, H. Tanigawa, T. Ono, L. Giovannini, F. Montoncello, and F. Nizzoli, Phys. Rev. Lett. **97**, 247203 (2006).

[106] J. Topp, G. Duerr, K. Thurner, and D. Grundler, Pure Appl. Chem. **83**, 1989 (2011).

[107] S. Schnittger, S. Dreyer, Ch. Jooss, S. Sievers, and U. Siegner, Appl. Phys. Lett. **90**, 042506 (2007).

[108] A. Sihvola, Metamaterials **1**, 211 (2007).

[109] R. Zivieri, "Metamaterial description of magnonic modes along ΓM direction in a 2D antidot lattice," in *Proc. Metamaterials' 2013*, pp. 181-183, Bordeaux, France, 16-21 September 2013.

[110] P. Malagò, L. Giovannini and R. Zivieri, "Effective properties of a bicomponent magnonic crystal," in *Proc. Metamaterials' 2014*, pp. 316-318, Copenhagen, Denmark, 25-30 August 2014.

[111] P. Malagò, L. Giovannini, and R. Zivieri, "Effective properties of perpendicularly magnetized 2D antidot lattices", in *Proc. Metamaterials' 2015*, pp. 535-537, Oxford, United Kingdom, 7-12 September 2015.

[112] R. Zivieri and L. Giovannini, Metamaterials **6** , 126 (2012).

[113] S. Mamica, M. Krawczyk, M.L. Sokolovskyy, J. Romero-Vivas, Phys. Rev. B **86,** 144402 (2012).